Numerical modelling of the stable atmospheric boundary layer over complex terrain and application to air quality

Julian Quimbayo-Duarte

Communauté
UNIVERSITÉ Grenoble Alpes

THÈSE

Pour obtenir le grade de

DOCTEUR DE LA COMMUNAUTE UNIVERSITE GRENOBLE ALPES

Spécialité : **Sciences de la Terre et de l'Univers et de l'Environnement (CESTUE)**

Arrêté ministériel : 25 mai 2016

Présentée par

Julian Andres Quimbayo-Duarte

Thèse dirigée par **Chantal Staquet, Université Grenoble Alpes**
codirigée par **Charles Chemel, University of Herfordshire**

préparée au sein du **Laboratoire des Ecoulements Géophysiques et Industriels (LEGI)** dans **l'École Doctorale Terre Univers Environnement**

Numerical modelling of the wintertime boundary layer over complex terrain and application to air-quality

Modélisation numérique de la couche limite hivernale sur des terrains complexes et application à la qualité de l'air

Thèse soutenue publiquement le **13/03/2019**,
devant le jury composé de :

M. Joan CUXART
Universitat de les Illes Balears, Espagne, Rapporteur
M. Dino ZARDI
Università di Trento, Italie, Rapporteur
M. Alain CLAPPIER
Université de Strasbourg, Président
M. Thierry HEDDE
Commissariat à l'Energie Atomique et aux Energies Alternatives, Examinateur
Mme. Florence TROUDE
Atmo Auvergne-Rhône-Alpes, Examinateur
M. Charles CHEMEL
University of Hertfordshire, Royaume-Uni, Co-directeur de thèse
Mme. Chantal STAQUET
Université Grenoble Alpes, Directeur de thèse

To Laura, thank you for all your love and support...

Declaration

I hereby declare that except where specific reference is made to the work of others, the contents of this dissertation are original and have not been submitted in whole or in part for consideration for any other degree or qualification in this, or any other university. This dissertation is my own work and contains nothing which is the outcome of work done in collaboration with others, except as specified in the text and Acknowledgements.

Julian Andres Quimbayo Duarte
May 2019

Acknowledgements

My first words must be for Chantal and Charles, their knowledge, patience, rigour and advice made the hard experience of a thesis still pleasant and rewarding. I would like to thank Chantal for giving me the first opportunity to work in science and help me see what I am capable of. I would like to thank Charles for teaching me the right way to deal with problems and helping me with my countless technical issues.
I would like to thank also to the members of the jury for evaluating my work and the careful reading of this document. Thank you for the interesting discussion and comments, it has greatly helped me to have some perspective on my own work.
I would like to dedicate special acknowledgement to the team of Atmo-Aura, Florence, Harry and Romain, their kind help and valuable contributions have greatly helped in the development of this thesis.
Go through this journey without friends would be impossible, so thank you very much guys for listen my complains and sorrows, and celebrate "las diminutas dichas" (the tiny joys) when we had the time, really ... thank you guys for everything! Here, I would like to say special thanks to my office mates, Keshav and Cruz, I can't imagine better companions to be trapped in that office for those four long years!
I want to say thank you to my family, my parents for bringing me where I am with their endless faith in me, my sister for her inspiration, and my brother with his continuous motivation and infinite support, thank you for so much love.
Laura, you are the beginning and end of everything, you took me when I was completely lost and taught me with your love and example what I can do. Ecko, thanks for bringing me joy and the discipline that was required at the very end of this journey.
Finally, I want to thanks Juan Andrés for taking care of me from the infinity.

Todo tiene su final, nada dura para siempre,
tenemos que recordar, que no existe eternidad ...
Willy Colón, 1973.

Abstract

During wintertime anticyclonic regimes, urbanized mountain areas often experience stable and decoupled atmospheric conditions, resulting in severe episodes of particulate air pollution. This study deals with the characterization of drivers of particulate air pollution in deep alpine valleys under such stable conditions from the point of view of atmospheric dynamics. The work has been carried out through the implementation of both idealized and real case numerical simulations using the Weather Research and Forecasting (WRF) model. Particulate air pollution has been modelled by implementing passive tracers in the simulations.

In a first part, high-resolution numerical simulations have been performed using two different configurations of three-dimensional idealized valleys opening onto a plain. The first configuration corresponds to a valley of constant width in the along-valley direction, directly opening onto a plain. The second one consists in a valley of varying width in that direction, with an upstream section of larger width than the downstream section, which opens onto the plain. The latter configuration is referred to as a pooling case. The change in the vertical temperature profile along the valley axis in all configurations results in a horizontal pressure gradient that leads to the development of an along-valley flow. Configurations in which the upstream section of the valley opens onto a narrower one have shown to be prone to higher pollutant concentrations than in the case of a valley opening directly onto a plain, due to the weaker down-valley flow developing in the variable width configurations. The impact of the downstream valley section on the concentration of pollutants in the upstream valley section is remarkable: the ventilation of the upstream valley section can be completely blocked for most of the simulation (six hours) when the ratio of the upstream to downstream valley section width is equal to 10.

The second part deals with a real case situation, focusing on a section of the alpine Arve River valley around the city of Passy. The numerical modelling of the atmospheric dynamics and particulate matter (PM) concentration in that section has been performed during a strongly polluted wintertime episode of February 2015. For this purpose the emission

inventory prepared by the air quality agency of the région Auvergne Rhône-Alpes has been implemented in the WRF-Chem model. The boundary layer dynamics has been compared to wind and temperature profiles collected during a field campaign conducted during the episode, and PM concentration has been compared to data recorded by air quality stations. The contribution of the valley tributaries to air pollution within the section considered has been first studied. Results show that this contribution is very small compared to that from local sources; this implies that $in-situ$ emissions are primarily responsible for the high PM concentration recorded in the valley since the valley bottom is decoupled from the atmosphere above the valley. The ventilation characteristics of the valley and their influence on the particulate matter (PM) concentration have next been investigated. The analysis indicates that due to the limited ventilation around the city of Passy, the hourly variability of PM concentration therein is driven by that of the emissions.

Résumé

En hiver, par condition anticyclonique hivernale, les régions montagneuses urbanisées font l'objet de conditions atmosphériques stables et découplées, qui conduisent à des épisodes de forte pollution particulaire. Ce travail de thèse traite de la caractérisation des facteurs de pollution de l'air aux particules par condition stable en vallée alpine encaissée, du point de vue de la dynamique atmosphérique. Ce travail repose sur des simulations numériques idéalisées et en conditions réelles à l'aide du modèle Weather Research and Forecasting (WRF), les particules étant modélisées par un champ de traceur passif.

Dans une première partie, des simulations numériques à haute résolution ont été réalisées, en utilisant deux configurations différentes de vallées tridimensionnelles idéalisées ouvrant sur une plaine. La première configuration correspond à une vallée de largeur constante dans la direction de l'axe de la vallée ouvrant sur une plaine. Dans la seconde configuration, la vallée est composée de deux sections, la section aval, qui ouvre sur la plaine, étant plus étroite que la section amont. Cette configuration est appelée "pooling". Quelle que soit la configuration, la variation du profil vertical de température le long de l'axe de la vallée conduit à d'un gradient de pression horizontal générant un vent de vallée. Les configurations de type "pooling" sont associées à des concentrations de polluants plus élevées que dans le cas où la largeur de la vallée ne varie pas, car le vent de vallée est plus faible dans la configuration "pooling". L'impact de la largeur de la section aval sur la concentration de polluants dans la section amont est remarquable: la ventilation de la section amont peut être complètement bloquée pendant la majeure partie de la simulation (six heures) lorsque le rapport de largeur de la section amont à la section aval est égal à 10.

La deuxième partie concerne une situation réelle en vallée alpine, durant un épisode fortement pollué de février 2015. La dynamique atmosphérique et la concentration de particules fines (PM) ont été modélisées dans une section de la vallée de l'Arve autour de la ville de Passy par le modèle WRF-Chem durant cet épisode. Pour cela, le cadastre d'émission préparé par l'agence de qualité de l'air de la région Auvergne Rhône-Alpes a été implémenté dans le modèle. La dynamique de la couche limite a été comparée à des profils verticaux de vent et température mesurés lors d'une campagne de terrain durant l'épisode pollué, et la concentration de PM comparée aux données de stations de qualité de l'air. La contribution des vallées tributaires à la pollution atmosphérique dans cette section de la vallée de l'Arve a d'abord été étudiée. Les résultats montrent que cette contribution est très faible par rapport à celle des sources locales; ceci implique que les émissions $in-situ$ sont principalement responsables de la forte concentration de particules polluantes enregistrée

dans la vallée car le fond de vallée est découplé de l'atmosphère au-dessus de la vallée. Les processus de ventilation et leur influence sur la concentration de particules (PM) ont ensuite été étudiés. L'analyse montre qu'en raison de la ventilation limitée autour de la ville de Passy, la variabilité horaire de la concentration de PM dans la ville est contrôlée par les émissions.

Table of contents

List of figures xvii

List of tables xxv

1 General Introduction 1

2 General Considerations 7

2.1 The Atmosphere 7

2.1.1 The Atmospheric Boundary Layer 8

2.1.2 The Valley Wind System 11

2.1.3 Temperature Inversions 14

2.2 Particulate air-pollution 15

2.2.1 Emissions Sources 15

2.2.2 Physical Characteristics of Aerosols 17

2.2.3 Deposition 17

2.2.4 Climate Impact 18

2.2.5 Impact on Population's Health 18

2.2.6 Regulations 19

3 Dispersion of tracers in the stable atmosphere of a valley opening on a plain 21

3.1 Introduction 22

3.2 Methods 24

3.2.1 Numerical Model 24

3.2.2 Topography of the Valley 24

3.2.3 Initial Conditions 25

3.2.4 Boundary Conditions 27

3.2.5 Numerical Parameters 28

3.2.6 Initialization of the Passive Tracer 28

3.3 Analysis of the Valley-Wind System 29

3.3.1 Overall Behaviour of the Flow 29

3.3.2 Analysis of the Flow Oscillations 31

3.3.3 Vertical Profiles of the Down-Valley Flow Speed and of the Absolute Temperature Along the Valley Axis 34

3.3.4 Regions of Turbulence 36

3.3.5 Sensitivity Study 37

3.4 Properties of the Tracer Concentration Field 40

3.4.1 Overall Behaviour of the Tracer Concentration Along the Valley Axis 40

3.4.2 Temporal Evolution of the Tracer Flux 42

3.4.3 Temporal Evolution of the Tracer Concentration 46

3.4.4 Evolution of the Tracer Concentration Along the Valley Axis 47

3.5 Summary and Conclusions 49

4 Impact of Along-Valley Orographic Variations on the Dispersion of Passive Tracers in a Stable Atmosphere 53

4.1 Introduction 54

4.2 Methods 57

4.2.1 Numerical Model 57

4.2.2 Topography 57

4.2.3 Numerical Setup 58

4.2.4 Passive Tracer Emission 59

4.3 Low Atmosphere Structure 60

4.3.1 Along-Valley Flow 60

4.3.2 Thermal Structure 61

4.4 Stagnation and Ventilation Zones 64

4.4.1 Summary of the Methodology Proposed by Allwine & Whiteman (1994) 64

4.4.2 Recirculation, Stagnation and Ventilation Zones 66

4.5 Transport of Passive Tracers 68

4.5.1 Horizontal Distribution of Tracers in the Lower Atmosphere 68

4.5.2 Ventilation Efficiency 69

4.6 Summary and Conclusions 74

5 Drivers of Severe Air Pollution Events in a Deep Valley During Wintertime 77

5.1 Introduction 78

5.2 The Numerical Model 82
5.2.1 Meteorological Model Configuration and Physics 82
5.2.2 Geographical Location and Terrain Representation 83
5.2.3 Emission Input 84
5.3 Results 87
5.3.1 Model Performance 87
5.3.2 Horizontal Distribution of the PM_{10} Concentration 96
5.3.3 Stagnation and ventilation zones in the Arve river valley 98
5.3.4 Local and Non-local Contributions 103
5.4 Conclusions and Discussion 105

6 Summary and General Conclusions **109**

6.1 Prospectives 114

References **117**

List of figures

1.1 a) The Thames below Westminster, Claude Monet (about 1871). Oil on canvas. The National Gallery, London, UK. b) Photography of a man looking at the Tower Bridge during the 1952 Great Smog (Credit: Fox Photos/Hulton Archive/Getty Images) 2

2.1 Schematic vertical temperature profile through the atmosphere highlighting the different layers that compose it. In the present work, we only focus in the troposphere layer. 8

2.2 Schematic diagram of the diurnal cycle of the atmospheric boundary layer over flat terrain under quiescent synoptic conditions (adapted from Stull, 2012). 9

2.3 Schematic diagram of the structure of the atmosphere above a complex terrain. Dark blue zones correspond to the valley atmosphere layer, and the light blue zones close to the terrain denote the slope layer (adapted from Ekhart, 1948) 10

2.4 a) Sketch of the daytime valley-wind system (up-slope and up-valley flows), b) Sketch of the nighttime valley-wind system (down-slope and down-valley flows). The red and blue curves represent the vertical profiles of the horizontal wind-valley component in a position near to the valley entrance. The red and blue curves are vertical profiles of the horizontal valley wind component at a location close to the valley inlet. Two columns of air are represented by the blue and yellow squares at the valley core and the other on the plain. The yellow and blue squares indicate layers where the potential temperature is relatively warm (W) or cold (C). The red and blue arrows represent the up-slope and down-slope flows respectively. The free atmosphere is supposed to be undisturbed under decoupled atmospheric conditions. (Adapted from Whiteman, 2000). 12

3.1 a) Three-dimensional view of topography T1. b) Terrain height in the along-valley direction at $x = 7$ km from the valley centre. c) Terrain height in the cross-valley direction for $0 \leq$ y ≤ 6 km, for T1 and T2. The numerical domain is symmetric with respect to the plane $y = 0$ and only its southern part ($y \geq 0$) is displayed in frames a) and b). 26

3.2 Locations of the passive tracer emissions. Each colour zone (Z_i) corresponds to an emission source, all zones having the same area (1440 m x 1080 m). Four different tracers were emitted in each zone at different levels (0, 95 m, 280 m and 415 m above the ground). The contours displayed are those for topography T1. 29

3.5 (t,z) diagram of the vertical velocity component [m s^{-1}] at $x = -2850$ m (mid-slope) and $y = 3000$ m. Results are shown for simulation S1. 33

3.6 Vertical profiles of the down-valley flow speed (a) and of the absolute temperature (b) averaged over the valley floor at different positions along the valley axis, at t = 360 min. Blue lines in b) correspond to the buoyancy frequency at 3 km (solid line) and 9 km (dashed line) from the beginning of the valley averaged over the last hour of simulation. The horizontal orange lines indicate the top of the different layers defined in Sect. 3.3.3. Results are shown for simulation S1. 35

3.15 View of the Grenoble valley during an anticyclonic regime on December 18, 2016. Vertically decoupled cloud layers attest of the strong stratification of the atmospheric boundary layer (photo by C. Staquet). 50

4.1 a) Contours of the terrain height in metres from the valley bottom for configuration $P2$ (the first contour is set at 50 m for configuration $P1$ is indicated with a red line). The topography is oriented north-south in the y-direction, the valley being symmetric along that axis. The system of valleys is divided in three sections, an upstream section ($\mathscr{U}$), a downstream section ($\mathscr{D}$), a junction ($\mathscr{J}$) between upstream and downstream sections, and finally a plain ($\mathscr{P}$) at the end of the valley. Six different emission zones are set along the valley axis. b) Three dimensional representation of topography $P2$. Frames (a) and (b) display the southern part of the domain. 58

4.2 Hovmöller diagram of the evolution of the along-valley wind speed at the valley centre for P1 at 10 km (a) and 16 km (b), and for P2 at 10 km (c) and 16 km (d) from the beginning of the valley. Positive (red) values correspond to a down-valley flow, negative values (blue) to an up-valley flow. 60

4.3 Cumulative mass flux across a vertical surface perpendicular to the valley axis located at 10 km from the beginning of the valley for $P1$ (blue lines) and $P2$ (red lines) at 100 (solid lines) and 200 minutes (dashed lines) of simulation. 62

4.4 Vertical cross sections of the change in the potential temperature ($\Delta\theta$) with respect to the initial condition averaged over 1 km along the y-direction after 90 minutes into the simulation for $P1$ a), and $P2$ b). Each frame is divided in two panels, the left panel corresponding to the exit of the upstream valley $\mathscr{U}$ (10 km) and the right panel corresponding to the mid part of the downstream valley $\mathscr{D}$ (16 km). White lines represent an estimate of the CAP height at each section and setup. 63

4.5 Average of the cooling rate over a cross-section extending up to the plateaux height ($\langle \partial\theta_v/\partial t \rangle_{VA}$) at the end of the first hour (blue line) and at the end of fourth hour (red line) of simulation for $P1$ (solid lines) and $P2$ (dashed lines). Vertical grey dashed lines stand for the end of each section of the valley. . . 63

4.6 Sketch of the definitions of the wind run (S_i) and of the transport distance (L). Each segment S_i is computed using an average over the time interval T equal to 15 minutes in the present work. Adapted from Allwine and Whiteman (1994). 65

4.7 Contour plots of the recirculation factor (R, top row), contour plots of the wind run (S, middle row) and zones prone to critical stagnation and ventilation (bottom row) for P_1 (a, c and e) and P_2 (b, d and f) configurations. Each point in the domain has been averaged over 15 minutes and over the first 30 m above the ground level. The unit for S is km. 67

4.8 Zoom on the upper part of the valley for $P2$ displaying streamlines. The velocity field is vertically averaged over the first 30 m above the ground and averaged in time over a) 60-120 min, b) 120-180 minutes and c) 240-300 minutes. 68

4.9 Contour plot of the tracer concentration at the end of the simulation (averaged over the last 15 minutes of simulation) for a) $TrP1_1$, b) $TrP1_3$, c) $TrP2_1$ and d) $TrP2_3$ averaged over the first 30 m along the vertical. Blue lines correspond to the locations where the critical stagnation zones are located (Figs. 4.7e and 4.7f). Green rectangles represent the emission zones for each of the tracers. Note that the label bar is different for each of the pictures. . . 71

4.10 Time series of the relative tracer mass (R_M) at the different control volumes in the system ($V_{\mathscr{U}}$, $V_{\mathscr{J}}$, $V_{\mathscr{D}}$ and $V_{\mathscr{P}}$) for tracers $TrPn_1$ (released at $\mathscr{U}$), $TrPn_3$ (released at $\mathscr{J}$), $TrPn_4$ (released at the beginning of $\mathscr{D}$) and $TrPn_5$ (released at the centre of $\mathscr{D}$). Note that $n = 1$ for $P1$ and $n = 2$ for $P2$. Solid lines represent values of $P1$ (top row), while dashed lines stand for $P2$ (bottom row). The location of the emission source of each of the tracers is presented in Fig. 4.1a. 72

4.11 Time series of the residence time ($\mathscr{T}$) of tracers $TrPn_1$ (blue lines, tracer released at $\mathscr{U}$), $TrPn_3$ (red lines, tracer released at $\mathscr{J}$) and $TrPn_5$ (green lines, tracer released at $\mathscr{D}$). Note that $n = 1$ for $P1$ and $n = 2$ for $P2$. Solid lines represent values of $P1$, while dashed lines stand for $P2$. The location of the source of each of the tracers is presented in Fig. 4.1a. Please note that for the vertical axis $\mathscr{T}$ the unit used is hours. 73

5.1 a) WRF model domain d01; domains d02, d03 and d04 noted with the boxes. b) Topographical representation of the innermost domain d05. Black contours indicate urban areas in the domain. The locations of the air quality stations in the zone are marked with coloured dots; Chamonix (blue), Passy (yellow), Sallanches (red) and Marnaz (black). The exact locations of the stations are documented in table 5.3. In addition, the location of the main measurement site in Passy-15 is denoted with the green dot. The black letters indicate the main tributaries leading to the towns of Megève (MGV), Saint-Gervais-les-Bains (StG) and Chamonix Mont-Blanc (CHX). The color areas represent a sub-array of the emissions along the valley. The color sections are named as Se_1 (red area), Se_2 (orange area), Se_3 (yellow area), Se_4 (green area), Se_5 (blue area), Se_6 (magenta area) and Se_7 (brown area). 81

5.2 First level disaggregation in time of total year emission for a complete daily cycle during the first week of February 2015 for the three main SNAP sectors emitting in the area, SNAP 2 (residential heating), SNAP 4 (industrial combustion) and SNAP 7 (route transport). Vertical dashed lines stands for the average sunrise and sunset times during the simulation period. 86

5.3 Horizontal distribution of the emission input in the domain for a complete day (9th February 2015) overlaid over contours of the terrain height (grey contours). Black contours indicate urban areas in the domain. The locations of the air quality stations in the zone are marked with coloured dots; Chamonix (blue), Passy (yellow), Sallanches (red) and Marnaz (black). In addition, the location of the main measurement site in Passy-15 is denoted with the green dot. No scale is provided for confidentiality reasons. 87

5.4 Vertical discretization of the model innermost domain (d05) in the first 1000 m above ground level. The first vertical discretization (grey line) is the one used by Arduini (2017), the second vertical discretization (black line) has been developed for this set of simulations. Each marker of the lines represents a grid point in the model. Both profiles were taken at the bottom of the valley from 556.6 m above sea level. 88

5.5 a) Simulation S_{vert2}. Temporal evolution of the vertical structure of the cold-air pool by computing the potential temperature vertical profile. Data were taken at the location of the main measurement site of the Passy-15 field campaign and are overlaid with the PM_{10} concentration registered over the same time period by the air quality station at Passy (black line). b) Temporal evolution of the vertical structure of the cold-air pool obtained by compiling potential temperature profiles from the radiosounding ascents and wind profiles retrieved from LiDAR (below 1050 m a.s.l.) and wind profiler (above 1050 m a.s.l.). Figure b) was extracted from Arduini (2017) with the author's authorization. 89

5.6 Temporal evolution of the vertical structure of the cold-air pool for simulations S_{ard} (left column), S_{vert1} (mid column) and S_{vert2} (left column) by computing the potential temperature vertical profiles (top row), wind speed (mid row) and wind direction (bottom row). All data were taken at the location of the main measurement site in Passy-15. 90

5.7 Time series of the concentration of PM_{10} in μgr m^{-3} in Chamonix (a), Passy (b), Sallanches (c) and Marnaz (d) using data collected by the AQS (dark lines), and results of WRF innermost domain d05 (light lines). The results of the model have been averaged in time over one hour, over a horizontal domain of 1/3 km centred about each AQS and vertically over 10 m from ground level. Local time is used in all time series. 93

5.8 Time series of the concentration of PM_{10} in μgr m^{-3} (color lines) and the horizontal wind speed (grey lines) using results of the simulations. The results of the model have been averaged in time over 15 minutes, over a horizontal domain of 1/3 km centred about each AQS and vertically over 10 m from ground level. Local time is used in all time series. The emission releasing profile has been added (dashed line) with no units as a reference. The calculations have been done for the positions of the AQS at Passy (a) and Sallanches (b). 94

5.9 Temporal evolution of the vertical structure of the cold-air pool in the innermost domain (d05) using data of potential temperature at Passy (a) and Sallanches (b). 95

5.10 Contour plots of six-hour average of PM_{10} concentration [μgr m^{-3}] averaged along the vertical in the first 10 m above the ground overlayed with contour lines of the terrain height. Black contours indicate urban areas in the domain. The locations of the air quality stations in the zone are marked with coloured dots; Chamonix (blue), Passy (yellow), Sallanches (red) and Marnaz (black). The exact locations of the stations are documented in table 5.3. In addition, the location of the main measurement site in Passy-15 is denoted with the green dot. 97

5.11 a) Hourly area average of the emissions released in each of the valley sections previously defined in Fig. 5.1a normalized with the area averaged emission for the whole domain. b) Time series of the ratio R_{cc} between the volume averaged concentration and the area-averaged emissions of PM_{10} for each of the valley sections (valley sections defined in Fig. 5.1a). 99

5.12 Timeseries of the wind run S (a) and the recirculation index R (b) for the winter 2014-2015 (1st December 2015 to the 28th February 2015). Data retrieved from LiDAR measurements at the position of the IOP at 40 m a.g.l. The calculation has been done using a τ= 6 hr. 100

5.13 Maps tracking the zones prone to critical stagnation (CS), stagnation (S), recirculation (R), low ventilation (LV) and ventilation (V) using a six-hour average in time and averaged along the vertical in the first 10 m above the ground. The results have been overlayed with contour lines of the terrain height. The data is masked to show the information only for terrain height lower than 1500 m a.s.l. Black contours indicate urban areas in the domain. The locations of the air quality stations in the zone are marked with coloured dots; Chamonix (blue), Passy (yellow), Sallanches (red) and Marnaz (black). The exact locations of the stations are documented in table 5.3. In addition, the location of the main measurement site in Passy-15 is denoted with the green dot. 102

5.14 Timeseries of the relative contribution in percentage of each of the valley sections (see Fig. 5.1b) to the value recorded in the AQS position in Chamonix (a), Passy (b), Sallanches (c) and Marnaz (d) using the data produced in the innermost domain d05. The results of the model have been averaged in time every 15 minutesand in space over a horizontal square of side 1/3 km around the location of AQS station; an average is also performed over the first 10 m above ground level. 104

List of tables

3.1 Main parameters of the simulations. The number of grid points indicated is that of the inner domain, the horizontal resolution being 90 m. In the outer domain, the horizontal resolution is set to 270 m. 27

3.2 Location of the tracers released in the simulations. Each tracer is named $TrSn_{i,j}$, where $1 \leq n \leq 3$ is the simulation number, $1 \leq i \leq 4$ is the zone number on the valley bottom and $1 \leq j \leq 4$ is the height index at which the tracer is released over the valley bottom. All zones are horizontal and centred with respect to the valley axis. For $i = 1$, Z_i is also centred with respect to the position $y = 3$ km; for $i = 2$, $y = 5$ km; for $i = 3$, $y = 7$ km and for $i = 4$, $y = 9$ km. For $j = 1$, the tracer is released at the valley bottom; for $j = 2$, at 95 m above the valley bottom; for $j = 3$, at 280 m and for $j = 4$, at 415 m. The zones correspond to the colour areas Z_i in Fig. 3.2; each zone has an area of 1440×1080 km^2. 30

5.1 Main parameters used in the simulations. The number of grid points nx, ny, nz correspond to the east-west, north-south and vertical directions, respectively. The vertical coordinate is stretched with height, Δz_{min} represents the height above the ground of the first grid point, the first mass point being located at $\Delta z_{min}/2$ m. 82

5.2 The contribution of each SNAP sector in mass (percentage) to the total PM_{10} emission in the numerical domain; according to the emission inventory provided by Atmo-Aura for the year 2015. 85

5.3 Localisation of the four air-quality stations in the domain. Colour dots in figure 5.3 represent the locations of the four air-quality stations and the position of the IOP measurement site in the map. 86

5.4 Definition of the five categories to characterize the transport properties of the flow proposed by Largeron (2010). The critical values for the wind run have been modified to better describe the wind structure in the Arve River Valley (IOP location). The values registered herein for the critical values have been selected using a $\tau = 6$ hr. 101

Chapter 1

General Introduction

Air pollution is not a new problem of the modern society, in fact, it began at least eight hundred years ago. In medieval England, air pollution was first documented when King Edward I created the world's first anti-smoke commission and banned the burning of sea coal in the city of London (Christy, 1960). A few years later, in 1303, the importance of the stack's height was recognized in the dispersion of pollutants for the first time and London started to regulate the minimum stack heights (Chew and Kellaway, 1973). In the second half of the 17th century, John Evelyn, one of the best diarists of his time and founder member of the Royal Society of London, published one of the first written books on the growing problem of air pollution in London: *Fumifugium, or, The inconveniencie of the aer and smoak of London dissipated together with some remedies* (Evelyn, 1661). In this work, Evelyn denounced the general air-pollution in London and the possible effects in human health. In this document Evelyn also advised some ways to ameliorate the situation to King Charles II and the parliament, i.a., he thought that wood burning may be better for the local air-quality than coal burning.

The beginning of the Industrial Revolution marked a clear increase in particle emissions near the industrial districts of the northern hemisphere, England being its cradle, air pollution problems in London were massive during the eighteenth and nineteenth centuries. Some of the early visual records of this type of pollution are the works of French painter Claude Monet, who moved to London during the Franco-Prussian war (1870-1871). In his work "The Thames below Westminster" (see Fig. 1.1a), the painter showed the misty and polluted atmosphere of the capital on a spring day, with the Houses of Parliament and the Westminster Bridge in the background. The combination between the traditional London's fog and the

(a) (b)

Fig. 1.1 *a) The Thames below Westminster, Claude Monet (about 1871). Oil on canvas. The National Gallery, London, UK. b) Photography of a man looking at the Tower Bridge during the 1952 Great Smog (Credit: Fox Photos/Hulton Archive/Getty Images)*

smoke coming from the chimneys around the city generated a brown layer of air that was later called smog (smoke+fog). The word was firstly used by Dr. Henry Antoine Des Voeux in a paper presented in the Public Health Congress in London (1905).

Atmospheric pollution problems peaked in December 1952, when an anticyclonic regime established over the city of London creating a strong temperature inversion that generated a very calm atmosphere. This inversion trapped the smoke of 3.5 million chimneys and many industrial stacks. The event was known as the great London smog of 1952, the visibility was reduced to a few metres during the day making very difficult even to walk through the city (see Fig. 1.1b). During the event, the death of more than four thousand people was recorded (Bell et al., 2004). This event is remembered as the most important pollution episode in history, due to the impact it had on public perception of air pollution and on government regulation. The negative effects on population's health during the episode and months later highlighted the link between human health and poor air quality, which led the British government to create the Clean Air Act in 1956. The main aim of the Act was to control emissions in the country for the first time and to encourage the introduction of new technologies to reduce noxious emissions from coal combustion devices.

Although London's industrial development is closely related to the development of air pollution problems, the city is not the only place where a well-documented pollution record has been made and coal burning is not the only cause of poor air quality. On the west coast of the US, the city of Los Angeles (LA) has suffered from major pollution events in recent decades and has become a benchmark for poor air quality in North America with a significant rate of related mortality (Kinney and Özkaynak, 1991). The city is located in a coastal

plain surrounded by high mountains, leaving it at the mercy of temperature inversions that completely trap pollutants therein. On July 26, 1943, the city suffered for the first time from an air pollution episode, via the formation of a dense layer of smog. California government set in 1947 an emission control organization, the LA air pollution control district, whose aim was to regulate the industry emission. These episodes of extreme pollution have opened the door to the development of emission control worldwide. Around the same time in France for example (1954, having already air pollution problems in the capital and in some of the main cities), an agency to study the effects of air pollution on society was set up for the first time, "La commission interministérielle pour l'étude de la pollution atmosphérique", but it was not until 1974 that a control of polluting emissions into the atmosphere was introduced.

Emissions are undoubtedly a critical factor in air pollution, however, as was recorded during the big smog event in London, meteorological aspects also plays an important role in the problem (Megaritis et al., 2014). In complex terrain, the problem has an additional complexity because the flow of air over the orography generates a wide range of responses that cover all scales of the atmosphere. Mountains impact airflow by modifying advection processes at synoptic scale and generating planetary waves, producing organized movements at mesoscale and altering turbulent mixture at microscale (Serafin et al., 2018), which cause massive changes in the processes of transport and dispersion of pollutants in the atmosphere.

In Europe, the Alps are a major reference of complex terrain, having a large influence on the climate of the continent. Italy, France, Germany, Switzerland and Austria share their borders through the Alps, having 14 million inhabitants living mainly at the mountain's sides favoured by major rivers and rich farmland. Until the first half of the 20th century, much of the pollution in the Alps was attributed to the industrial sector, but with the start of emission control, the high cost of transport and the growing scale of commercial operations, the main emitters (such as the manufacture of iron and aluminium) began to leave the valleys, although it is still a large emitter in the Alpine region. In the last decades road transport has become one of the most important emitters in the area with the construction of route tunnels through the Alps that increased the traffic in the area (Aymoz et al., 2007). The Chamonix Valley has been receiving cross-border traffic since "Le tunnel du Mont-Blanc" opened in 1965. The construction of "l'autoroute blanche" in 1973 through the Arve River Valley and the opening of the Fréjus tunnel in 1980 in the Maurienne Valley transformed these valleys into some of the main roads for freight transportation in Europe.

During winter there is usually an increase in particulate air pollution in mountain areas (Zoras et al., 2006, Whiteman et al., 2014, Largeron and Staquet, 2016), when the

atmosphere is subject to strongly stable conditions that prevent mixing and increase air stagnation between mountains. The contribution of biomass burning for residential heating becomes an important factor in air quality problems in the area (Szidat et al., 2007).

Even with the high technological development of recent years that has helped to develop more efficient systems for better use of resources, air quality remains a constant concern throughout the world. However, our society still requires combustion to meet our energy demand (production of energy through thermal power plants) and combustion is also essential in large part of current industrial processes.

Scope of the Present Work

Although pollution is generally attributed to chemicals composites such as carbon dioxide (CO_2), sulphur oxides (SO_x), nitrogen oxides (NO_x), carbon monoxide (CO) or volatile organic compounds (VOCs), particulate air pollution (fine particles of solids or liquids suspended in a gas) requires special attention because of the proven correlation with increased incidence of respiratory symptoms, decreased lung function, increased hospitalization for respiratory diseases and increased mortality (Pope and Dockery, 2006). In France in 2012, 43.400 premature deaths were attributed to Particulate Matter (PM) air pollution (E.E.A, 2015), which is the pollutant with the largest impact on population's health.

Air-pollution is a difficult problem due to the multiple variables involved, from chemical interactions in the atmosphere to the atmospheric dynamics over complex terrain. Numerical weather prediction models have been used extensively to describe the atmosphere in order to feed (or be coupled with) chemical models to track and predict pollution in the atmosphere (Grell et al., 2000, Silcox et al., 2012, Neemann et al., 2015). The problem is that the current capacity of computers does not allow such numerical models to be run with a resolution that adequately solves the small-scale temporal and spatial atmospheric processes that affect the life of pollutants in an operational time-scale, which highlights the need for better sub-grid scale parametrizations of these processes. One of the problems related to such parametrizations is that most of the current three-dimensional numerical models calculate surface fluxes through the implementation of one-dimensional schemes based on the Monin-Obukhov similarity theory (MOST). MOST has been found to work well only on flat and uniform terrain; however, in mountain areas, the influence of slope flows plays an important role in the flow dynamics resulting in an additional source of errors. MOST was mainly

designed to solve externally driven flows, implying that density-driven flows developing over slopes cannot be well resolved (Łobocki, 2014).

Outline and Research Objectives

The focus of this work is the study of PM transport processes (modelled as a passive scalar to avoid the chemical complexity involved in the problem) over complex terrain in a stable boundary layer decoupled from above. The present document starts with a brief scientific background in Chapter 2. The scientific work is organized into three chapters and address the following objectives:

I To characterise the effect of the thermally-driven valley-wind system on the pollutant transport in a nocturnal stable layer of a rectilinear valley opening on a plain;

II To quantify the influence of along-valley orographic variations on the creation of pollutant stagnation and ventilation zones in a valley under stable atmospheric conditions;

III To characterize the role of the valley-wind system on the horizontal distribution of particulate matter in real conditions in a stable valley atmosphere;

IV To identify and quantify the effect of local pollutant sources in the resultant daily cycle of PM concentration in a stable valley atmosphere.

The work is thought to gradually increase the complexity of the problem throughout the document starting with the study of the pollution transport processes in an idealized simple valley opening on a plane in Chapter 3, addressing objective I. Then, a more complex set-up taking into account the orographic variations along the valley axis is studied in Chapter 4 to explore the objective II. The objectives III and IV are explored in Chapter 5 using the results from a realistic simulation of one episode of a field-campaign conducted in the alpine Arve River valley under stable conditions. Finally, general conclusions and future prospectives are presented in Chapter 6.

Chapter 2

General Considerations

In urban areas, air pollution mainly results from human activities. Most of the emissions of polluting compounds into the atmosphere occurs near the surface, in the first few dozen meters, which justifies the fact that this work focuses on transport and mixing processes in the lower atmosphere (specified below). This chapter is divided into two main sections. The first part presents the main concepts related to meteorology, with special attention to air circulation in mountain valleys (Sect. 2.1). The second part highlights the importance of particulate air pollution problems for the population's health and the overall effects on climate, together with an overview of the main physical characteristics of aerosols (Sect. 2.2).

2.1 The Atmosphere

The Earth's atmosphere is divided into two layers, the lower atmosphere composed of the troposphere and the tropopause, extending from the surface up to an altitude of about 10 km. The upper atmosphere then consists of all the layers above the tropopause (stratosphere, stratopause, mesosphere, mesopause and thermosphere) up to 140 km above the earth's surface, which roughly corresponds to 2% of the total earth radius (see Fig. 2.1). The atmosphere is composed by gases, such as nitrogen (78%), oxygen(21%), argon (0.9%) and some trace gases (such as ozone, 0.01%) and 99% of this mass is concentrated in the first 30 km above the surface (Jacobson, 2005).

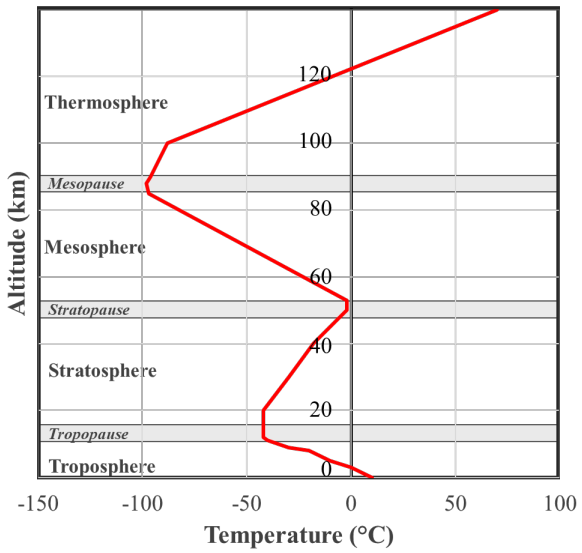

Fig. 2.1 *Schematic vertical temperature profile through the atmosphere highlighting the different layers that compose it. In the present work, we only focus in the troposphere layer.*

In the following the processes driving air circulation in the lower troposphere are discussed, focusing on the atmospheric boundary layer over complex terrain.

2.1.1 The Atmospheric Boundary Layer

Human activities develop almost entirely in the first few hundreds meters above the Earth's surface. This first layer of air is commonly called the atmospheric boundary layer (ABL). Stull (2012) has defined it as follows: *"We can define the boundary layer as that part of the troposphere that is directly influenced by the presence of the earth's surface, and responds to surface forcings with a time scale of about an hour or less".* Its characteristics are also variable depending on the underlying surface, the thickness of the ABL reaching values ranging from a few tens of metres in Antarctica to a few kilometres at mid- and low-latitudes. Above the ABL the rest of the troposphere is known as the free atmosphere. The free atmosphere which is not influenced by surface forcing, so it experiences temporal variations greater than a few hours (no daily variations are detected).

The heating and cooling of the soil due to radiative forcing from the atmosphere (long and short wave radiations) results in a heat exchange between the soil and the boundary layer, which generates transport processes associated with turbulence. The general behaviour of the ABL over flat terrain and its evolution during the day have been well described in

Stull (2012) and a brief summary is now provided on the basis of Fig. 2.2. Four main layers are distinguished in the atmosphere throughout the day, a surface layer, a convective mixed layer, a stable layer and a residual layer. The surface layer is located near the ground, and is defined by the height over which the momentum and heat fluxes vary by less than 10%. The surface layer is present throughout the day no matter how is the behaviour of the rest of the atmosphere.

In the first hours of the morning, after sunrise, a convective layer is created and in the afternoon dominates the ABL due to the heat exchange with the ground. In the late afternoon, at sunset, the shortwave radiation from the sun ceases and the heat exchange between the ground and the atmosphere reverses slowly decreasing the turbulent character of the atmosphere; as a result, the lower part of the atmosphere affected by the longwave radiative cooling from the ground is slowly transformed into a stable layer, displaying a weak and sporadic turbulence. The well mixed part of the atmosphere located just above the stable layer, which is not affected by the nocturnal ground cooling, is called the residual layer.

Due to the weak turbulence in the stable layer, vertical transport in this layer is very weak as well and transport is predominantly horizontal. The stable atmosphere promotes the propagation of internal gravity waves and the trapping of many high frequency wave fields between the ground and its highest part (Whiteman et al., 2008).

In the next morning, the radiative energy from the sun starts heating the ground, leading to a convective layer from the ground that slowly breaks the stability of the layer.

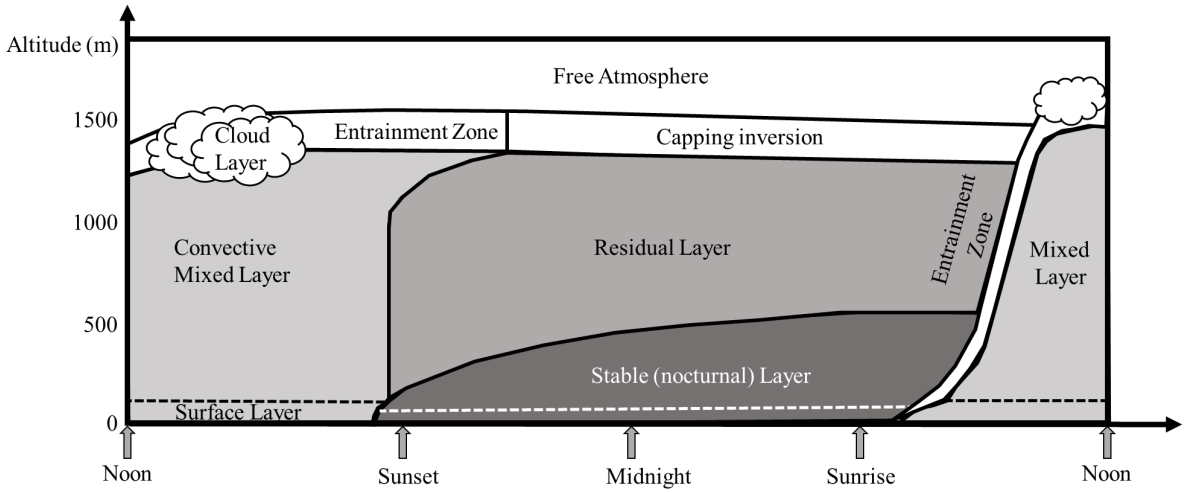

Fig. 2.2 *Schematic diagram of the diurnal cycle of the atmospheric boundary layer over flat terrain under quiescent synoptic conditions (adapted from Stull, 2012).*

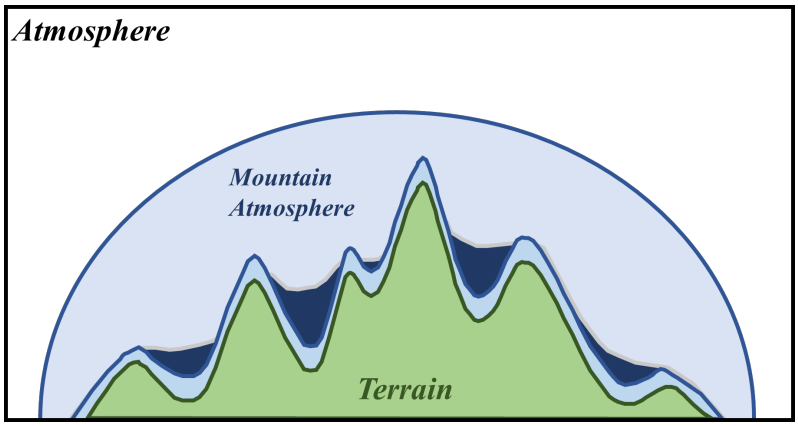

Fig. 2.3 *Schematic diagram of the structure of the atmosphere above a complex terrain. Dark blue zones correspond to the valley atmosphere layer, and the light blue zones close to the terrain denote the slope layer (adapted from Ekhart, 1948)*

Although much of the research on this topic has been addressed on a flat and homogeneous terrain (see for instance Garratt et al., 1992), in the following the general characteristics of the ABL are explored with a special attention to the processes over complex terrain.

The Atmospheric Boundary Layer over Complex Terrain

The interaction between the earth's surface and the boundary layer, together with the resulting transport processes, have already been highlighted as key aspects of the dynamics of the ABL. In complex terrain, additional factors such as terrain-induced flows or shadow effects, among others, must be considered. The flows observed over mountainous terrain can be related mainly to two types of flows: (i) Terrain-induced flows, when topography affects large-scale flows by changing their speed or direction (e.g. flow channelling between mountains). (ii) Mountain flows, which are associated with thermally driven flows. Temperature difference between sections of a valley, or between a valley section and an adjacent plain generate pressure gradients driving intra-mountain transport. This work focuses on the second type of flow.

Over mountainous terrain three layers can be distinguished in response to the radiative flux variation of the ground during the day (see Fig. 2.3). A first shallow layer (a few metres deep), called the "slope layer", is found just above the surface and responds directly to the influence of the ground. The layer is associated with thermally driven slope flows that develop and circulate therein. A second and deeper layer called the "valley atmosphere" layer (a few hundred metres deep) covers and occupies the concavities between the mountains.

During the night it corresponds to the stable layer mentioned above for flat terrain. The layer is characterized by containing the thermally driven along-valley flows, which are associated with scales of the order of 1 to 100 km. Finally, the "mountain atmosphere" (third layer), which contains the two previous layers, experiences the dynamic influence of the mountain range as a whole, meaning that it can be affected by the processes that occur in the surrounding valleys (Ekhart, 1948).

2.1.2 The Valley Wind System

Several studies have addressed the physical mechanisms responsible for the creation and maintenance of the valley wind system. The basis of the theory was developed in the first half of the twentieth century (Wagner, 1938, Ekhart, 1948, Defant, 1949) and nowadays, the basic mechanisms driving the valley flows are well understood. The interaction between the valley wind flows in the valley boundary layer is a continuous and complex process that can be affected even by large-scale flows at the top of the mountainous atmosphere (Zardi and Whiteman, 2013). Although an isolated valley-wind component is difficult to observe, the contribution of the slope flows in the triggering of valley wind dynamics is crucial.

Slope flows

Slope flows can be detected both up-slope and down-slope on a valley sidewall or on an isolated hill or mountain, usually with up-slope flows during the day and down-slope flows at night (see Fig. 2.4). This wind system is created as a response to the heat exchange between the ground and the atmosphere. During the day, due to the short-wave radiation emitted by the sun, the ground warms up and the air near it heats up. The warmer air begins to be transported in the up-slope direction due to buoyancy effects. During the night, the process is reversed due to the absence of solar radiation; the ground and the air near it are cooled generating a cooler and denser air flowing down the slope and associated with a downward heat flux. This wind system is stronger and easier to detect in synoptic anticyclonic weather conditions, with clear skies that allow maximum cooling of the air close to the ground.

Several works have addressed the problem from the observations side (Kuwagata and Kondo, 1989, De Wekker, 2008, Jiménez and Cuxart, 2014), due to the difficulties implicit in the measurement of such flows (mast towers are not easy to configure and not always can cover the whole flow layer for example), theoretical models (Prandtl, 1952, McNider, 1982)

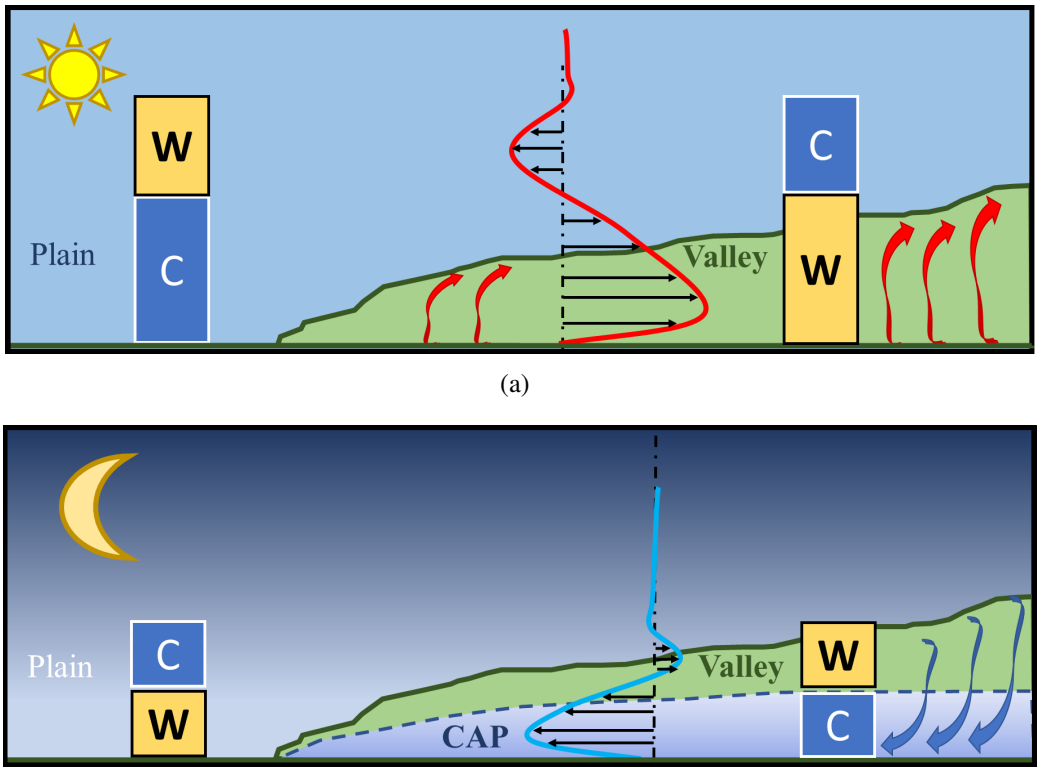

Fig. 2.4 *a) Sketch of the daytime valley-wind system (up-slope and up-valley flows), b) Sketch of the nighttime valley-wind system (down-slope and down-valley flows). The red and blue curves represent the vertical profiles of the horizontal wind-valley component in a position near to the valley entrance. The red and blue curves are vertical profiles of the horizontal valley wind component at a location close to the valley inlet. Two columns of air are represented by the blue and yellow squares at the valley core and the other on the plain. The yellow and blue squares indicate layers where the potential temperature is relatively warm (W) or cold (C). The red and blue arrows represent the up-slope and down-slope flows respectively. The free atmosphere is supposed to be undisturbed under decoupled atmospheric conditions. (Adapted from Whiteman, 2000).*

and numerical modelling (Schuman, 1990, Atkinson and Shahub, 1994, Cuxart et al., 2007) have been developed to complement the observations in order to properly understand and subsequently predict the development and maintenance of slope flows.

McNider (1982) for example, from observations of oscillations in the speed magnitude of nocturnal down-slope flows (Heywood, 1933, Doran and Horst, 1981) and based on the work of Fleagle (1950), developed a model to determine the characteristic of a down-slope wind flowing over a constant slope of infinite extent in a uniformly stratified atmosphere. The model predicts that a fluid particle advected by the down-slope wind oscillates as a result of buoyancy and adiabatic cooling effects at a frequency depending on the environmental

lapse rate and the slope angle. The frequency of oscillation is indeed given by $N \sin \alpha / 2\pi$, where α is the slope angle and N, the Brunt-Väisäla frequency, which is defined as:

$$N = \sqrt{\frac{g}{\theta} \frac{d\theta}{dz}} \tag{2.1}$$

where g is the gravitational acceleration and θ the potential temperature. When the down-slope flow reaches the valley bottom, it looses energy via a hydraulic jump process and radiates internal gravity waves. The latter has been shown by Chemel et al. (2009a) using numerical simulations.

Valley Flows

At night, the down-slope flows carry cold air to the valley bottom generating an accumulation therein. Together with radiative cooling of the valley bottom, a layer of cold air called "cold air pool" (CAP) forms over the valley floor, being associated with a temperature inversion (discussed below). The growth of the CAP leads to a colder atmosphere inside the valley (valley atmosphere) than in the neighbouring regions creating a horizontal pressure gradient that drives the development of a down-valley wind flowing inside the valley layer (see Fig. 2.4b). Note that in this case the flow is fully driven by the pressure gradient, meaning that it can develop even on a flat valley floor.

In the following morning, the radiation from the sun warms up the ground and the atmosphere, creating a turbulence transport of momentum that breaks up the stable valley atmosphere. As it was mentioned above the slope flows start to transport air in the up-slope direction and the valley atmosphere becomes warmer than the air on the plain (see Fig. 2.4b). The temperature difference between the valley atmosphere and the plain creates a horizontal pressure gradient driving the characteristic diurnal up-valley flow. The development of those thermally forced flows in valleys has been studied by Wagner (1938) and further investigated later by several authors (Steinacker, 1984, Vergeiner and Dreiseitl, 1987, McKee and O'Neal, 1989) using the concept of "topographic amplification factor" (TAF). The TAF is a pure geometric concept based on the fact that in a valley a certain energy input is distributed in a smaller volume of air than if the same energy input was applied over a plane, which results in greater warming in the case of the valley atmosphere. This is also the case at night, when the energy is subtracted from the system, the smaller volume in a valley will be easier to cool.

Both up- and down-valley winds have been commonly observed in field campaigns. In the Inn Valley located in the Austrian Alps for example, Vergeiner and Dreiseitl (1987) have reported differences close to 5 hPa over a distance of 100 km driving along-valley winds with speeds in the range from 3 to 10 m s^{-1}. From observations of nocturnal down-valley flows in the Kimball Creek Valley located in Colorado, Porch et al. (1991) reported oscillations in the speed magnitude with a 20 minutes period. The authors attributed these oscillations to interaction between the main valley flow and the flows coming from the tributaries.

Due to the complexity of the valley-wind system, idealized simulations have been used as a tool to isolate the main variables of the problem and better understand the mechanisms that drive the creation of slope flows and along-valley flows. Several studies using both 2D (or infinite valley length) (Bader and McKee, 1985, Anquetin et al., 1998, Catalano and Cenedese, 2010, Burns and Chemel, 2014, 2015) and 3D (Rampanelli et al., 2004, Schmidli and Rotunno, 2010, Lehner and Gohm, 2010a, Largeron et al., 2013b, Arduini, 2017) idealized valley topographies in both convective and stable conditions have been performed to identify the different variables affecting the development of the valley wind system (such as the slope angle, slope length, the surface characteristics, i.a.) and the influence of the valley-wind system on the valley atmosphere (CAP formation, wave generation, i.a.).

2.1.3 Temperature Inversions

During the night, the ground at the valley bottom cools the adjacent air and the cold air layers coming from the slopes meet at the valley centre. The cold air starts to accumulate at the valley centre and generates a CAP in the valley core (see 2.4b). As the night evolves, the CAP is fed by the down-slope winds and becomes deeper and deeper. This phenomenon generates a temperature inversion at the valley core. During the following morning, the temperature inversion is destroyed by diurnal convective processes triggered by incoming radiation from the sun (this processes is well explained in Whiteman, 1982, Anquetin et al., 1998).

The temperature inversion is not always destroyed in the next morning, especially in wintertime. CAPs, for example, can last for several days when large-scale flows, as an anticyclonic regime, limit the exchanges of heat and mass between the valley core and the free atmosphere preventing the turbulent erosion of the stable layer in the valley. The mesoscale flows and radiative, turbulent and cloud processes may also affect its evolution. During one of the nights in the Persistent Cold Air Pool Study (Lareau et al., 2013), the

combination of radiative cooling at the top of the cloud layer and synoptic scale heating of the air produced a potential temperature deficit of about -25 K, promoting a stable atmosphere (that was related to a high particulate pollution level). Indeed, due to the stability of the atmosphere associated with temperature inversions, turbulent mixing is suppressed which is a situation prone to pollutant accumulation.

2.2 Particulate air-pollution

In general terms, particulate matter may be defined as: *"any substance, except pure water, that exits as a liquid or solid in the atmosphere under normal conditions and is of microscopic or submicroscopic size but larger than molecular dimensions"* (Seinfeld and Pandis, 2012). Particulate matter can be produced by direct emissions of particles, or by the condensation into particles and liquid droplets of some gases. Those particles and liquid droplets may be composed of acids, organic chemicals, metals, and soil or dust particles. The variability of particulate matter in the atmosphere is quite wide, meaning that an appropriate description of atmospheric particles requires more information than their concentration; their size, chemical composition, phase and morphology are also required. The present work deals with the transport of aerosols (a colloidal suspension of particles dispersed in air or gas) with special attention to particles with an aerodynamic diameter[1] less than 10 μm (PM_{10}) emitted by anthropogenic sources.

2.2.1 Emissions Sources

Emission sources are generally classified into two main categories: natural emissions and anthropogenic emissions. As noted above, the present work focuses on emissions linked to human activities such as combustion and industrial processes. The combustion of fossil fuels is one of the main sources of pollution due to its use in the road transport sector. This sector is known to be an important actor in pollution problems. The combustion processes of fossil fuels result in particles mainly composed of carbon, but other compounds such as sulphur, water-soluble ions and metallic waste are also found to be a product of combustion (Schauer and Cass, 2000, Schauer et al., 1999). Other human activities such as the burning of natural gas for domestic use (heating and cooking) should also be taken into account, although their

[1] The aerodynamic diameter of an irregular particle is defined as the diameter of the spherical particle with a density of 1000 kg m^{-3} and the same settling velocity as the irregular particle (Hinds, 2012, P53).

contribution is not comparable with emissions from road transport. The residential heating, through the combustion of biomass, is an important source of coarse particulate matter emissions. Indeed in some regions in the northern French Alps it is the main contributor to PM_{10} during the cold seasons (Jaffrezo et al., 2005, Atmo-Auvergne-Rhone-Alpes, 2018).

Due to the wide range of industrial sources, emissions from the industrial sector is divided into sub-sectors such as the oil related activities, metallurgy industry, chemical industry, thermal power plants for energy production, i.a. The composition of emissions varies greatly from one industrial process to the other, and it is very difficult to attribute a source to particles found in the atmosphere in a given place[2]. Nonetheless, some sub-sectors are well know for their common emissions, such as the petrochemical industry that is characterized by the presence of nickel and vanadium (Querol et al., 2002), or the metallurgical industry which is highlighted by the presence of lead, silver, caesium and rubidium (Alleman et al., 2010).

The aerosols may be categorized according to their formation processes: primary (directly emitted into the atmosphere) and secondary (transformation and condensation process of chemical compounds in the atmosphere) aerosols. Secondary aerosols may be composed of inorganic or organic compounds. Secondary organic aerosols (SOA) are produced through the complex interaction of sunlight, volatile organic compounds (VOCs) from trees, plants, automobiles or industrial emissions, and other airborne chemical compounds. Although it has been proven that much of the SOAs in the atmosphere are produced by VOCs emitted by vegetation, their presence in the atmosphere is highlighted by human activities (Kanakidou et al., 2000).

Sulphates and nitrates form secondary inorganic aerosols (SIA). The precursors for those aerosols are sulphur dioxide (SO_2), nitrogen oxides (NO_x including NO and NO_2) and ammonia (NH_3). SO_2 is emitted by the combustion of fossil fuels (coal, fuel oil). The oxidation of the dimethyl sulphide, produced by marine algae, can also lead to formation of sulphates (Seinfeld and Pandis, 2012).

Aerosols can be emitted to the atmosphere by a wide range of either natural or anthropogenic sources. Due to the variety of those sources, they can be composed of a great range

[2]In the Northern French Alps, the DECOMBIO project (Chevrier et al., 2016) has investigated the physical and chemical properties of PM_{10} found around the town of Passy. The origin of these particles has been traced through the determination of the biomass fraction in the particulate matter found in the area. Biomass combustion is related to the combustion of wood for residential heating.

of chemical compounds such as sulphates (SO_4^{-2}), nitrates (NO_3^-), ammonia (NH_3), organic carbon (OC), black carbon (BC), i.a.

2.2.2 Physical Characteristics of Aerosols

Particles with an aerodynamic diameter less than 2.5 μm ($PM_{2.5}$) are considered as *fine particles* while particles with an aerodynamic diameter between 2.5 and 10 μm (PM_{10}) are considered as coarse particles. Particles are distributed in four main modes as follows (Seinfeld and Pandis, 2012): i) nucleation mode: representing aerosols with a diameter less than 0.02 μm, formed by steam condensation during combustion processes or by nucleation of gas molecules; ii) Aitken mode: aerosols with a diameter between 0.02 and 0.1 μm, often regrouped with the nucleation mode, mainly formed by the coagulation of ultrafine particles; iii) Accumulation mode: aerosols with a diameter between 0.1 μm and 2.5 μm including combustion particles and particles resulting from the condensation of vapour on the particles and coagulation of particles from the nucleation mode; iv) Coarse mode: aerosols with a diameter greater than 2.5μm formed by anthropogenic mechanical processes, such as agriculture, industry, mining, and natural processes, which result from the raising of desert dust or sea spray. The life time of aerosols strongly depends on the chemical compounds, and on the part of the atmosphere where it spends its "life": from a few minutes for NO_3 released near the surface, up to years for CH_4 subjected to synoptic forcing in the upper troposphere (Seinfeld and Pandis, 2012).

2.2.3 Deposition

Aerosols may be removed from the atmosphere by means of two processes: dry deposition (dry weather) and wet deposition (in the presence of precipitations). Dry deposition basically is a consequence of the atmospheric exchange mechanisms (heat and mass), but it is also greatly influenced by a number of surface properties (physical, chemical and biological), and by the physical properties of particles (Hicks et al., 1987). Wet deposition is observed during precipitation when the aerosols are transported to the surface with the droplets, either by coagulation or nucleation of particles within a cloud (rainout), or by capture by raindrops under the cloud (washout) (Sehmel, 1980).

2.2.4 Climate Impact

Aerosols are known for absorbing solar radiation causing changes in vertical profiles of temperature and relative humidity. Therefore, they may have a significant impact on the formation and shape of clouds (Ackerman et al., 2000). Black carbon (BC) in soot, for example, is an important product of combustion and is well known as the dominant absorber of visible solar radiation, converting it into heat and releasing it into the atmosphere. Indeed, BC emissions are considered the second largest contributor to global warming after CO_2 emissions (Bond et al., 2013). BC can often be transported over long distances, mixing with other available aerosols in the atmosphere along the way. This mixture of aerosols can even form a transcontinental plume of atmospheric brown clouds, with vertical extensions of 3 to 5 km (Jacobson, 2002).

In the south of China and India, a moderate cooling has been recorded in the last years while most of the world has been warming. Reflective, like sulphates, and absorbing, like BC, aerosols may be responsible for such cooling of the atmosphere preventing solar radiation to reach the ground then generating a localized cooling. Indeed, those changes in the temperature are usually reported in summer when the effects of aerosols are larger (Menon et al., 2002).

The aerosols may affect several important aspects in the planet's ecosystem, such as Earth's energy balance, hydrological cycle, atmospheric circulation and the abundance of greenhouse gases and trace reactive gases in the atmosphere. Furthermore, they also play an important role in the reproduction of biological organisms which may cause or exacerbate diseases (Pöschl, 2005).

2.2.5 Impact on Population's Health

According to the World Health Organization, 4.2 million premature deaths worldwide for 2016 can be attributed to (outdoor) air pollution in both cities and rural areas. In fact, particulate air pollution accounts for a significant proportion of that figure, contributing to an estimated 800,000 premature deaths each year, making it the 13th leading cause of death worldwide (Anderson et al., 2012a). It has been demonstrated that particulate air pollution has a strong relationship with cardiovascular (Samet et al., 2000) and cerebrovascular (Dominici et al., 2006) diseases through the mechanisms of systemic inflammation, direct and indirect activation of coagulation and direct transport of polluting particles from the lungs to the

systemic circulation. Respiratory diseases are also accentuated by exposure to PM. The creation of oxidative stress and inflammation by the exposure to PM leads to anatomical and physiological alteration of the lungs (Avol et al., 2001).

2.2.6 Regulations

As it was introduced in Chapter 1, due to the proven negative relation between the particulate air-pollution and population's health, several governments have developed their own regulations to control the emission of potentially harmful particles in the atmosphere. The Clean-Air Act (1956) introduced in England several measures to reduce air pollution, notably through the introduction of "smoke control zones" in some towns and cities where only smokeless fuels[3] could be burned. In north America, the US signed their first Clean Air Act in 1970. Through this law, the Environmental Protection Agency (EPA) limited the pollutant emissions everywhere in the United States.

In France (1996), the Air and Rational Use of Energy Act (LAURE, by its French acronym) made it mandatory for the government to monitor and inform the public about the status of the air quality in the country. The effect of the law, among others, was to encourage the creation of various tools for the planning and organization of actions at different regional scales, which allowed the creation of Regional Air Quality Plans. The ultimate objectives of Regional Air Quality Plans were to decrease the pollutant concentration in the cities and to define alert procedures.

The first European directive was released in 1999. The objective of this document was to limit the concentration values for sulphur dioxide, nitrogen dioxide and oxides of nitrogen, particulate matter and lead in ambient air (DIRECTIVE, 1999). In 2008, the European Commission released a new directive on ambient air quality and cleaner air for Europe in which the following elements were included: i) Merge most of the existing legislation into a single directive without changing the existing air quality objectives. ii) A new air quality target for fine particulate matter ($PM_{2.5}$) that includes a limit value and exposure-related targets. iii) The option to exclude natural sources of pollution when assessing compliance with limit values. iv) Possibility of time extensions of three years for PM_{10} or up to five years for NO_2 and benzene to comply with limit values. In 2015 the new directive (DIRECTIVE, 2015) was introduced, in which several modifications were made to the existing directives. Improvements concerned to the standards for reference methods, data validation and the

[3] Fuel that does not produce visible smoke in a combustion process.

location of sampling points for the assessment of ambient air quality. According to the current legislation, the concentration of particulate matter is limited in the European Union to a daily average of 25 μg m^{-3} for fine particles ($PM_{2.5}$). In the case of PM_{10} concentration the limits are defined in a slightly complex way: a maximum daily average of 50 μg m^{-3} is allowed, and this daily threshold should not be exceeded more than 35 days per year. Finally, the concentration on an annual average cannot exceed 40 μg m^{-3}.

Chapter 3

Dispersion of tracers in the stable atmosphere of a valley opening on a plain

This chapter is a reproduction of Quimbayo-Duarte et al. (2019a)

Abstract

We quantify the impact of a valley-wind system on the transport of passive tracers in the stably-stratified atmosphere of a valley dynamically decoupled from the atmosphere above. The simple configuration of an idealized Alpine-type valley opening onto a plain is considered, for two values of the initial buoyancy frequency and of the valley steepness. The valley-wind system consists of thermally-driven downslope flows that induce a pressure difference between the valley interior and the plain, thereby triggering a down-valley flow. A steady-state regime is eventually reached, at the beginning of which passive tracers are emitted at the valley floor and at different heights above it. The tracer emitted at the valley floor is fully mixed below the height of the maximum speed of the down-valley flow, which behaves like a jet, and remains decoupled from the tracers emitted above. The down-valley flow increases linearly in the along-valley direction y so that, from the conservation of the tracer flux, the tracer concentration decays as $1/y$. A simple theoretical model is proposed to fully account for the down-valley flow and tracer behaviours. The tracer concentration emitted at the valley floor also displays marked oscillations, which are induced by internal gravity waves radiated via a hydraulic-jump process when the downslope flow reaches the

valley floor. The amplitude of the oscillations can be as high as 50% of their mean value, implying that averaged values in an urbanized valley may disguise high instantaneous – and potentially harmful – values.

3.1 Introduction

Under weak synoptic flow, the airflow close to the ground in mountainous areas is driven by thermal winds. These flows develop at sunset in response to the radiative cooling of the ground and in the morning due to ground heating, being downslope and upslope, respectively. During wintertime, downslope flow dominates due to the lower insolation and more pronounced shadowing effects (Largeron and Staquet 2016). Together with radiative cooling, this flow leads to the formation of cold-air pools in valleys, whose role in trapping air pollution has been well-documented (Silcox et al. 2012, Whiteman et al. 2014). Therefore, under a wintertime anticyclonic regime, urbanized valleys always experience high air pollution levels (Brulfert et al. 2005), particularly for PM_{10} (particulate matter of aerodynamical diameter smaller than 10 μm). When the anticyclonic regime persists for several days, as is common, the thermal structure within the valley eventually displays a vertical temperature gradient of positive sign (referred to as an inversion layer) extending throughout the valley depth. These inversion layers are persistent during the whole anticyclonic period, apart from the region immediately above the ground, which can be eroded due to convection around midday. Thermal stratification and thermally-driven flows are therefore determinant in controlling the distribution of pollutants, once emitted, in the atmosphere of a valley under wintertime anticyclonic conditions.

While the formation, persistence and destruction of inversion layers, along with the associated evolution of thermally-driven winds, have been examined in several studies, both using data from field campaigns (e.g. Whiteman et al. 2004, Lareau et al. 2013) and from numerical modelling (e.g. Largeron and Staquet 2016), their impact on pollutant transport has received less attention. When the pollutant is considered to be passive, as is assumed to be valid for PM_{10} herein, computations of mass fluxes already provide useful pointers on the fate of pollutants. However, what matters at a given site is the spatial distribution of pollutants and how the thermal and wind structure control that distribution. A specific study involving passive tracer transport is required for this purpose. This is the aim of the present work, using numerical modelling of a three-dimensional idealized valley.

Previous numerical modelling studies aiming at relating the atmospheric dynamics and passive tracer transport in mountainous terrain were first conducted by considering a quasi two-dimensional valley, namely with no change along the valley axis. Anquetin et al. (1999) presented results describing the influence of seasonal variations (summertime and wintertime) on the mechanisms responsible for inversion layers, and their consequences on pollutant trapping within valleys. Chemel and Burns (2015) investigated the transport and mixing of pollutants into the stable atmosphere of a valley when the emission sources are located along the slopes. The authors noted that downslope flows transport pollutants into the valley to depths that depend on the temperature deficit of the downslope flows. Rendón et al. (2014) showed that, when a temperature inversion is present, the warming associated with the heat island created by urban areas affects the concentration field of passive tracers by accelerating the break-up of the temperature inversion. Lang et al. (2015) investigated daytime air pollution over complex terrain in a set of two parallel valleys (i.e. three parallel ridges) of varying valley-floor altitude in the cross-valley direction. Results showed that the differences in thermally-driven flows and their impact on tracer transport are highly sensitive to the difference in altitude of the different valley floors.

Due to the two-dimensional geometry considered in previous studies, the role of the along-valley flow on pollutant transport could not be examined. Three-dimensional idealized topographies were considered recently in a few numerical modelling studies. Wagner et al. (2014) considered a valley in between two ridges opening onto a plain for daytime convective conditions. The analysis of mass-flux budgets and forward trajectories indicated that mass is transported three to four times more effectively from the surface to the free atmosphere over valleys than over flat terrain and that vertical transport is greater for deep and narrow valleys. Lehner and Gohm (2010b) performed numerical simulations using both two- and three-dimensional terrain configurations to investigate the influence of vertical inhomogeneities in the thermal stratification and vegetation cover on slope-wind circulations and tracer transport. The authors concluded that the increase in the albedo causes a reduction of the mass flux in the slope flow, directly affecting tracer transport. Cuxart and Jiménez (2007) used a three-dimensional numerical model to simulate a low-level jet developing over a gentle slope, based on field observations from the SABLES-98 field campaign over the northern Spanish plateau. The model was able to reproduce the two-layer structure of the jet observed during the campaign. This jet structure consists of two turbulent layers separated by a change of the temperature gradient at the height where the jet maximum is located. A passive tracer was used to track the mass exchange between the two layers, leading to the conclusion that it is very small.

The present work relies on three-dimensional numerical simulations of an idealized Alpine-type valley opening onto a plain for wintertime stable atmospheric conditions. It is based on Arduini et al. (2016) who considered the same valley configuration for one set of the physical parameters and no passive tracer. The main objective is to characterize the role of downslope and down-valley flows on the transport of passive tracers released at different locations, both on the valley floor and above it. The numerical set-up is presented in Sect. 3.2. The dynamics of the downslope and down-valley flows are reported in Sect. 3.3 and their impact on passive tracer transport is discussed in Sect. 3.4. A summary and conclusions are given in Sect. 3.5.

3.2 Methods

3.2.1 Numerical Model

We use the Weather Research and Forecasting (WRF) numerical model (Peckham et al., 2012), version 3.4.1, which is a fully compressible, non-hydrostatic model that uses a hydrostatic pressure terrain-following vertical coordinate and a staggered grid of Arakawa-C type. The model was run using a large-eddy simulation (LES) configuration. The LES formulation computes the large-scale turbulent motions by solving the filtered three-dimensional Navier–Stokes equations, while the small-scale motions are parametrized using a subgrid-scale (SGS) model. The 1.5-order turbulent kinetic energy closure of Deardorff (1980) was used to model these SGS motions, with the modification proposed by Scotti et al. (1993) to account for the strong anisotropy of the grid along the slope close to the ground. The WRF model is coupled with a chemistry module (WRF-Chem), which is capable of simulating the transport, mixing and chemical transformation of trace gases and aerosols. In the present case, only the transport of passive tracers is considered.

3.2.2 Topography of the Valley

The topography is an idealized U-shape valley opening onto a plain (see Fig. 3.1a). All points have been assigned the geographical coordinates of 45.92°N and 6.87°E, a position located in the Chamonix valley, a typical valley in the French Northern Alps. The idealized valley is oriented south–north, along the y-direction. The topography is similar to that proposed

by Rampanelli et al. (2004), which is symmetric with respect to the vertical plane $y = 0$ to facilitate the implementation of the boundary conditions on the north and south sides. Only the southern half of the domain will be considered. In the following, the *beginning of the valley* refers to the $y = 0$ plane. The analytical expression for the height of the terrain is given by

$$h(x,y) = H\, h_x(x)\, h_y(y) + h_0, \tag{3.1}$$

where

$$h_x(x) = \begin{cases} [1-\cos(\pi\,(|x|-L_x)/S_x)]/2 & \text{for} \quad L_x \le |x| \le S_x + L_x \\ 0 & \text{for} \quad |x| < L_x \\ 1 & \text{for} \quad |x| > S_x + L_x \end{cases} \tag{3.2}$$

and

$$h_y(y) = \begin{cases} [1+\cos(\pi\,(|y|-L_y)/S_y)]/2 & \text{for} \quad L_y < |y| \le S_y + L_y \\ 0 & \text{for} \quad |y| > L_y + S_y \\ 1 & \text{for} \quad |y| \le L_y \end{cases} . \tag{3.3}$$

The valley depth H is equal to 800 m, which is also the altitude above the valley floor of the plateaux extending symmetrically on both sides of the valley in the cross-valley direction x (Fig. 3.1a). The length of the valley in the along-valley direction L_y is equal to 6 km and, together with the length of the sloping sidewall in that direction $S_y = 5$ km, the total length of the valley is equal to 11 km (Fig. 3.1b). The position where the plain starts is referred to as *the valley exit*. The valley floor half-width is equal to $L_x = 720$ m (in the cross-valley direction x) and is set at $h_0 = 1000$ m above sea level (a.s.l.).

Two topographies are considered, only differing in the steepness and length of the sloping sidewall in the cross-valley direction S_x. For the first topography, referred to as T1, the maximum slope angle is 16.7° and $S_x = 4200$ m. This is the topography considered in Arduini et al. (2016). For the second topography, denoted T2, the maximum slope angle is 8.3° and $S_x = 8600$ m (Fig. 3.1c).

3.2.3 Initial Conditions

The numerical simulations use a stable atmosphere, starting one hour before sunset on a winter day (21 December) and lasting either 6 or 8 h. At the initial time, the vertical gradient of the (virtual) potential temperature profile $\partial\theta_v/\partial z$ is constant and no flow imposed. Therefore, the atmosphere of a winter night under decoupled conditions with the synoptic flow is simulated.

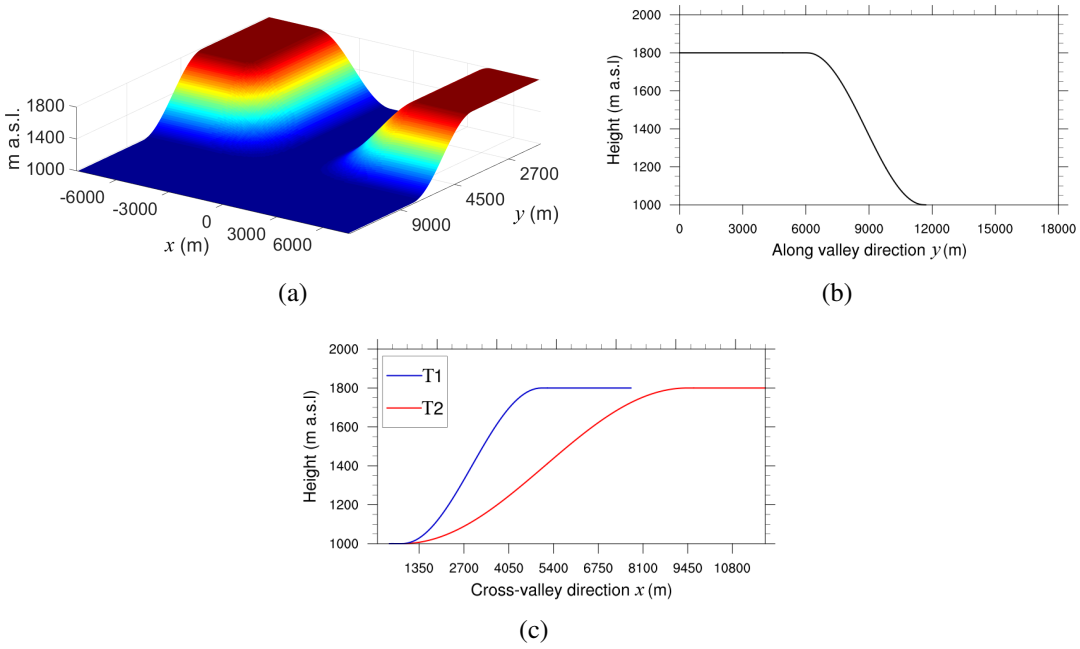

Fig. 3.1 *a) Three-dimensional view of topography T1. b) Terrain height in the along-valley direction at $x = 7$ km from the valley centre. c) Terrain height in the cross-valley direction for $0 \leq y \leq 6$ km, for T1 and T2. The numerical domain is symmetric with respect to the plane $y = 0$ and only its southern part ($y \geq 0$) is displayed in frames a) and b).*

A relatively dry atmosphere is considered using a constant relative humidity value of 40% at the initial time. Two values of the initial stratification are considered, either $\partial\theta_v/\partial z = 1.5$ K km^{-1} associated with the buoyancy frequency $N_1 = 0.00715\ s^{-1}$, or $\partial\theta_v/\partial z = 6$ K km^{-1} associated with $N_2 = 0.01430\ s^{-1}$; the buoyancy (or Brunt-Väisälä) frequency is defined by $N^2 = (g/\theta_{v,ref})\partial\theta_v/\partial z$, where g is the acceleration due to gravity and $\theta_{v,ref} = 288$ K is a reference temperature, equal to the near-surface temperature at the initial time. This value can be considered as a typical temperature at that time of the year in the French Alps. Burns and Chemel (2014) conducted a brief study to estimate the near-surface temperature in the area of the Chamonix valley during one week in January 2003. The near-surface temperature (at 2 m above the ground level) at 1600 local time consistently showed a value of the virtual potential temperature close to 288 K (namely 279.3 K for the associated potential temperature, for a relative humidity of 40%), which accounts for the value of $\theta_{v,ref}$ in the present set of simulations.

Three numerical simulations have been performed, different in either the topography (T1 or T2) or the initial stratification (N_1 or N_2). In simulation S1, topography T1 is used with stratification N_1; simulation S2 differs from S1 through the topography, which is T2;

simulation S3 differs from S1 through the buoyancy frequency, which is N_2 (see Table 3.1). In Arduini et al. (2016) only simulation S1 was considered (and the modification of the SGS model proposed by Scotti et al. (1993) was not implemented).

Simulations							
Sim.	Topo	Slope length (m)	Max slope ang. (°)	$\partial\theta_v/\partial z$ (K km^{-1})	N (rad s^{-1})	Grid pts (x)	Grid pts (y)
S1	T1	4200	8.3	1.5	7.15×10^{-3}	172	361
S2	T2	8600	16.7	1.5	7.15×10^{-3}	270	361
S3	T1	4200	8.3	6	1.43×10^{-2}	172	361

Table 3.1 *Main parameters of the simulations. The number of grid points indicated is that of the inner domain, the horizontal resolution being 90 m. In the outer domain, the horizontal resolution is set to 270 m.*

3.2.4 Boundary Conditions

All simulations were run in a one-way nested domain configuration using two domains. In the outer domain, periodic boundary conditions are imposed at the east and west boundaries. On the east and west sides of the valley, the plateaux are long enough (3000 m) to prevent the influence of these boundary conditions on the inner domain. As for the boundaries in the y-direction, open boundary conditions are imposed at the north and south boundaries of the outer domain, thanks to the symmetry with respect to the plane $y = 0$ of T1 and T2. In the inner domain, the boundary conditions are provided by the fields computed in the outer domain and are updated every outer-domain timestep. No information passes from the inner to the outer domain due to the one-way nesting.

To prevent wave reflection at the top of the domain, located at 12 km a.s.l., a Rayleigh damping layer (Klemp et al., 2008) is set using a damping depth equal to 4000 m and a damping coefficient equal to 0.2 s^{-1}. At the ground the usual impermeability condition is used. The atmospheric surface-layer is modelled by the revised MM5 Monin–Obukhov surface-layer scheme proposed by Jiménez et al. (2012); it provides in particular the bottom boundary conditions for the turbulent fluxes. Radiative transfer is considered using the Rapid Radiative Transfer Model for longwave radiation (Mlawer et al., 1997) and the scheme proposed by Dudhia (1989) for shortwave radiation. The soil type is "silty clay loam", which is consistent with the typical Alpine valley landscape in the absence of snow. The skin temperature is initialized through an extrapolation of the temperature in the first three layers above the surface.

3.2.5 Numerical Parameters

The size of the inner domain is 15 km $\times$ 32 km in the x- and y-directions, respectively, for T1 and 25 km $\times$ 32 km for T2, with a grid size of 90 m in both directions. The size of the domain of interest is therefore equal to 16 km in the y-direction, as discussed above. The outer domain is two times larger than the counterpart inner domain in the x-direction and three times larger in the y-direction, with a horizontal grid size of 270 m. Both domains share the same vertical discretization with 100 grid points: the first mass point is at 1.7 m above the surface and the vertical coordinate is stretched so that the first 20 m are discretized with 10 grid points and the first 100 m with 26 grid points. The timestep is equal to 0.075 s for the inner domain, and is three times larger for the outer domain. A summary of the physical and numerical parameters of simulations S1, S2 and S3 is provided in Table 3.1.

3.2.6 Initialization of the Passive Tracer

The tracers used in the present experiment are passive (with no chemical reaction), the physical properties of the tracers being those of dry air so that no deposition effect needs to be modelled. Four different emission zones (Z_i) with the same surface area are defined along the valley axis, centred at 3, 5, 7, and 9 km from the beginning of the valley (see Fig. 3.2). Each emission zone at ground level is replicated at four different levels above it implying that 16 tracers are emitted for each simulation. Each zone Z_i is composed of an array of 12×16 grid cells in the north–south and east–west direction, respectively, and the tracer emission is distributed in a single grid cell along the vertical. The emission rate Q over a given zone Z_i is constant in time and equal to 6.56×10^{-7} kg s^{-1}. An initial background tracer concentration is imposed in the whole domain, with value 1.25×10^{-12} kg m^{-3}. Hereafter each tracer is named as $TrSn_{i,j}$, where $1 \leq n \leq 3$ denotes the simulation number in which the emission has been released, $1 \leq i \leq 4$ and $1 \leq j \leq 4$ refer to the area at the valley bottom and to the height at which the tracer is released, respectively (see Table 3.2). Tracers are released 150 min after the initial time, as justified below.

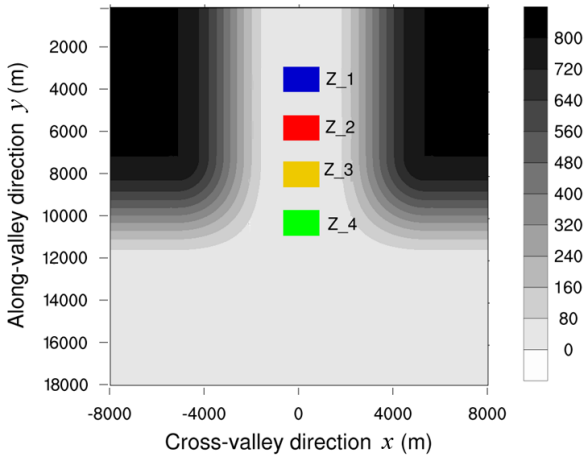

Fig. 3.2 *Locations of the passive tracer emissions. Each colour zone (Z_i) corresponds to an emission source, all zones having the same area (1440 m x 1080 m). Four different tracers were emitted in each zone at different levels (0, 95 m, 280 m and 415 m above the ground). The contours displayed are those for topography T1.*

3.3 Analysis of the Valley-Wind System

The flow behaviour for the parameters of simulation S1 has been studied in detail by Arduini et al. (2016), with a focus on the impact of the valley-wind system on the development of the cold-air pool. Here, the analysis of the flow dynamics for S1 is related to the flow properties that affect the passive scalar behaviour: the oscillations of the velocity components (Sect. 3.3.2), the vertical structure of the cold-air pool (Sect. 3.3.3) and the mixing regions (Sect. 3.3.4). A sensitivity study is next conducted (Sect. 3.3.5) for a slope angle of the valley twice smaller (simulation S2) and a value of the buoyancy frequency twice larger (simulation S3).

3.3.1 Overall Behaviour of the Flow

During nighttime, a negative buoyant flow is detected over the valley sidewalls. The generation of this downslope flow is produced by a sign reversal in the surface radiative budget over the valley. During the day this budget has a positive sign as a result of shortwave solar radiation. On the late afternoon solar radiation decreases and is eventually overcome by longwave radiation emitted from the ground, leading to surface cooling. The sensible heat flux is then directed from the atmosphere to the ground resulting in a shallow layer of cooler air over the slope surface. This air layer is therefore denser than the air parcels located at the

Emission Sources				
Height above the surface (m)	Z_1 (3 km)	Z_2 (5 km)	Z_3 (7 km)	Z_4 (9 km)
0	$TrSn_{1,1}$	$TrSn_{2,1}$	$TrSn_{3,1}$	$TrSn_{4,1}$
95	$TrSn_{1,2}$	$TrSn_{2,2}$	$TrSn_{3,2}$	$TrSn_{4,2}$
280	$TrSn_{1,3}$	$TrSn_{2,3}$	$TrSn_{3,3}$	$TrSn_{4,3}$
415	$TrSn_{1,4}$	$TrSn_{2,4}$	$TrSn_{3,4}$	$TrSn_{4,4}$

Table 3.2 *Location of the tracers released in the simulations. Each tracer is named $TrSn_{i,j}$, where $1 \leq n \leq 3$ is the simulation number, $1 \leq i \leq 4$ is the zone number on the valley bottom and $1 \leq j \leq 4$ is the height index at which the tracer is released over the valley bottom. All zones are horizontal and centred with respect to the valley axis. For $i = 1$, Z_i is also centred with respect to the position $y = 3$ km; for $i = 2$, $y = 5$ km; for $i = 3$, $y = 7$ km and for $i = 4$, $y = 9$ km. For $j = 1$, the tracer is released at the valley bottom; for $j = 2$, at 95 m above the valley bottom; for $j = 3$, at 280 m and for $j = 4$, at 415 m. The zones correspond to the colour areas Z_i in Fig. 3.2; each zone has an area of 1440 × 1080 km^2.*

same altitude further away from the slope; as a result, a downslope flow develops following the valley shape.

The downslope flow speed, denoted U_s, follows a jet structure normal to the slope, with a maximum value (jet nose) reached at about 5 m above the ground in simulation S1 (not shown). Time series of U_s are presented in Fig. 3.3a for S1 at different positions along the valley axis, at a height of 5 m above the ground and for x = 2000 m (close to the bottom of the slope). Fig. 3.3a shows that U_s develops within the first hour with a growth rate almost independent of the position along the valley axis. This growth rate is controlled by radiative cooling and the stratification, which are independent of the along-valley direction. In contrast, U_s reaches a maximum value that depends on the length of the slope (which is the same at $y = 3$ and $y = 6$ km but shorter at $y = 9$ km). This maximum value is reached between 60 and 120 min, and U_s next decays and reaches a quasi-steady state.

The advection of cold air along the slopes by the downslope flows, and subsequent upward transport from the convergence of the downslope flows at the valley centre, create a cold-air pool in the valley. The resulting temperature difference, and therefore pressure difference through hydrostatic balance, between the valley interior and the plain triggers a down-valley flow, with speed denoted V (see Fig. 3.3b).

As opposed to U_s, the rate at which V develops is strongly dependent on the position along the valley axis: it is larger close to the valley exit, where the pressure gradient between the valley and the plain is largest and decays as one moves towards the beginning of the valley (note that V vanishes for $y = 0$ due to the symmetry of the topography with respect to

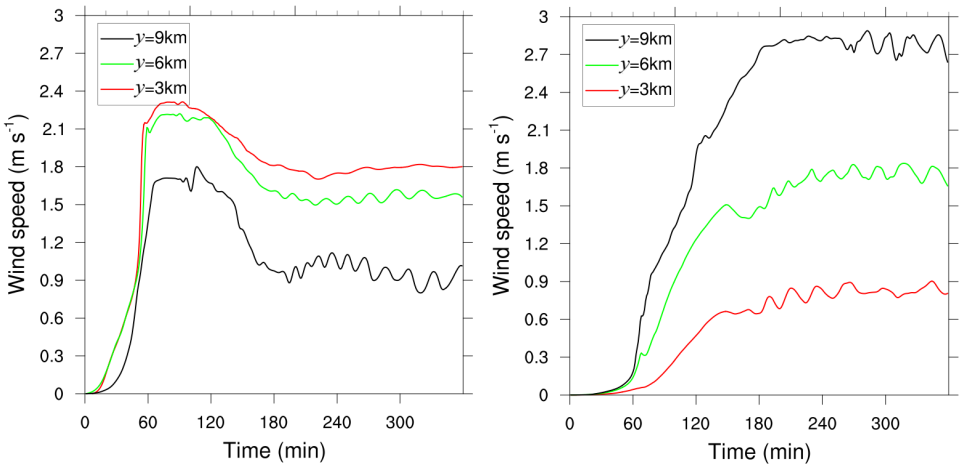

Fig. 3.3 *a) Time series of the downslope flow speed at three different locations along the valley axis. For the three locations, $x = 2000$ m and $z = 5$ m above the ground. b) Time series of the down-valley flow speed averaged over the valley bottom at 5 m above the bottom at the same three locations along the valley axis. Results are shown for simulation S1.*

the $y = 0$ vertical plane). The down-valley flow is therefore generated at the valley exit and, by mass conservation, further develops inside the valley; this implies that a return flow should form as well at higher altitude. Consistent with its generation mechanism, this down-valley flow exists only within the cold-air pool.

The downslope and down-valley flows eventually reach a quasi-steady regime whose origin is discussed in Arduini et al. (2016). This regime is reached after 3 h, a duration that depends on the ratio of the length to the height of the valley and on the buoyancy frequency (see also Schmidli and Rotunno, 2015). Marked temporal oscillations in the time series of U_s and V are noticeable during the quasi-steady regime, which are analyzed in the next section. A simple model of the down-valley flow speed during the quasi-steady regime is proposed in Sect. 3.4.4.

3.3.2 Analysis of the Flow Oscillations

As shown in Sect. 3.4, the oscillations of the down-valley flow speed have an impact on the passive tracer concentration. We investigate here the origin of these oscillations, for the downslope and down-valley flows.

Energy spectra of U_s and V have been computed from the time series displayed in Fig. 3.3 when the quasi-steady regime is reached (see Fig. 3.4). The downslope flow speed U_s displays two main peaks whatever the value of the y-location along the valley axis, for 3.1 $\times$ 10^{-4} Hz and 6.2 $\times$ 10^{-4} Hz (owing to the resolution in frequency of the spectrum, equal to 1.04 $\times$ 10^{-4} Hz). Only the latter peak is convincingly detected in the spectra of the time series of V whatever the y-location.

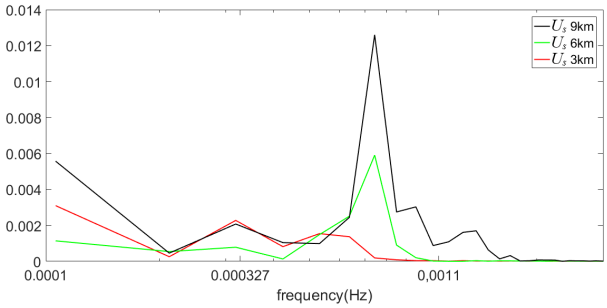

(a)

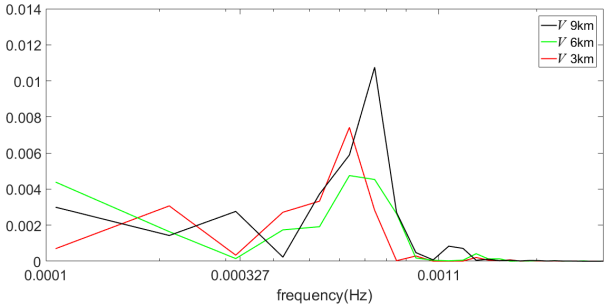

(b)

Fig. 3.4 *a) Energy spectrum of the downslope flow speed (U_s) (a) and down-valley flow speed (V) (b) from 200 to 360 min, for the time series displayed in Fig. 3.3. A log-log scale is used. The frequency predicted by McNider's model is indicated with a tickmark at* 3.27 $\times$ 10^{-4} *Hz. Results are shown for simulation S1.*

The smallest frequency peak can be accounted for by the combination of the effects of radiative cooling from the ground and stratification, following a simple model proposed by McNider (1982). According to this model, valid for a constant slope of infinite extent in a uniformly stratified atmosphere, a fluid particle advected by the downslope flow oscillates at a frequency equal to $N \sin \alpha / 2\pi$, where α is the slope angle and N, the (constant) value of the buoyancy frequency. Using for α the maximum slope angle in the y-plane the downslope flow is considered and for N its value at the initial time, as in Chemel et al. (2009b), a value of 3.27 $\times$ 10^{-4} Hz is obtained for the oscillating frequency (taking $\alpha = 16.7^\circ$ for $y = 3$ and

6 km and $N = 7.15 \times 10^{-3}$ rad s^{-1}). This value is indicated in Figs. 3.4a,b and matches quite well the first frequency peak for U_s.

The second frequency peak can be explained by relying again on the analysis of Chemel et al. (2009b). It is indeed the signature of an internal gravity wave field emitted by the downslope flow when it experiences a hydraulic jump at the bottom of the slope (see also Renfrew, 2004). The period associated with this frequency is about 27 min. To attest that internal gravity waves with this period are indeed radiated, a (t,z) diagram of the vertical velocity component is displayed in Fig. 3.5 at a mid-slope location and at $y = 3$ km. A propagating internal gravity wave pattern is clearly detected, whose period is in agreement with that associated with the second frequency peak.

We therefore conclude that the oscillations in the down-valley flow speed V result from the emission of this internal gravity wave field while the downslope flow speed U_s is also subject to McNider's oscillations.

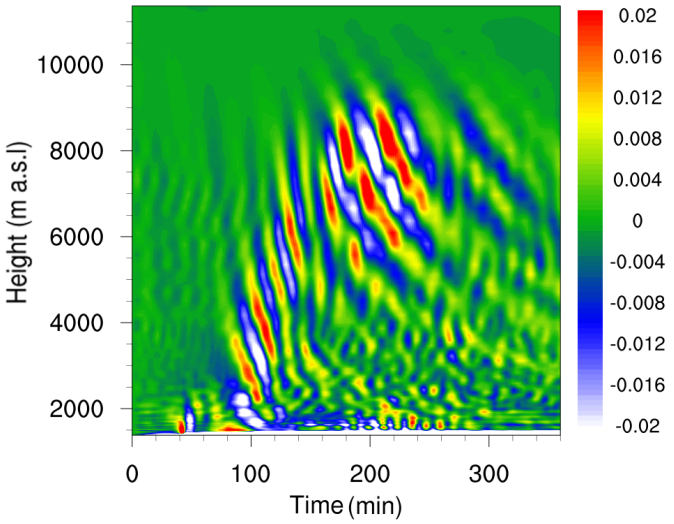

Fig. 3.5 *(t,z) diagram of the vertical velocity component [m s^{-1}] at $x = -2850$ m (mid-slope) and $y = 3000$ m. Results are shown for simulation S1.*

3.3.3 Vertical Profiles of the Down-Valley Flow Speed and of the Absolute Temperature Along the Valley Axis

The vertical profiles of the down-valley flow speed and of the absolute temperature, along with the counterpart buoyancy frequency, are displayed in Fig. 3.6 at different positions along the valley axis, at $t = 360$ min.

As shown by Arduini et al. (2016), the height of the cold-air pool created by the downslope flow (and subsequently modified by the development of the along-valley flow) decreases from the beginning of the valley to the valley exit as a result of the decreasing depth of the valley. This is also attested in Fig. 3.7a, which displays streamlines in the vertical $x = 0$ plane. The down-valley flow existing within the cold-air pool, it behaves like a "flow in a pipe", the height of the pipe being set by that of the cold-air pool. As a result, the down-valley flow speed increases towards the valley exit (see the streamline pattern in Fig. 3.7a). Figure 3.6a shows that a jet-like profile develops along the valley axis, which is fully developed at the valley exit, the jet maximum being located at about 40 m above the ground. Whatever the $y-$location, the vertical profile of the flow speed reverses around $z = 1400$ m a.s.l. up to the plateau height, which ensures mass conservation.

As shown in Fig. 3.6b, the temperature profile displays a very strong ground-based inversion, controlled by radiative cooling at the ground, of about 0.1 K m^{-1} up to the height at which the down-valley flow speed reaches a maximum. This value is an average, over the valley floor and over the first layer, of the absolute temperature vertical gradient at the end of the simulation. The corresponding value of the buoyancy frequency N is very large as well, of about 0.06 rad s^{-1} (close to the ground it may even reach values as high as 0.16 rad s^{-1}, namely 0.7 K m^{-1}). The temperature profile reverses at an altitude around 1150 m a.s.l. and becomes y-independent at the altitude where the down-valley flow speed changes sign (at about 1400 m a.s.l.), slowly converging above towards the initial temperature profile. Figure 3.6b also shows that the air in the cold-air pool is warmer close to the valley exit than at $y = 3$ km. Indeed, the larger down-valley flow speed at the valley exit results in a larger sensitive heat flux at 9 km than at 3 km; therefore mixing with the air coming from the slopes is stronger at the valley exit than at 3 km (Arduini et al., 2016, showed that there is very little contribution from subsidence).

Fig. 3.6b shows that the buoyancy frequency N in the cold-air pool is larger at $y = 9$ km than at $y = 3$ km, because of the decrease in the cold-air pool height. This is attested in Fig. 3.7a below, which displays streamlines inside the valley during the quasi-steady regime,

recalling that streamlines are also lines of constant potential temperature in this regime if cooling effects are neglected. Figure 3.6b also shows that N displays vertical oscillations, attesting again to the presence of internal gravity waves. The vertical wavelength is about 100 m in the cold-air pool, consistent with N being ten times larger in the cold-air pool than above the valley (using results from Largeron et al. (2013a) to estimate the wave frequency, Fig. 3.5 to estimate the vertical wavelength above the valley and the dispersion relation of internal gravity waves).

As indicated in Fig. 3.6b, three layers can be defined along the vertical. These layers will help, in Sect. 3.4, to characterize the transport properties of the flow. The first layer extends from the ground to the height of the jet maximum (about 40 m above ground level); the second layer surmounts the first layer and extends up to the height of the reversal of the temperature, namely the location at which dT/dz vanishes, at about 1150 m a.s.l.; the third layer extends from the top of the second layer to the height where the down-valley flow speed reverses, at about 1400 m a.s.l.

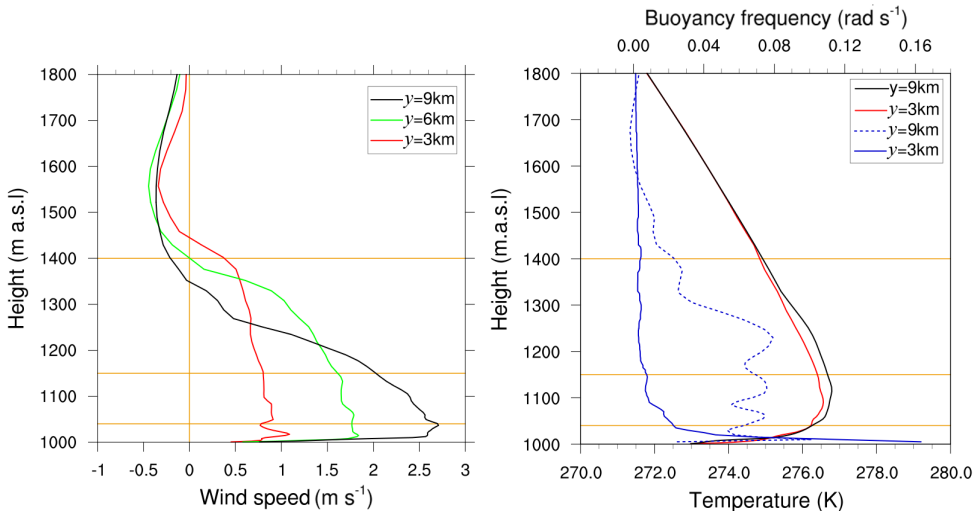

Fig. 3.6 *Vertical profiles of the down-valley flow speed (a) and of the absolute temperature (b) averaged over the valley floor at different positions along the valley axis, at t = 360 min. Blue lines in b) correspond to the buoyancy frequency at 3 km (solid line) and 9 km (dashed line) from the beginning of the valley averaged over the last hour of simulation. The horizontal orange lines indicate the top of the different layers defined in Sect. 3.3.3. Results are shown for simulation S1.*

3.3.4 Regions of Turbulence

The identification of the regions where turbulence occurs is an essential step in the understanding of the passive scalar behaviour. Turbulence kinetic energy (TKE) is a good indicator of turbulence and contours of TKE for S1 are displayed in a vertical plane containing the valley axis in Fig. 3.7a; a zoom over the first 50 m above the valley floor is shown in Fig. 3.7b.

The development of the down-valley flow displayed in Fig. 3.6a is reminiscent of that of a low-level jet during the evening transition in a stably stratified atmosphere (e.g. Banta et al., 2003), the temporal development of the low-level jet becoming here a spatial development along the y-direction. As shown by several authors (see Banta et al., 2003, and references therein), turbulence is generated in the layer between the ground and the maximum of the low-level jet, as a result of the strong shear in the jet. Figure 3.7b shows that this is also the case for simulation S1.

Turbulent regions of a flow can be identified using the local Richardson number,

$$Ri = \frac{\frac{g}{\theta_{v,ref}} \frac{\partial \langle \theta \rangle}{\partial z}}{\left(\frac{\partial \langle U \rangle}{\partial z}\right)^2 + \left(\frac{\partial \langle V \rangle}{\partial z}\right)^2}. \tag{3.4}$$

In Eq. 3.4, the $<>$ symbol refers to a spatial average over the valley floor and a temporal average over the last 30 minutes of the simulation. For a steady parallel shear flow in a stably stratified fluid, a necessary condition for instability is $Ri < 1/4$ somewhere in the flow (see Drazin and Reid, 1982). This criterion is actually a good indicator of turbulent regions for any shear flow and is widely used in the literature. Figure 3.7b shows that the condition $Ri < 1/4$ is satisfied below the jet maximum. We note that the TKE value is of the order of 0.1 m^2 s^{-2}, which is comparable to the lowest values recorded in the field experiments reported in Banta et al. (2003).

Figure 3.7a displays another turbulent region, which is associated with the upper part of the down-valley flow in the cold-air pool. The streamlines show that a strong shear exists there, as evidenced by a local Richardson number smaller than $1/4$ and, especially, by TKE values being up to seven times larger than those below the jet maximum.

Apart from these two turbulent regions, the flow can be considered as laminar, with Ri $\sim$ 10. This implies that the flow below the jet maximum is decoupled from the flow above it,

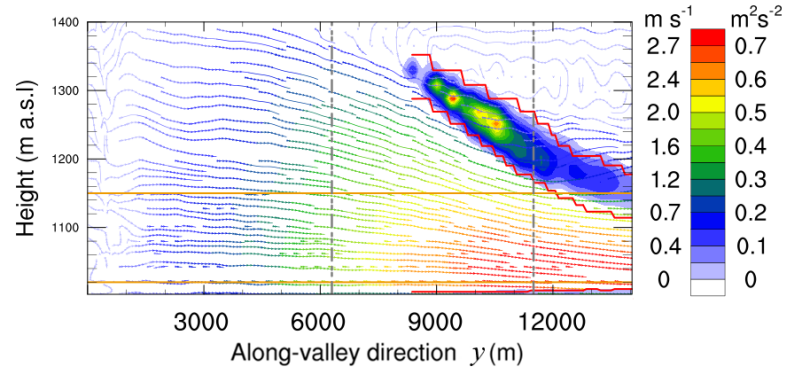

(a)

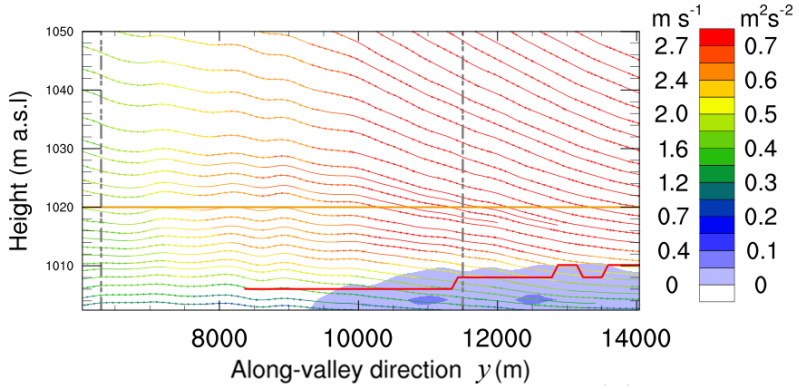

(b)

Fig. 3.7 *(a) Contour plot of the turbulence kinetic energy (TKE) (with values indicated in the right column of the colour map) overlaid with streamlines along the valley axis at 360 minutes into the simulation. The colours along the streamlines refer to values of the down-valley flow speed (which are indicated in the left column of the colour map). The regions where Ri, defined by Eq. 3.4, is less than* $1/4$ *are bounded by red lines. (b) Zoom of frame (a) over the TKE region close to the bottom. Results are shown for simulation S1.*

as already noted in Cuxart and Jiménez (2007) for the case of a downslope flow over a gentle slope.

3.3.5 Sensitivity Study

The impact of the slope angle and of the value of the buoyancy frequency on the dynamics of the flow described in the previous section are now briefly analyzed, based on the results of simulations S2 and S3 (see Table 3.1).

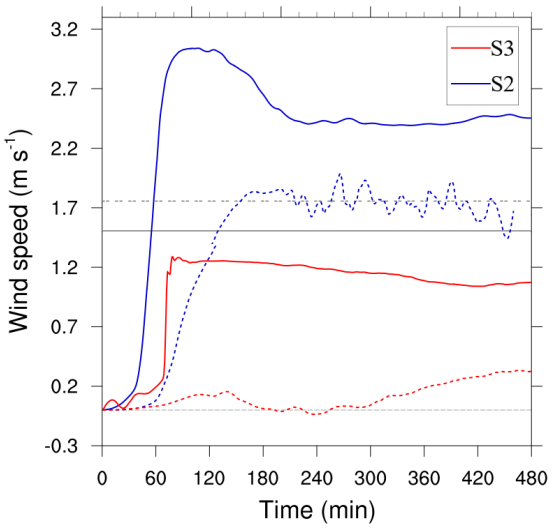

Fig. 3.8 *Solid lines: time series of the velocity U_s [m s^{-1}] at $y = 6$ km and $z = 20$ m above the ground level; $x = 2500$ m for simulations S2 (blue) and $x = 3000$ m for S3 (red). The $x-$position is located outside the region along the slope where the hydraulic jump forms (before it in the downslope direction). Dashed lines: times series of the velocity V [m s^{-1}] at $y = 6$ km, averaged over the valley floor for simulations S2 (blue) and S3 (red). Grey lines denote the values of the U_s (solid line) and V (dashed line) speed in S1 once the quasi-steady state is reached, averaged from 180 to 360 min using the same data than Fig 3.3. The dotted horizontal light-grey line marks the zero value of the velocity.*

Figure 3.8 displays time series of the downslope flow speed U_s and of the down-valley flow speed V at $y = 6$ km for simulations S2 and S3. Despite the gentler slope in S2 than in S1, implying that the along-slope component of the gravity vector is smaller in the former case than in the latter case, U_s reaches a higher quasi-steady value in S2 than in S1. This behaviour can be explained as follows (Zardi and Whiteman, 2013). The sensible heat flux close to the slope leads to a cooling of the fluid layer and, therefore, to its downward motion along the slope. For the same atmospheric conditions, an air parcel travelling over a longer slope (as in S2) will loose more heat than along a shorter slope (as in S1) for a given difference in altitude travelled by the fluid parcel. The speed at the bottom of the slope reached by the fluid parcel will therefore be larger for the shallower slope (S2) than for the steeper slope (S1) as the plateau height is the same in both simulations. In the present case, the quasi-steady value of U_s for S2 is about 50% larger than that for S1 (compare Fig. 3.3a and Fig. 3.8).

The larger U_s speed in S2 leads to a greater mass flux of a slightly colder air-mass. However, since the T2 topography is associated with a larger valley volume than the T1 topography, the height of the cold-air pool is eventually smaller in S2 than in S1 (compare Fig. 3.7a and 3.10a). As a result, the maximum value of the jet speed at the valley exit is

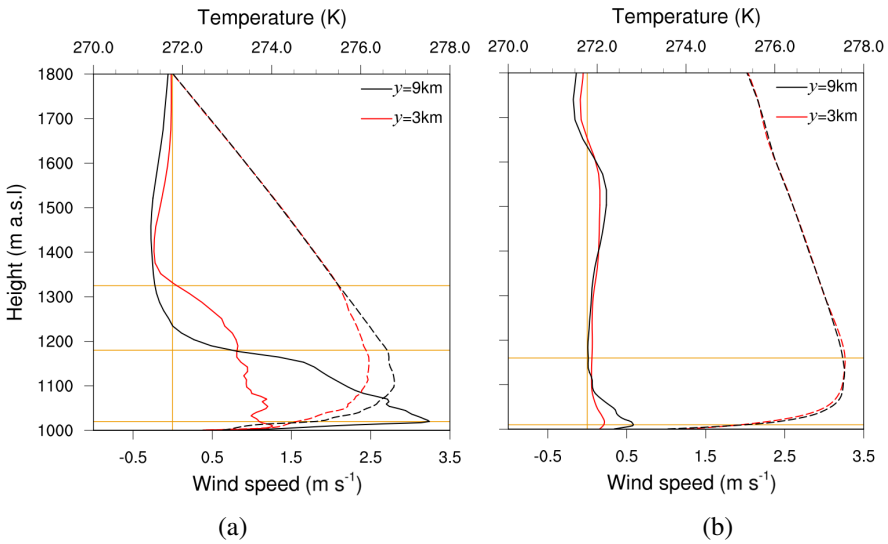

Fig. 3.9 *Vertical profile of the down-valley flow speed (solid lines) and of the temperature (dashed lines) at $t = 360$ min, for $y = 3$ km (red colour) and $y = 9$ km (black colour). Horizontal orange lines denote the height of the layers detected inside the flow. a) Simulation S2 and b) Simulation S3. Data were taken at the valley centre in both simulations.*

larger in S2 than in S1 (compare Fig. 3.6a and 3.9a), but the average value over the valley floor is found to be similar (Fig. 3.8).

As for S1, three layers can be defined for S2 from the vertical profiles of V and the temperature (see Fig. 3.9a): a first layer of height 20 m limited by the height of the jet maximum associated with a layer-averaged temperature gradient of about 0.1 $\mathrm{K\,m^{-1}}$, a second layer limited by the top of the ground-based inversion at about 1180 m a.s.l., and a third layer up to the top of the cold-air pool at 1320 m a.s.l.

The turbulent regions of the flow are identified in Fig. 3.10a by contours of TKE and the line associated with the critical value of $1/4$ for the Richardson number. The same two regions as in S1 are recovered, below the jet maximum and at the top of the cold-air pool near the valley exit, where the strongest vertical shear of the down-valley flow speed occurs. However, as opposed to S1, the largest TKE values are encountered here close the ground. These values are about twice larger than in S1, consistent with the larger down-valley flow speed maximum.

The doubling of the value of the buoyancy frequency for S3 has a very strong impact on the valley-wind system. Theoretical models of the downslope flow speed predict that this speed is inversely proportional to the buoyancy frequency (see Prandtl, 1952, McNider,

1982), implying that it should be weaker for S3 than for S1. Fig. 3.8 shows that this is the case, U_s for S3 being 50% smaller than for S2 at the positions considered in this figure. The mass flux associated with the downslope flow is therefore smaller for S3 than for S1 and the topography being the same, the height of the cold-air pool is smaller for S3 than for S1 as well. The cold-air pool in S3 actually coincides with the ground-based inversion (see Fig. 3.9b), implying that the temperature profile hardly varies along the valley axis. As a result, the pressure difference between the valley and the plain is very small and a weak down-valley flow develops, whose maximum speed reaches at most 0.5 m s^{-1} at the valley exit. Only two layers can be identified from the vertical profiles of the down-flow flow speed and the absolute temperature. The first layer is the ground-based inversion and is very thin, about 10-m high, and is associated with the same very strong gradient of temperature as for S1 and S2; the second layer extends up to about 1150 m a.s.l. As expected (see Fig. 3.10b), the down-valley flow speed for S3 does not exhibit any turbulent region and remains localized in a layer close to the ground, about 10-m high, with a value smaller than 1 m s^{-1}.

3.4 Properties of the Tracer Concentration Field

All tracers were emitted 150 min after the initial time, when the along-valley flow is fully developed, to analyze the impact of this flow and of the stable stratification on the tracer behaviour. During the first hour of simulation indeed, a vertical motion is induced inside the valley by the convergence of the downslope flows, which would transport the tracer upwards inside the valley volume if emission were imposed from the initial time.

We recall that the tracers are emitted in four zones along the valley axis, each of them covering a surface area equal to the valley width along the x-direction (1440 m) and extending over 1080 m along the y-direction; for each zone, emission occurs at the valley floor and at three different heights above it (see Table 3.2). These heights have been selected so as to be located inside the highest layer identified in Sect. 3.3.4 for S1, of altitude 1400 m a.s.l.

3.4.1 Overall Behaviour of the Tracer Concentration Along the Valley Axis

Contours of the tracer concentration are displayed in Fig. 3.11 at 360 min into the simulation in the vertical plane $x = 0$ (containing the valley axis) for S1 and S3, along with streamlines.

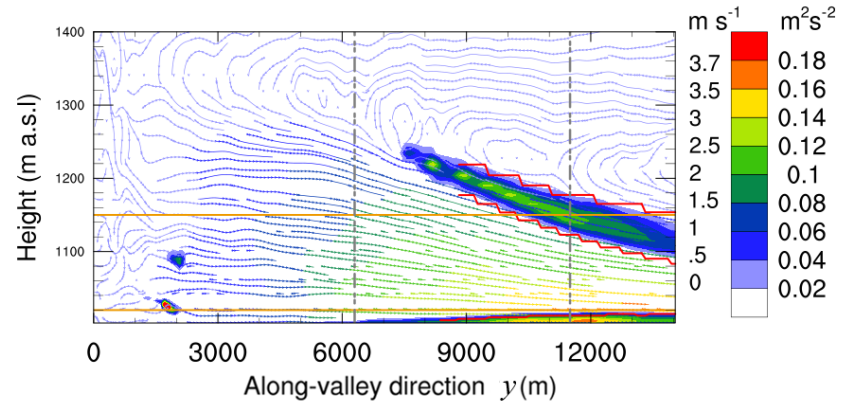

(a)

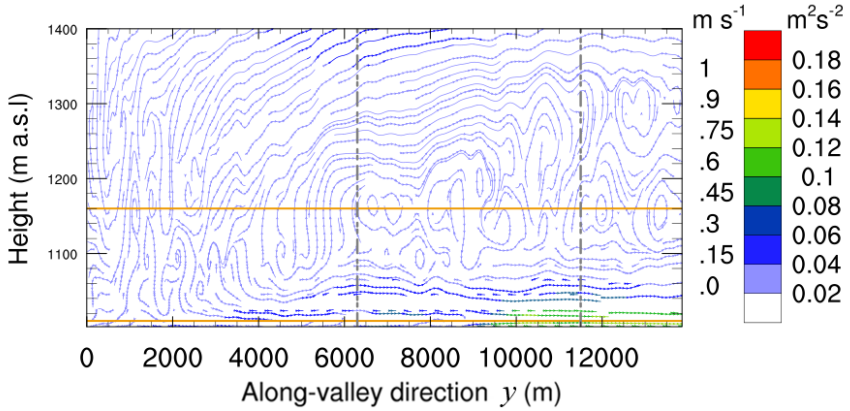

(b)

Fig. 3.10 *Same as Fig. 3.7a: (a) for simulation S2; (b) for simulation S3.*

The emission zone is Z_1 in frames a) to h), with the tracer being emitted at the four different levels mentioned above, and Z_4 in frames (i) and (j).

The tracer is advected by the velocity field, which is mainly contributed by the down-valley flow in the $x = 0$ plane (there is no cross-valley flow in that plane, by symmetry, and the vertical velocity is of much weaker amplitude than the down-valley flow speed). The valley-wind system being quasi-steady once the down-valley flow has fully developed (see Section 3.1), tracer contours closely follow the streamlines of that flow. Since this flow is laminar apart from the two turbulent regions identified in Sect. 3.3.4 for S1, one expects the tracers emitted at different heights to remain decoupled while being advected toward the valley exit; the latter point is clearly illustrated in Fig. 3.11.

For S1 (left column of Fig. 3.11), striking additional features should be noted. The tracer released at the ground (see Fig. 3.11a) spreads vertically but remains trapped below

the first maximum of the down-valley flow speed. In a real valley during wintertime where particulate air pollution is mainly contributed by PM_{10} (which can be modelled as a passive tracer), the latter result could explain the height above the valley floor over which pollution levels are highest during nighttime. Figure 3.11a also shows that the concentration decreases as the valley exit is approached. This results from the tracer concentration to be inversely proportional to the down-valley flow speed (which increases toward the valley exit as already shown), as discussed in the next section.

When emission occurs within the cold-air pool (see Figs. 3.11a, 3.11c and 3.11e), the tracer is advected towards the valley exit. However, the decrease of the concentration along the valley axis implies that, depending upon the emission sources, the superposition of the different tracers at the valley exit may not lead to a concentration higher than inside the valley, closer to the emission source.

When the tracer is emitted at the top of the cold-air pool where the down-valley flow speed is very weak (see Fig. 3.11g), the tracer remains localized at the emission location, as expected, apart from a weak vertical diffusion.

The purpose of Fig. 3.11i is to illustrate the presence of the return flow above the cold-air pool, due to mass conservation. Indeed, at 360 min, the tracer has moved towards the beginning of the valley, as opposed to the tracers at lower altitudes. This figure also shows that the higher is the tracer release altitude the stronger is the vertical diffusion for $y = 3$ km, because the local buoyancy frequency, that is the stratification level, decreases with height (see Fig. 3.6b for $y = 3$ km, the behaviour being similar for $y = 6$ km).

As for S3 (see right column of Fig. 3.11), the passive tracer remains trapped within its emission zone because of the very weak down-valley flow speed, with a weak dispersion along the vertical. As a result, higher concentration levels than for S1 are reached locally at 360 min. This simulation S3 will not be further considered in the remainder of this section.

3.4.2 Temporal Evolution of the Tracer Flux

The total tracer flux across a vertical cross-section of the valley located 2 km downstream from the centre of an emission zone (Z_1, Z_2 or Z_3) is displayed in Fig. 3.12 for S1 and S2. This cross-section, denoted Σ, extends from the valley floor to the top of the cold-air pool, whose height above the valley floor is denoted z_{CAP}.

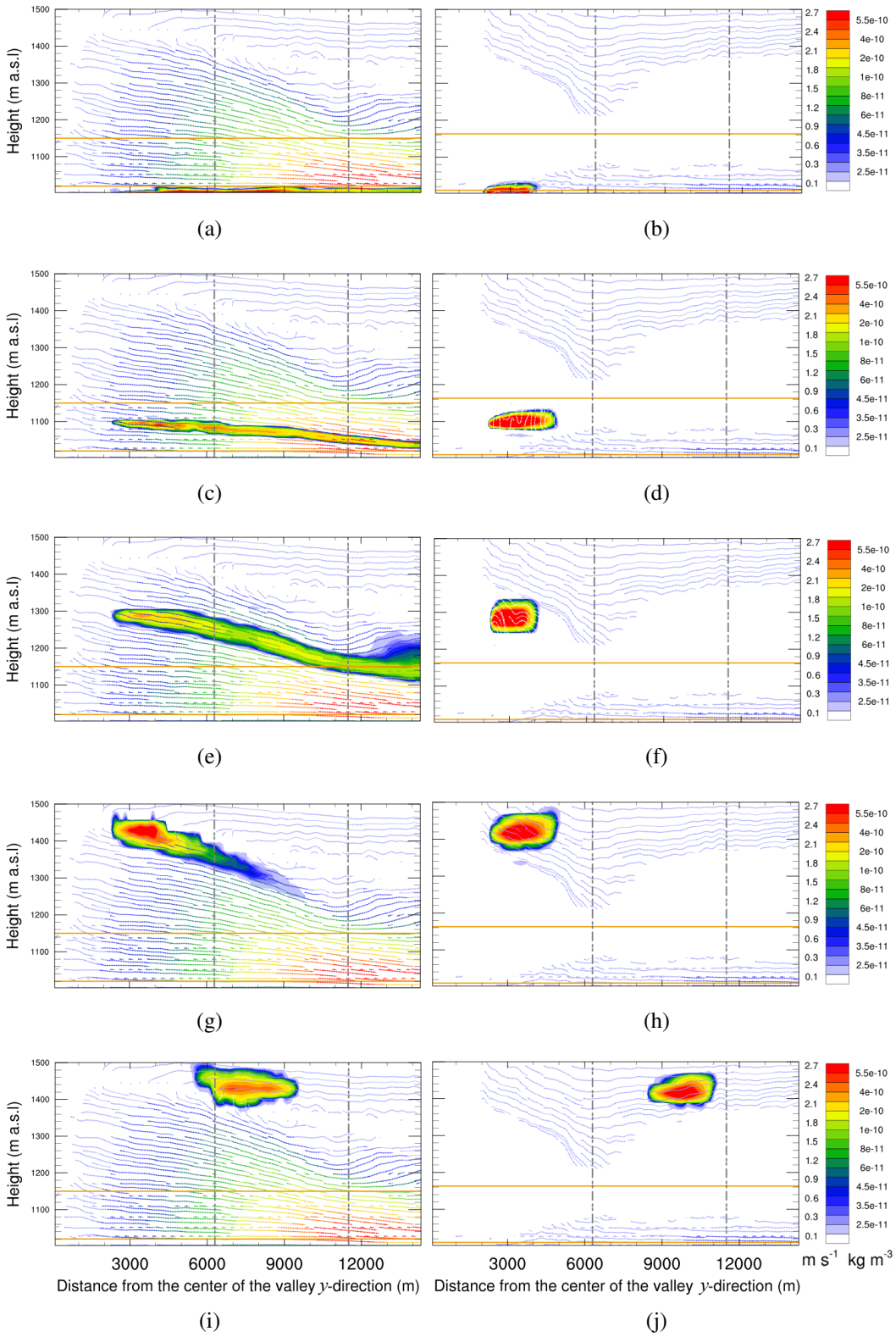

Fig. 3.11 *Contour plots of tracer concentration overlaid with streamlines in the $x = 0$ vertical plane at t = 360 min for simulation S1 (left column) and S3 (right column). In panels a) to h), tracers were released in zone Z_1 at different heights: a) and b) surface level ($TrS1_{1,1}$ and $TrS3_{1,1}$), c) and d) 100 m above the ground ($TrS1_{1,2}$ and $TrS3_{1,2}$), e) and f) 280 m above the ground ($TrS1_{1,3}$ and $TrS3_{1,3}$), g) and h) 415 m above the ground ($TrS1_{1,4}$ and $TrS3_{1,4}$). Panels i) and j) correspond to $TrS1_{4,4}$ and $TrS3_{4,4}$, respectively, released in zone Z_4 and at 415 m above the ground level. The two lower layers identified in Sect. 3.3.3 for S1 and in Sect. 3.3.5 for S3 are indicated with an orange horizontal line for each simulation.*

Since the tracers are released 150 min after the initial time, the tracer flux in Fig. 3.12 starts to grow from this time on. More precisely, the growth starts when the tracer reaches the vertical area Σ and the smaller is the down-valley flow speed the later this growth occurs, namely the closer to the beginning of the valley is the emission zone. The tracer flux eventually reaches the same quasi-steady value (apart from oscillations associated with internal gravity waves) whatever the (y-)position of Σ.

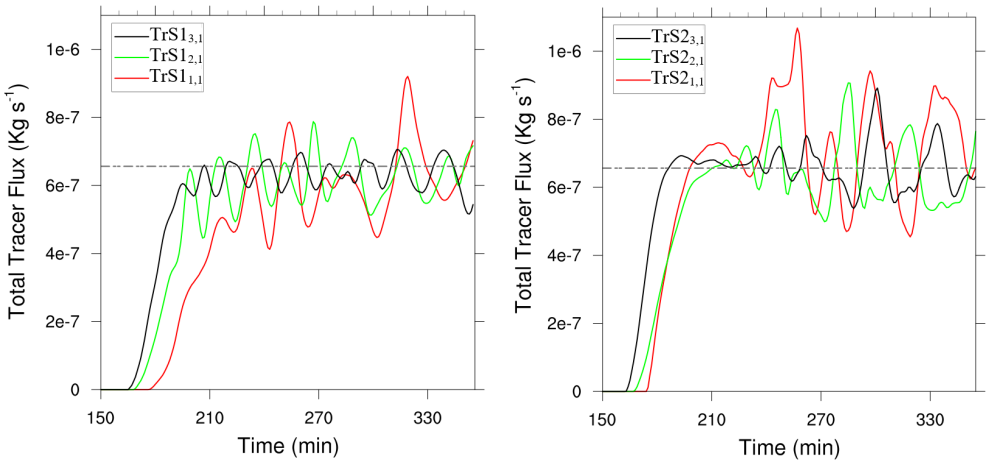

Fig. 3.12 *a) Time series of the total tracer flux ($TrS1_{1,1}$,$TrS1_{2,1}$ and $TrS1_{3,1}$) through the cross sectional area of the valley Σ located at 2 km from the centre of a tracer emission zone for S1. b) Same as a) for S2. The area Σ extends vertically from the valley bottom to the top of the cold-air pool z_{CAP}. The horizontal dashed line indicates the value of the emission rate Q over a given zone.*

The fact that the same quasi-steady value is reached for S1 and S2 can be easily explained by considering the equation for the tracer concentration,

$$\frac{\partial C}{\partial t} + \mathbf{u}.\nabla C = \nabla.(\kappa \nabla C) + q, \tag{3.5}$$

where C is the tracer concentration, $\mathbf{u} = (u, v, w)$ is the velocity field and κ is the turbulent diffusivity of the tracer (equal to the thermal diffusivity given by the model of Deardorff, 1980); q is the local emission rate, whose surface integral over a zone Z_i, whatever i, is equal to Q. Assuming that a steady state has been reached, that the flow is incompressible and ignoring diffusive effects yields the simplified equation,

$$\nabla.(\mathbf{u}C) = q. \tag{3.6}$$

We consider the small volume dV delimited by the slopes of the valley along the x-direction, by Σ-sections located at positions y and $y+dy$ inside the valley but outside an emission zone and by the valley floor and the cold-air-pool height along the vertical. Integrating over dV and using the divergence theorem yields

$$\int_{\Sigma} vC\,dx\,dz = \text{constant}, \tag{3.7}$$

since there is no tracer at the top of the cold-air pool and no emission inside dV. The constant value is the total emission rate over a zone Z_i, equal to Q,

$$\int_{\Sigma} vC dx\,dz = Q, \tag{3.8}$$

which simply expresses the conservation of the tracer emitted at the valley floor. As shown in Fig. 3.12, the total flux over Σ is the same for S1 and S2 since the emission rate is the same (but the areas Σ are different). Figure 3.12 also shows that the tracer flux displays marked oscillations, which are discussed below.

It is useful at this stage to express Eq. 3.8 in terms of the mean values of C and v over the area Σ. Denoting the average value over Σ by $<>_{\Sigma}$, the integral $\int_{\Sigma} vC dx\,dz$ is equal to $\Sigma < vC >_{\Sigma}$. Assuming that the fluctuations of v and C are much smaller than their average values, $< vC >_{\Sigma}$ can be written as $< v >_{\Sigma} < C >_{\Sigma}$. This assumption is actually approximately satisfied owing to the jet shape of the down-valley flow speed: the ratio $\beta = < vC >_{\Sigma} / < v >_{\Sigma} < C >_{\Sigma}$ ranges from $\beta \approx 2$ for $y = 3$ km to $\beta \approx 1.3$ for $y = 9$ km. Equation 3.8 thus becomes:

$$< C >_{\Sigma} = \frac{Q}{\beta\,\Sigma < v >_{\Sigma}}, \tag{3.9}$$

$< C >_{\Sigma}$ and $< v >_{\Sigma}$ being a function of y.

Since the tracer remains trapped in the bottom layer identified in section 3.3.3 for S1 and in section 3.3.5 for S2, the integral of C over Σ is actually equal to the integral of C over the area, denoted $\mathscr{A}$, defined by this bottom layer along the vertical and by the valley cross-section in the horizontal. The identity $\mathscr{A} < C >_{\mathscr{A}} = \Sigma < C >_{\Sigma}$ implies that Eq. 3.9 can also be written as:

$$< C >_{\mathscr{A}} = \frac{Q}{\beta\,\mathscr{A} < v >_{\Sigma}}. \tag{3.10}$$

Equation 3.9 (or equivalently Eq. 3.10) recovers a well-known result for so-called "trapped plumes" in a stably-stratified fluid (see Beychok, 2005, chp 8). Equation 3.9 also qualitatively accounts for the behaviour of the tracer concentration in Fig. 3.11: since the down-valley

flow speed increases with y, the concentration should decrease towards the valley exit, which is indeed what is observed. A more precise prediction of the tracer concentration is derived in section 3.4.4 below.

3.4.3 Temporal Evolution of the Tracer Concentration

The temporal evolution of the tracer flux integrated over the area Σ displayed in Fig. 3.12 shows marked temporal oscillations induced by the internal gravity wave field identified in section 3.3.2. The tracer being advected by the down-valley flow, its concentration is expected to oscillate as well but it is useful to quantify the magnitude of these oscillations. For this purpose, the concentration of the tracers released at the ground level from the three zones Z_i, $1 \leq i \leq 3$, is displayed in Fig. 3.13 for S1 and S2, at a position $y_i = 2$ km from the centre of the Z_i emission zone. The concentration is averaged over the area $\mathscr{A}$ (or, equivalently, Σ).

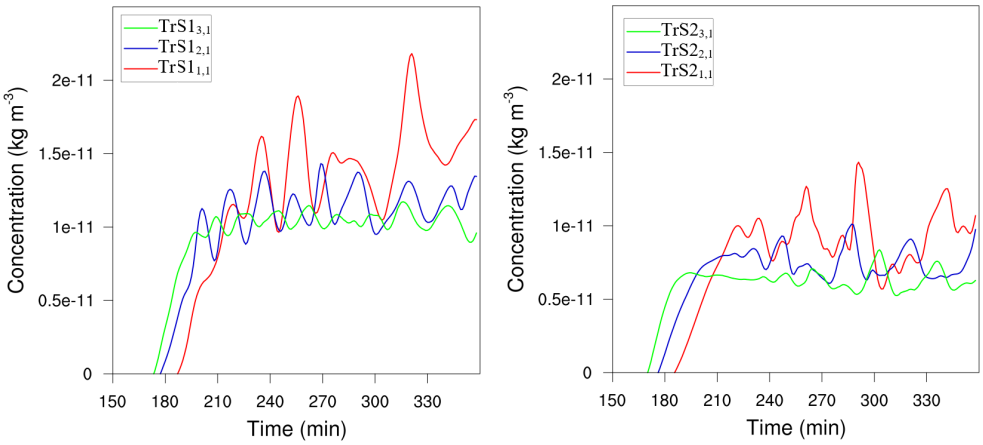

Fig. 3.13 *Time series of the tracer concentration averaged over the area $\mathscr{A}$ (defined in Section 4.2) for $TrS1_{1,1}$, $TrS1_{2,1}$ and $TrS1_{3,1}$. Each curve is plotted at two kilometres from the centre of the tracer emission zone. Emission starts at 150 min.*

Once the tracer emitted from a given zone Z_i has reached the counterpart y_i position, the concentration at that position reaches a quasi-steady value controlled by that of the down-valley flow speed at y_i. This value is higher close to the beginning of the valley and lower close to the valley exit, consistent with equation 3.10. The striking feature of Fig. 3.13 lies in the amplitude of the oscillations of the concentration. For the tracer emitted from zone Z_1 in S1 for instance ($TrS1_{1,1}$), the concentration may reach values as high as 50% of

the mean value. This effect is likely to occur in a real valley and should not be disregarded. From an operational point of view indeed, the pollutant concentration is usually averaged over one hour, possibly smoothing out those large fluctuations.

3.4.4 Evolution of the Tracer Concentration Along the Valley Axis

The tracer concentration averaged over the area $\mathscr{A}$ is plotted versus the along-valley direction y at $t = 300$ min in Fig. 3.14, for the tracers emitted at ground level in S1.

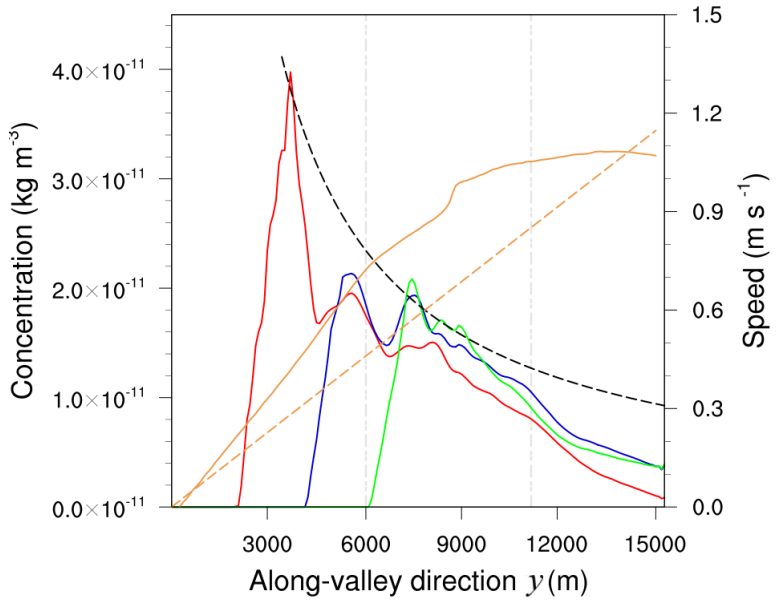

Fig. 3.14 *Tracer concentration averaged over the area $\mathscr{A}$ at t = 300 min versus the along-valley direction, for tracers emitted at the surface level in simulation S1 ($TrS1_{1,1}$, $TrS1_{2,1}$ and $TrS1_{3,1}$). The down-valley flow speed (V) averaged over the area Σ is also displayed at the same time (orange colour). The dashed lines are the theoretical predictions for V (orange dashed line, Eq. 3.13) and for the concentration (black dashed line, Eq. 3.15), respectively. The grey vertical lines represent the end of the plateau and of the valley.*

The figure displays two striking features. As regards the concentration field, a similar behaviour is observed whatever the emission zone, that is: the concentration increases with y inside the emission zone, at a rate that is inversely proportional to the local down-valley flow speed, and next decreases with the same law whatever the emission zone, leading to similar values of the $\mathscr{A}$-averaged concentrations emitted from the different zones. As for the down-valley flow speed, it displays a remarkable linear growth before saturating when reaching the plain.

This linear growth can be predicted by expressing the conservation of mass in the cold-air pool inside the valley, once the down-valley flow has developed.

We consider again the small volume dV, noticing that Σ depends upon y because of the decreasing height of the cold air pool inside the valley; more precisely Σ is constant in the plateau region ($0 \leq y \leq 6$ km) and decreases out of it ($6 \leq y \leq 11$ km). The mass fluxes across dV, whose sum vanishes by mass conservation, are those across the Σ-sections and across the top of the volume. In the following the density is assumed to be constant. The net flux across the Σ-sections is

$$(\Sigma < v >_\Sigma)(y+dy) - (\Sigma < v >_\Sigma)(y) \approx \frac{\partial(\Sigma < v >_\Sigma)}{\partial y} dy. \tag{3.11}$$

The flux across the top of the volume is mainly contributed by U_s (see Arduini et al., 2016). The projection of this flux along the vertical direction is thus equal to $-2\overline{U_s} h_n \sin\alpha_{\mathrm{CAP}}\, dy$, where $\overline{U_s}$ is the average of the downslope flow speed over the flow depth normal to the slope, h_n is the normal flow depth, and α_{CAP} is the slope angle of the topography at the top of the cold-air pool. Conservation of mass in volume dV therefore implies that

$$\frac{\partial(\Sigma < v >_\Sigma)}{\partial y} - 2\overline{U_s} h_n \sin\alpha_{\mathrm{CAP}} = 0. \tag{3.12}$$

Integration of this equation is simple only if $\overline{U_s}$, h_n and α_{CAP} do not depend upon y. This is approximately the case in the plateau region only. In this region, where Σ has a constant value, one gets a simple expression for the averaged down-valley flow speed, using the boundary condition $< v >_\Sigma = 0$ for $y = 0$:

$$< v >_\Sigma (y) = \frac{2\overline{U_s} h_n \sin\alpha_{\mathrm{CAP}}}{\Sigma} y. \tag{3.13}$$

Equation 3.13 thus predicts that, in the plateau region, the down-valley flow speed averaged over a valley section inside the cold-air pool evolves linearly with y; this is indeed what Fig. 3.14 shows.

Let us estimate the numerical value of the growth rate predicted by Eq. 3.13. The expression of the area Σ is

$$\Sigma = 2 z_{\mathrm{CAP}} \left(L_x + S_x^{\mathrm{CAP}}\right) - H\left(S_x^{\mathrm{CAP}} - \frac{S_x}{\pi} \sin\left(\pi \frac{S_x^{\mathrm{CAP}}}{S_x}\right)\right), \tag{3.14}$$

where the length scales L_x, H and S_x have been defined in section 3.2.2; S_x^{CAP} is defined such that $2\,(L_x + S_x^{\mathrm{CAP}})$ is the horizontal extent of the cold-air pool upper surface; from the expression of the topography (Eq. 3.2), $S_x^{\mathrm{CAP}} = (S_x/\pi)\,\mathrm{acos}(1 - 2\,z_{\mathrm{CAP}}/H)$. With $\overline{U_s} \approx 2.5$ m s^{-1}, $h_n \approx 90$ m, $\alpha = 16.7°$, $L_x = 720$ m (using values from Arduini et al., 2016)) and $z_{\mathrm{CAP}} \approx 400$ m (from section 3.3.3), the growth rate of $< v >_\Sigma$ is equal to 7.86×10^{-5} s^{-1}. This value is of the same order as that inferred from Fig. 3.14, equal to $\approx 1.2 \times 10^{-4}$ s^{-1} (the ratio of these two values being 1.5).

Using Eqs. 3.10 and 3.13, we infer the expression for the tracer concentration emitted from a zone Z_i, valid inside the plateau region of the valley and out of Z_i,

$$< C >_{\mathscr{A}} (y) = \frac{\Sigma}{\mathscr{A}} \frac{Q}{\beta\,(2\overline{U_s}\,h_n \sin\alpha_{\mathrm{CAP}})} \frac{1}{y}, \tag{3.15}$$

with Σ defined by Eq. 3.14. This law is superposed on the evolution of the concentration in Fig. 3.14a. The area $\mathscr{A}$ is equal to $2\,L_x\,h_1$, where $h_1 \approx 20$ m is the height of the first layer. A value of the parameter $\beta = 2$ has been used, implying that the concentration emitted at zone Z_1 is modelled. The agreement can be considered as being quite good.

3.5 Summary and Conclusions

We have investigated and modelled the impact of a valley-wind system on the night time behaviour of a passive tracer released in an idealized Alpine-type valley. Persistent stable atmospheric conditions are assumed, as they occur in winter during an anticyclonic regime, sometimes leading to a dynamical decoupling between the valley-wind system and the synoptic meteorological fields. This decoupling is imposed here and the case of a simple valley opening on a plain is considered, as in Arduini et al. (2016).

The first part extends the analysis of the valley-wind system proposed in Arduini et al. (2016) when a steady state has been reached. We focus on the down-valley flow dynamics with its impact on tracer transport in mind. We show that the down-valley flow displays oscillations induced by internal gravity waves emitted by the downslope flow when reaching the valley floor (or its level of neutral buoyancy) via a hydraulic jump. The down-valley flow is however weakly turbulent, as it exhibits turbulence in two regions only: close to the valley floor, within a shallow layer (≈ 20 m) extending from the ground to the first maximum of this flow, which behaves like a jet; and at the top of the cold-air pool close to the valley

exit, where the flow accelerates because of the decreasing height of the cold-air pool. The down-valley flow is elsewhere laminar because of the stable stratification. When averaged horizontally over the valley floor and vertically over the height of the cold-air pool, an area denoted by Σ in the paper, the down-valley flow speed displays a remarkable linear profile inside the valley, which can be modelled analytically using mass conservation within the cold-air pool; this is Eq. 3.13.

Passive tracers are emitted at the beginning of the steady regime and display several striking features. Firstly, the tracer emitted at the ground remains trapped at all times inside the shallow layer extending up to the jet speed maximum. As a consequence, and because the flow is laminar elsewhere (except in the second region detected close to the valley exit), tracers emitted above that bottom layer at different altitudes are advected towards the valley exit but do not meet. Evidence of this vertical decoupling in a real valley under stable wintertime conditions is provided in Fig. 3.15. The height of the jet-speed maximum may also account in this real case for the height over which pollutants are trapped, a conjecture which would need to be tested.

Fig. 3.15 *View of the Grenoble valley during an anticyclonic regime on December 18, 2016. Vertically decoupled cloud layers attest of the strong stratification of the atmospheric boundary layer (photo by C. Staquet).*

Outside its emission zone, the passive tracer averaged over the trapping region close to the ground, an area denoted by $\mathscr{A}$, displays a decaying law along the valley axis. This law can be modelled from the conservation of the tracer flux in the down-valley direction and the linear behaviour of the down-valley flow speed; this is Eq. 3.15. The concentration thus decreases as $1/y$ at a given time, where y is the along-valley coordinate. As a consequence, the total concentration at the valley exit, where the various valley-floor emissions superpose, may not be larger than inside the valley close to an emission source.

At a given location inside the valley, the concentration averaged over the area $\mathscr{A}$ displays strong temporal oscillations, induced by the down-valley flow, which may reach 50% of the mean (over time) value of the concentration. If occurring in a real valley, this would imply that time-averaged values in an urbanized valley may disguise high instantaneous, and potentially harmful, values.

Even if several conclusions regarding tracer transport in a real valley can be proposed from the present work, the highly idealized configuration considered here requires that the impact of main topographical features on the transport of tracers be taken into account, such as a change in the valley width along the valley axis (as done by Arduini et al., 2017), a non flat valley floor or tributary valleys.

Acknowledgements

The PhD work of J. Quimbayo is supported by the Colombian Administrative Department of Science, Technology and Innovation (COLCIENCIAS). Numerical simulations were run on the French national HPC facilities at CINES.

Chapter 4

Impact of Along-Valley Orographic Variations on the Dispersion of Passive Tracers in a Stable Atmosphere

This chapter is a reproduction of Quimbayo-Duarte et al. (2019b)

Abstract

A numerical model is used to investigate the response of the transport of passive tracers to orographic variations along the axis of an idealized version of an Alpine valley during wintertime after the evening transition. The valley is composed of an upstream valley section, which opens in a narrower downstream valley section, which opens on a plain. Two configurations were considered, called P1 and P2 for which the ratio between the valley-floor widths of the upstream and downstream sections is 4 and 11.5, respectively. The change in the thermal structure of the atmosphere in the along valley direction and over the plain leads to a horizontal pressure gradient that drives the development of an along-valley flow. The along-valley flow can be up- or down-valley, depending on the differences in cooling within the different valley sections and over the plain, with an intensity and depth that are related to the geometrical properties of the valley. Zones prone to stagnation, recirculation and ventilation were identified using the methodology developed by Allwine and Whiteman (1994). The agreement between the zones identified as prone to stagnation and that of high

tracer concentration was good for both configurations (P1 and P2). The narrowing of the valley was found to reduce significantly ventilation in the downstream section. For P2, in six hours only 10% of the mass of tracers emitted in the upstream section is transported to the downstream section, while for the tracers emitted in the downstream section 90% of the tracer mass is ventilated out of the valley towards the plain. The mass of tracers exported out of the upstream valley section for P2 is 55% that for P1, which indicates that ventilation in the upstream valley section reduces significantly as the ratio between the valley-floor widths of the upstream and downstream sections increases.

4.1 Introduction

Under wintertime atmospheric conditions, urbanized mountainous areas are affected by air pollution episodes related to particulate matter (PM) due to emission of primary aerosols and precursor gases leading to secondary aerosols. PM emission resulting from wood combustion during winter in urbanised complex terrain, as in the French Alps (Jaffrezo et al., 2005), is a key factor for air quality issues. Emissions being given, PM concentration is controlled by meteorology. A stable atmosphere, as this occurs frequently in winter, prevents vertical turbulent mixing from occurring and may therefore lead to locally high PM concentration. This is the case in valleys as stable boundary layers are often related to persistent cold-air pools (PCAPs), which can last for days leading to the accumulation of air pollutants, thereby exceeding air quality standards (Silcox et al., 2012).

The terrain geometry strongly affects the formation of cold-air pools (CAPs) in complex terrain. In valleys colder and denser air flowing down the slopes tends to accumulate in the lower parts of the terrain. Air may remain stagnant there or may be ventilated away (Whiteman, 1990) depending, inter alia, on the geometry of the valley. The thermal structure of the atmosphere plays a crucial role in the characteristics of the intra-valley atmospheric dynamics, by creating an along-valley pressure gradient that pushes the flow out of the valley, or in absence of any temperature difference along the valley axis, by promoting stagnation of air.

The relationship between the development of wintertime CAPs in mountainous areas and severe air pollution episodes has been well documented in recent years. Whiteman et al. (2014) considered the critical wintertime meteorological factors that affect PM concentrations in Utah's urbanized Salt Lake Valley using a record of 40 years of data. The authors found

a strong positive correlation between the strength of PM air pollution episodes and valley heat deficit, which can be thought as a vertically-integrated measure of atmospheric stability. Largeron and Staquet (2016) considered the relationship between synoptic-scale meteorology and boundary-layer processes, and the occurrence of PM air pollution episodes during PCAPs in the Grenoble Valley in the French Alps during winter 2006-2007. The authors also found a strong positive correlation between the strength of temperature inversions and the strength of PM air pollution episodes, when the temperature inversion persists for multiple days. Chemel et al. (2016) examined the temporal variability of PM concentration in an urbanized section of the Arve River Valley in the French Alps and showed that it may be explained by the temporal variability of the valley heat deficit and PM emissions in the area.

The physical processes controlling ventilation of air pollution from urbanized valleys have received little attention in the past. Allwine and Whiteman (1988) examined the evolution of a pollutant plume from a valley at night, which is released into the regional-scale flows the following morning. The authors developed a simple parametrization of valley-scale pollutant transport for regional-scale models. Regmi et al. (2003) used a numerical model and observations of chemical tracers to study air pollution transport in the Kathmandu valley in central Nepal. The authors concluded that local flows suppressed vertical mixing, leading to high air pollution levels due to the decrease of daytime ventilation of air over the area. Maurizi et al. (2013) used results from numerical simulations to investigate the budget of pollutants in the Po Valley in the north of Italy, and concluded that the contribution to air pollution from emissions outside the hot spots cannot be neglected due to the vertical mixing and entrainment at the top of the boundary layer, being more effective than advection in the vertical in the budget of pollutants near the surface.

To date, operational weather and air-quality numerical models are run using relatively coarse grid spacings and so rely on parametrizations of sub-grid scales. There is a need for reliable sub-grid scale parametrizations that can represent topographically-induced transport processes (Rotach et al., 2014). High-resolution numerical simulations of idealized configurations are key to developing such parametrizations. Several works have considered the effects of geometrical properties of the valley, namely its width (Serafin and Zardi, 2010) and depth (Colette et al., 2003), on the thermal structure of the atmosphere and the development of the valley-wind system, using high resolution idealized numerical simulations. Wagner et al. (2015) used an idealized valley to investigate the effects of both valley width and depth on vertical transport processes. The authors found that near-surface air is transported to the free atmosphere more effectively over valleys than over flat terrain. The role of the valley wind system in the transport of pollutants has been also addressed in different idealized studies.

Lehner and Gohm (2010b) explored the role of thermal stratification and surface albedo on daytime pollution transport in an idealized steep valley. The results obtained are qualitatively consistent with wintertime observations in the Austrian Inn Valley. Quimbayo-Duarte et al. (2019a) quantified the impact of the valley-wind system on the transport of passive tracers in a stably-stratified atmosphere during wintertime in an isolated alpine valley opening directly on a plain. The authors showed that the variability of the tracer concentration field is dynamically controlled by that of the along-valley wind.

However, little attention has been paid to the impact of along-valley topographic variations on the valley-wind system. (Li and Atkinson, 1999) analysed a set of numerical simulations to examine the dynamical and thermal characteristics of the atmosphere of idealized valleys during the morning and evening transition periods. The authors showed that the evening transition always lasts longer than the morning transition, and that the time at which these periods start strongly depends on the orography. Using results from numerical simulations (Arduini et al., 2017) explored the impact of along-valley variations of the valley width on the nocturnal boundary-layer structure in idealized deep valleys. The authors found that the dynamical and thermodynamical characteristics of the valley atmosphere along a valley section are strongly affected by the valley width of the neighbouring sections.

The main objective of the present work is to investigate the impact of along-valley orographic variations on the transport and dispersion of passive tracers under wintertime stable and dynamically decoupled atmospheric conditions. Results of a set of high-resolution numerical simulations of an idealized system of valleys with a varying width along the valley axis are presented and analyzed. The same numerical setup as Arduini et al. (2017) is used with the inclusion of set of passive tracers in the present work.

The numerical simulations are presented in section 4.2. In section 4.3 a brief description of the main characteristics of the valley atmosphere is given. Section 4.4 characterizes the zones prone to stagnation and recirculation using the methodology devised by Allwine and Whiteman (1994). In section 4.5 the overall behaviour of the passive tracers is described. Finally, a brief summary and conclusions are given in section 4.6.

4.2 Methods

4.2.1 Numerical Model

In the present work the Weather Research and Forecasting (WRF) model (Skamarock et al., 2005), version 3.4.1, is used to perform the numerical simulations. The model was run in a large-eddy simulation (LES) mode, as in for instance Catalano and Cenedese (2010), Wagner et al. (2014) and Burns and Chemel (2015). The model uses an Arakawa grid of type C and a terrain following coordinate system based on the dry-hydrostatic pressure. The 1.5-order turbulent kinetic energy (TKE) closure of Deardorff (1980) is used to model subgrid-scale mixing, but was modified following Scotti et al. (1993) to account for the strong anisotropy of the grid along the slopes in the first vertical levels. The simulations use the same topography and initial conditions for the temperature and velocity fields as Arduini et al. (2017). A brief description of the configuration of the simulations is presented below.

4.2.2 Topography

The topography used is a set of U-shaped system of valleys. Each valley system is composed of an upstream valley section ($\mathscr{U}$) (extending from 0 to 10 km in the y-direction) and a downstream valley section ($\mathscr{D}$) (extending from 13 to 19 km in the y-direction) joined by a 3-km long junction ($\mathscr{J}$). The downstream valley opens on a plain ($\mathscr{P}$). The difference between $\mathscr{U}$ and $\mathscr{D}$ lies in the width of the valley floor, which is larger in the upstream section than in the downstream section (see Fig. 4.1).

The system of valleys has an extension of 18 km in the cross-valley direction, and is symmetric about the valley axis (x=0). The topography is also symmetric about the y=0 plane for numerical tractability, but only the southern part of the domain (0 to 27 km) is considered for the analysis (see Fig. 3.1). The slopes in both $\mathscr{U}$ and $\mathscr{D}$ share the same length along the x-direction (4230 m). At the top of each slope there is a plateau long enough to prevent boundary related issues. The valley floor is set at 1000 m above the sea level, and the maximum elevation of the terrain (plateau) is set to 800 m above ground level. A detailed description of the terrain is reported in Arduini et al. (2017).

In the present work two different configurations are studied: a first configuration using an upstream-valley floor width $\mathscr{L}_u = 1440$ m, referred to as the pooling case $P1$, and a second

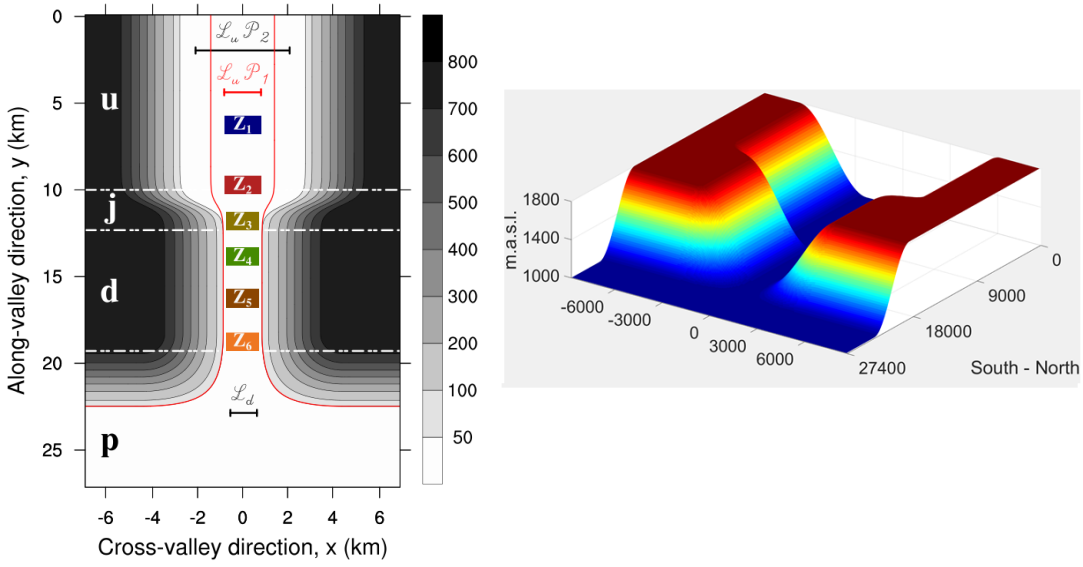

(a) (b)

Fig. 4.1 *a) Contours of the terrain height in metres from the valley bottom for configuration P2 (the first contour is set at 50 m for configuration P1 is indicated with a red line). The topography is oriented north-south in the y-direction, the valley being symmetric along that axis. The system of valleys is divided in three sections, an upstream section ($\mathscr{U}$), a downstream section ($\mathscr{D}$), a junction ($\mathscr{J}$) between upstream and downstream sections, and finally a plain ($\mathscr{P}$) at the end of the valley. Six different emission zones are set along the valley axis. b) Three dimensional representation of topography P2. Frames (a) and (b) display the southern part of the domain.*

configuration using $\mathscr{L}_u = 4140$ m, referred to as the pooling case $P2$. For both $P1$ and $P2$ the downstream valley width ($\mathscr{L}_d$) is set to 360 m so that the constriction ratio between the upstream and downstream sections is equal to 4 for $P1$ and 11.5 for $P2$. All other geometrical parameters between $P1$ and $P2$ are otherwise the same (see Fig. 4.1).

4.2.3 Numerical Setup

Numerical simulations using either $P1$ or $P2$ were run using two nested domains, with horizontal resolution 270 m, for the outer domain, and 90 m for the inner domain. In the along- and cross-valley directions, the outer domain extends far enough so that the boundaries do not have any effect on the results inside the valley over the duration of the simulations. Outputs from the outer domain were used to provide the boundary conditions for the inner domain, with no feedback from the inner to the outer domain. Along the vertical, the domain top was set to 12000 *m* above sea level and the vertical resolution was defined to decrease

with height, with the first mass point located 1.7 m above the ground and 25 grid points in the first 100 m above the ground.

A stable atmosphere with a constant positive vertical gradient of (virtual) potential temperature of 1.5 K km^{-1} associated with a buoyancy frequency $N = 0.00715$ s^{-1} was set at initial time. No wind was prescribed at the initial time. Both $P1$ and $P2$ started one hour and a half before sunset (15h30 local time) on a winter day (21 December) and lasted for 6 hours. Therefore, the atmosphere of a winter night under dynamically decoupled conditions with no synoptic flow was considered.

The surface physics was represented using the revised MM5 Monin-Obukhov surface layer scheme Jiménez et al. (2012). The Rapid Radiative Transfer Model (Mlawer et al., 1997) and the scheme proposed by Dudhia (1989) were used to model radiative transfer for long-wave and short-wave radiation, respectively. The surface cover in this simulation was set to "grassland" and the skin temperature was initialized from an extrapolation of the temperature of the first three layers above the surface.

4.2.4 Passive Tracer Emission

A set of passive tracers was released from six different emission zones along the valley axis (see Fig. 4.1a). The tracers have the same physical properties as that of the air and deposition was neglected. The same amount of tracers was released continuously from the initial time for each zone during the simulation using a constant rate equal to $Q = 2.25\ 10^{-6}\ kg\ s^{-1}$. A constant background concentration equal to $1.25\ 10^{-12}\ kg\ m^{-3}$ was set in the whole domain for each tracer.

The following notation will be used to identify the six different tracers emitted in each of the simulations: $TrPn_i$, where Pn refers to the simulations ($P1$ or $P2$) and i, to the emission zone along the valley axis ($1 \leq i \leq 6$). For example, the tracer emitted in the fourth emission zone (green zone in Fig. 4.1a) in simulation $P2$, will be denoted by $TrP2_4$.

4.3 Low Atmosphere Structure

4.3.1 Along-Valley Flow

In a typical winter day, after the evening transition an along-valley flow develops in the down-valley direction due to the pressure gradient generated by the difference in cooling of the lower part of the atmosphere within the valley and over the plain (Zardi and Whiteman, 2013). The temporal evolution of the vertical structure of the along-valley flow is displayed in Fig. 4.2 at the end of the upstream section ($\mathscr{U}$), and at the centre of the downstream section ($\mathscr{D}$) for $P1$ and $P2$.

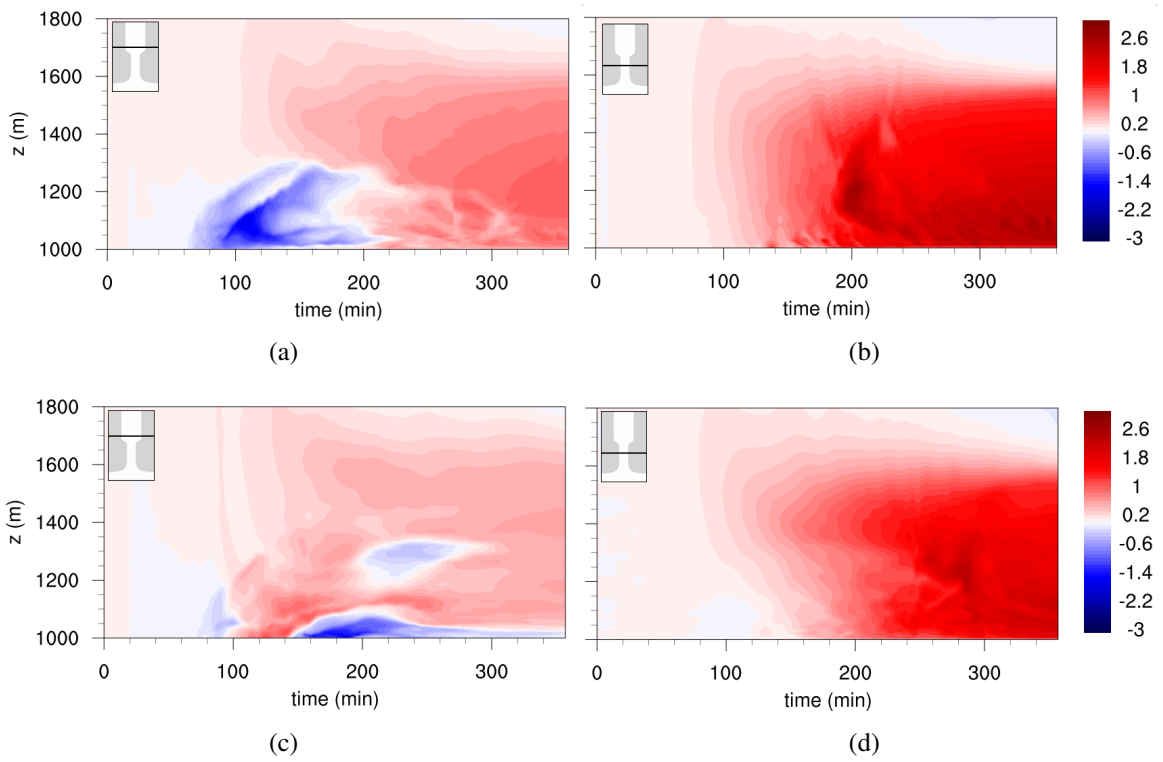

Fig. 4.2 *Hovmöller diagram of the evolution of the along-valley wind speed at the valley centre for P1 at 10 km (a) and 16 km (b), and for P2 at 10 km (c) and 16 km (d) from the beginning of the valley. Positive (red) values correspond to a down-valley flow, negative values (blue) to an up-valley flow.*

For $P1$, at the end of section $\mathscr{U}$ from 60 to 200 minutes into the simulation (see Fig. 4.2a), an up-valley wind is present in the first hundred meters above the ground. Although in $P2$ the flow behaviour seems to be rather complex (Fig. 4.2c), a clear up-valley flow is identified as well. The up-valley flow is deeper in $P1$ (about 250-m deep at 180 minutes)

compared to $P2$ (100-m deep at 180 minutes), but the shallower up-valley flow in $P2$ has a greater speed and lasts longer (until the end of the simulated period). To estimate the relative impact on mass flux of either up-valley or down-valley flow, the cumulative (in the vertical direction) mass flux at $y = 10$ km is displayed in Fig. 4.3 for $P1$ and $P2$ at two different times (100 and 200 minutes). This cumulative mass flux represents the amount of mass transported at a given position y in the along-valley direction from the ground up to a given height above ground level. Figure 4.3 shows that at 100 minutes the shallower flow in $P2$ (solid red line in Fig. 4.3) transports more mass in the up-valley direction than the deeper flow in $P1$ (solid blue line in Fig. 4.3). By contrast, at 200 minutes (dashed lines in Fig. 4.3), when the flow is well developed in the down-valley direction, the amount of mass exported from $\mathscr{U}$ below the height of the plateaux is larger in $P1$ than in $P2$ by more than 30%.

In the downstream valley section $\mathscr{D}$, no up-valley wind is observed in $P1$ or $P2$ (see Figs. 4.2b and 4.2d), but differences in the vertical structure of the flow for each simulation can be noted. For $P1$ after 150 minutes the speed of the flow reaches about 1.5 m s^{-1} and appears to be vertically quasi-homogeneous up to 600 m above ground level. It reaches a quasi-steady state around 200 minutes when the along-valley flow in the upstream section $\mathscr{U}$ reverses from up-valley to down-valley (see Fig. 4.2a). The development of the down-valley flow close to the ground takes longer in $P2$ (200 min, see Fig. 4.2d) and its speed reaches about 1.5 m s^{-1} only at 250 min. The development of the down-valley flow in $P2$ is not as vertically homogeneous as in $P1$ because it is delayed near the surface by the up-valley flow found at $\mathscr{D}$ (see Fig. 4.2c). The particular behaviour of the along-valley flow at these positions is well explained by the differences in the thermal structure of the atmosphere along the valley system, presented in the next section.

4.3.2 Thermal Structure

Figure 4.4 shows the change in potential temperature ($\Delta\theta$) between the initial time and 90 minutes into the simulation averaged over two different 1-km-long sections of the valley. The left and right panels in figures 4.4a and 4.4b display $\Delta\theta$ for the section centered at the exit of $\mathscr{U}$ (10 km) and for the section centered half way along $\mathscr{D}$ (16 km) for $P1$ and $P2$, respectively. Horizontal white lines indicate the top height of the CAP (denoted by CAP_{top}), defined as in Burns and Chemel (2015) by the local minimum of the vertical gradient of potential temperature above the ground-based inversion layer, averaged over the valley floor.

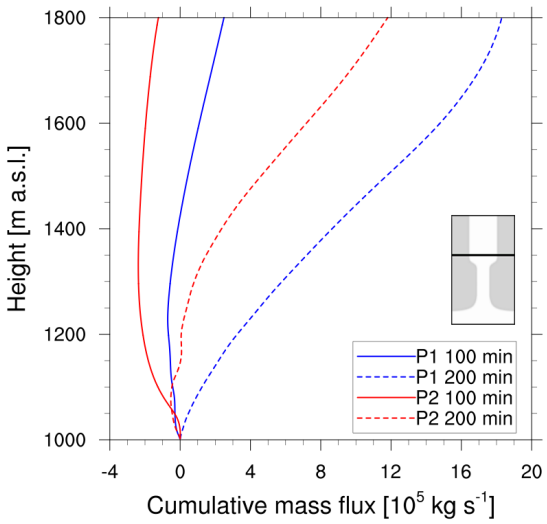

Fig. 4.3 *Cumulative mass flux across a vertical surface perpendicular to the valley axis located at 10 km from the beginning of the valley for P1 (blue lines) and P2 (red lines) at 100 (solid lines) and 200 minutes (dashed lines) of simulation.*

The CAP is shallower in $\mathscr{U}$ than in $\mathscr{D}$ for both $P1$ and $P2$, the difference in CAP heights between the two valley sections being more pronounced for $P2$ than for $P1$. These differences are explained by the differences in the valley volume of each section. Since the length of the slopes are the same in $\mathscr{U}$ and $\mathscr{D}$ for both $P1$ and $P2$, the mass flux from the slopes to the valley centre is almost equal for any position along the valley (not shown). Thence, the smaller volume of $\mathscr{D}$ is filled with cold air from the slopes more rapidly than the larger volume of $\mathscr{U}$. As a result, the rate of growth of the CAP is greater in $\mathscr{D}$ than in $\mathscr{U}$ (see Fig. 4.4).

As $P1$ and $P2$ share the same thermal vertical profile at the initial time, the development of the cooling rate along the valley axis is strongly affected by such differences in the thermal structure between each valley section. Differences in the cooling rate along the valley (see Fig. 4.5) indicate the existence of differences in temperature along the system, which derives in the pressure gradient driving the generation of the along-valley flow. At 60 min, the cooling rate in $\mathscr{U}$ is lower in $P2$ than in $P1$ since the same amount of cold air is filling a larger valley-volume as illustrated by the shallower CAP in $P2$. By contrast, in $\mathscr{D}$ the average cooling rate is similar for $P1$ and $P2$, as expected since the valley-volume is the same. However, the region near $\mathscr{J}$ (between 13 and 16 km along y) in $P1$ cools relatively faster because of the greater export of near-surface cold air from $\mathscr{D}$ to $\mathscr{U}$. At 300 minutes the flow is in a quasi-steady state for both $P1$ and $P2$, reducing significantly the differences in the thermal structure along the system of valleys due to the variations of the valley width

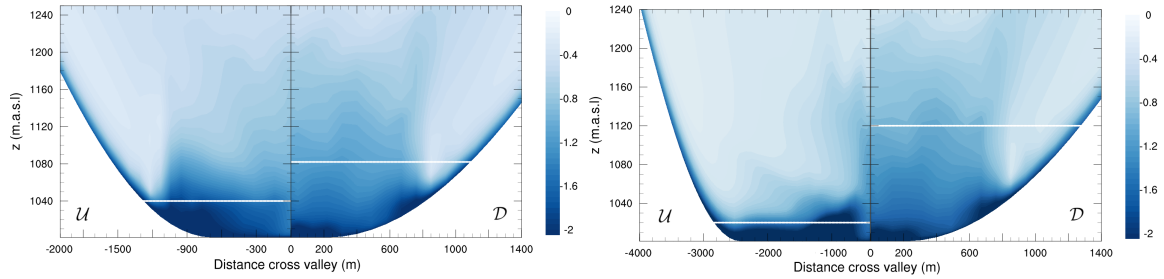

Fig. 4.4 *Vertical cross sections of the change in the potential temperature ($\Delta\theta$) with respect to the initial condition averaged over 1 km along the y-direction after 90 minutes into the simulation for P1 a), and P2 b). Each frame is divided in two panels, the left panel corresponding to the exit of the upstream valley $\mathscr{U}$ (10 km) and the right panel corresponding to the mid part of the downstream valley $\mathscr{D}$ (16 km). White lines represent an estimate of the CAP height at each section and setup.*

(Arduini et al., 2017). As a result, the cooling rate along the valley axis is more homogeneous inside the valley and the driving pressure gradient at this time is the one between the valley core and the plain, driving the along-valley flow out fromthe system as a whole.

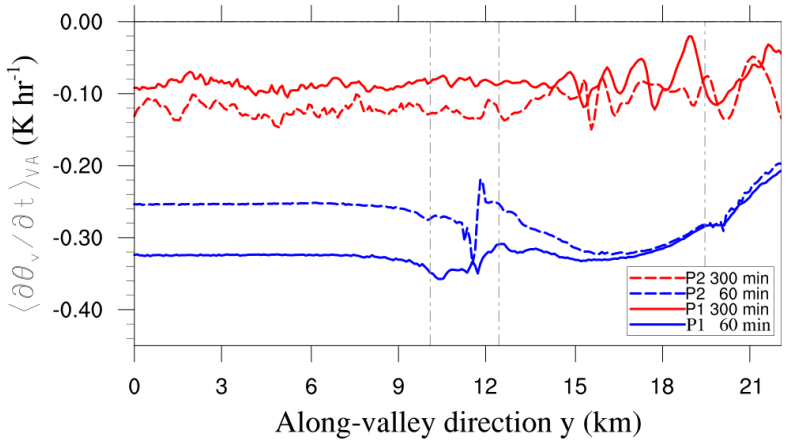

Fig. 4.5 *Average of the cooling rate over a cross-section extending up to the plateaux height ($\langle \partial\theta_v/\partial t \rangle_{VA}$) at the end of the first hour (blue line) and at the end of fourth hour (red line) of simulation for P1 (solid lines) and P2 (dashed lines). Vertical grey dashed lines stand for the end of each section of the valley.*

4.4 Stagnation and Ventilation Zones

Since the purpose of the present work is to analyse the transport of passive tracers by the wind, the locations of stagnation and ventilation zones at the valley bottom induced by this wind are identified first.

4.4.1 Summary of the Methodology Proposed by Allwine & Whiteman (1994)

The methodology proposed by Allwine and Whiteman (1994) aims at characterizing the recirculation, stagnation and ventilation zones from records of the horizontal velocity components u and v at a fixed location (say at a fixed mast) and at fixed time intervals. The wind speed and wind direction are then computed and averaged in time. In the present case, the wind speed and wind direction are spatial fields and are also averaged over the first 30 m above the ground. These averaged fields are denoted by U_i and D_i, respectively, the index i varying between 1 and τ/T, with T is the averaging window and τ is the length of the records (assumed to be a multiple of T). τ was set to the simulated period (that is six hours) and T was set to 15 min.

Allwine and Whiteman (1994) defined two main quantities to characterize the stagnation and ventilation zones induced by the velocity field, namely:

- the wind run time series S_i, where S_i is the virtual distance that an air parcel would travel during the averaging time period T, assuming the air parcel does not experience any change in speed or direction during this time period, that is $S_i = T\,U_i$. The effective distance travelled by the fluid particle over the duration τ is denoted by L (see Fig. 4.6).
- the recirculation index R defined by:

$$R = 1 - \frac{L}{S}. \tag{4.1}$$

  R quantifies the recirculation character of the flow: when R tends to 1, an air parcel following the flow may have travelled some distance, but its final position remains close to the initial position, meaning that it has experienced recirculation. Conversely, if R tends to 0, an air parcel is continuously moving away from its initial position; i.e. it has experienced ventilation.

Note that, in the present case, $S = \sum_{i=1}^{n} S_i$ and R are (time independent) spatial fields.

In order to classify the local transport properties of the velocity field, critical values for S and R (denoted by S_c, S_{cv}, R_c and R_{cv}) are defined such that:

- if $S \leq S_c$ in a given zone, this zone is defined as a stagnation zone;
- if $R \geq R_c$ in a given zone, this zone is defined as a recirculation zone.
- if $R \leq R_{cv}$ and $S \geq S_{cv}$ in a given zone, this zone is defined as a ventilation zone.

To better track the zones prone to high tracer concentration (Largeron, 2010), the following additional class is added:

- if $R \geq R_c$ and $S \leq S_c$, this zone is defined as a critical stagnation zone.

Following Allwine and Whiteman (1994), R_c and R_{cv} were set to 0.6 and 0.2, respectively. Values for S_c and S_{cv} depend on the time interval τ, the wind speed and the orography, among other factors. In the present case, S_c was set to 12 km, which represents 25% of the maximum value of S computed from the results of the simulations (see figs. 4.7c and 4.7d) and S_{cv} was set to 24 km.

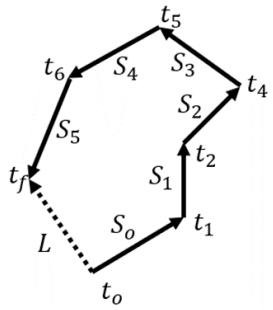

Fig. 4.6 *Sketch of the definitions of the wind run (S_i) and of the transport distance (L). Each segment S_i is computed using an average over the time interval T equal to 15 minutes in the present work. Adapted from Allwine and Whiteman (1994).*

4.4.2 Recirculation, Stagnation and Ventilation Zones

The differences in the wind structure in the lower part of the atmosphere between the configurations $P1$ and $P2$ may be assessed by tracking the zones prone to recirculation, stagnation or ventilation.

As regards the recirculation zones, results show that for $P1$ there is a single recirculation zone at the exit of $\mathscr{U}$ (see Fig. 4.7a). For $P2$ several recirculation zones are identified (see Fig. 4.7b), the larger one being located near the valley slopes in $\mathscr{U}$. Other zones with a recirculation character are found in the junction $\mathscr{J}$, which may play an important role in blocking the transport out of $\mathscr{U}$.

Conversely, for the wind run S, the values and distribution over the domain are very similar in $P1$ and $P2$ (see Figs. 4.7c and 4.7d). S reaches a maximum value of about 48 km at the exit of $\mathscr{D}$ and a minimum value close to 4 km in the core of $\mathscr{U}$. Stagnation zones are found in $\mathscr{U}$ and $\mathscr{J}$ only (ignoring the plateaux region for $P2$).

Using the threshold values discussed in the previous subsection the zones prone to critical stagnation and ventilation for each configuration are displayed in Fig. 4.7e and Fig. 4.7f. Note that the recirculation zones are always detected in the stagnation zones (values of S less than 12 km), implying that the recirculation zones displayed in figures 4.7a and 4.7b for $P1$ and $P2$ are also critical stagnation zones prone to high tracer concentration. By contrast, the slopes and the exit of the valley system, where a jet is detected, are ventilation zones. No ventilation zone is found in the valley core, which suggests that for tracers emitted close to the ground the whole system behaves as a trapper. This is particularly true for $P2$, where the largest recirculation zones are detected.

For $P1$, the single recirculation zone detected corresponds to the position where the flow coming from the slope at the junction diverges between the $\mathscr{U}$ and $\mathscr{D}$ valley sections during the first 200 minutes of the simulated period. Due to the greater change in the cross-sectional area between $\mathscr{U}$ and $\mathscr{D}$ for $P2$, the flow dynamics are more complex than for $P1$ and a more detailed inspection is required.

Figure 4.8 displays a zoom on the zone where the recirculation zones for $P2$ are detected and shows streamlines averaged in time for three different time periods and over the first 30 m above the ground. Between 60 and 120 minutes after the initial time (see Fig. 4.8a), the air coming from the slopes converges at the centre of the valley floor and flows in the up-valley direction, creating counter-rotating eddies near the end of $\mathscr{U}$ and a recirculation zone close

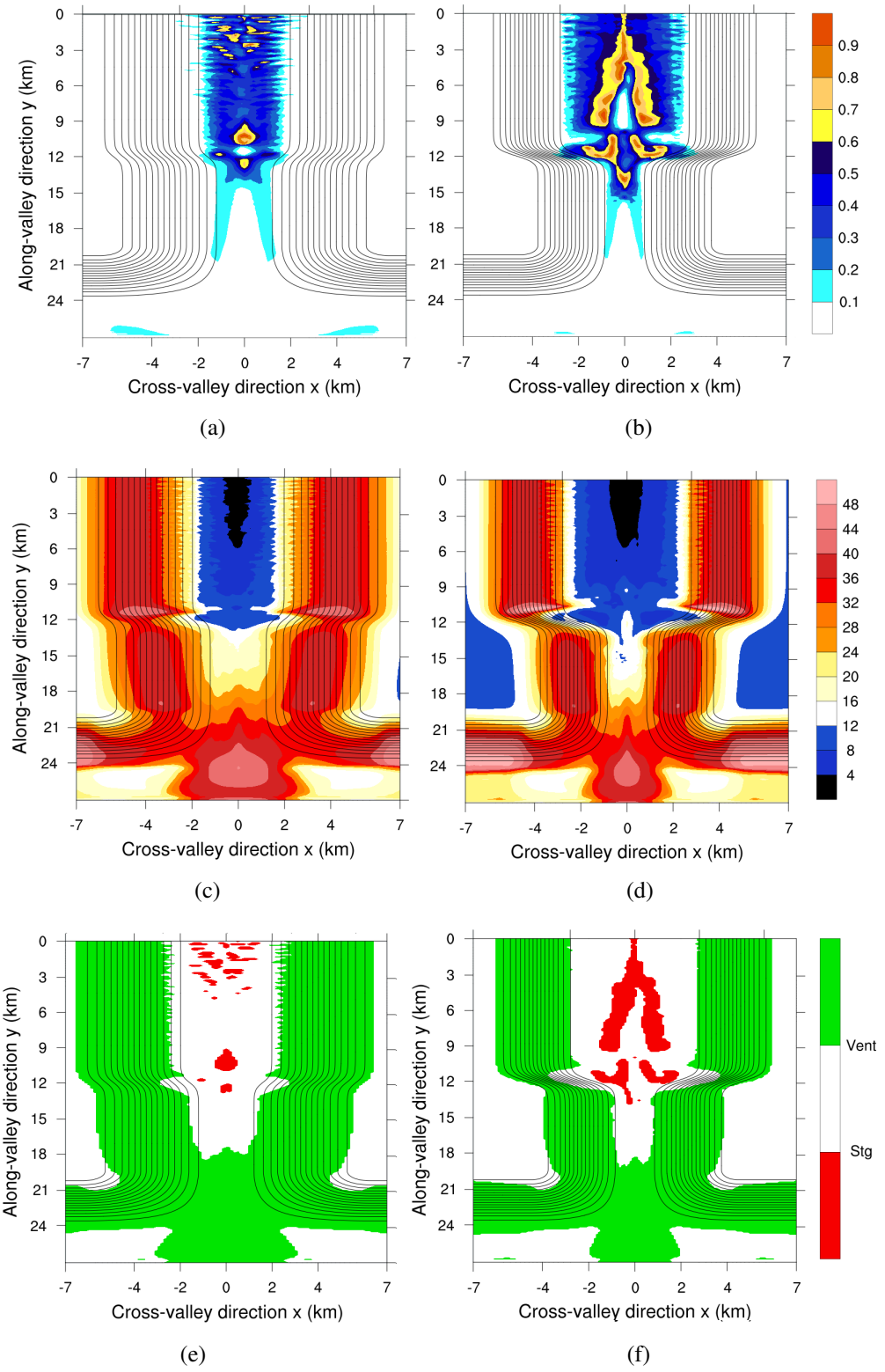

Fig. 4.7 *Contour plots of the recirculation factor (R, top row), contour plots of the wind run (S, middle row) and zones prone to critical stagnation and ventilation (bottom row) for P_1 (a, c and e) and P_2 (b, d and f) configurations. Each point in the domain has been averaged over 15 minutes and over the first 30 m above the ground level. The unit for S is km.*

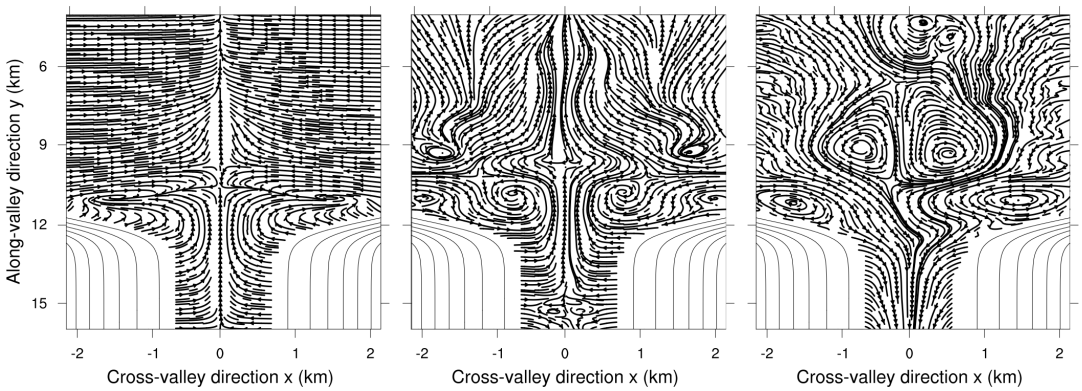

(a) (b) (c)

Fig. 4.8 *Zoom on the upper part of the valley for P2 displaying streamlines. The velocity field is vertically averaged over the first 30 m above the ground and averaged in time over a) 60-120 min, b) 120-180 minutes and c) 240-300 minutes.*

to the junction. The divergence of the along-valley flow near the end of $\mathscr{U}$ also favours the creation of such a recirculation zone.

Such recirculation is also visible between 120 and 180 minutes (see Fig. 4.8b) while an up-valley flow is established throughout $\mathscr{U}$. At the beginning of $\mathscr{D}$ the flow does start to flow down-valley (close to $y = 15$ km), which contributes to the creation of the most southern recirculation zone. Between 240 and 300 minutes the well developed up-valley flow push the stagnant air up-valley into $\mathscr{U}$ (see Fig. 4.8c). The stagnant air, advected towards the beginning of the valley by the up-valley flow, recirculates at the bottom of the slopes towards the centre of the valley floor (flowing down-valley). This creates a quadrupole flow structure at the valley floor with a stagnation zone at the very centre of $\mathscr{U}$.

4.5 Transport of Passive Tracers

4.5.1 Horizontal Distribution of Tracers in the Lower Atmosphere

Figure 4.9 shows contour plots at the end of the simulated period of the concentration of tracers emitted at two different locations for both $P1$ and $P2$. The blue lines indicate the regions where critical stagnation are identified. Note that the colour scale for each figure is different to highlight the peaks in concentration for each tracer. Tracer $TrP1_1$ (see Fig. 4.9a) spreads throughout the valley floor, however, a small fraction of the mass of the tracer

(compared to the mass of tracer remaining in $\mathscr{U}$) is transported from $\mathscr{U}$ to $\mathscr{D}$. The agreement between the location of maximum tracer concentration and that of critical stagnation zones is good at about 10 km from the beginning of the valley.

Tracer $TrP1_3$ (see Fig. 4.9b), emitted further down valley, displays higher concentrations than $TrP1_1$ at the end of the simulated period. Its emission zone is located at the exit of $\mathscr{U}$ (near a ventilation zone), but it coincides with the location of a recirculation zone. The proximity of the emission zone and the recirculation zone creates a localized region of high concentration at about 12 km, which afterwards is ventilated down valley.

The dynamics for $P2$ is, in general, more complex than for $P1$ and so is the evolution of the tracers. Figure 4.9c show that there is no transport of tracer $TrP2_1$ in the down-valley direction because of the up-valley flow in the region where it is emitted. The tracer is transported in the up-valley direction and diverges towards the slopes as it encounters more stagnant air further upstream before mention. There is a good agreement between the zones of high tracer concentration and the critical stagnation zones (blue lines in Fig. 4.9c). Tracer $TrP2_3$ (see Fig. 4.9d) is emitted at the exit of $\mathscr{U}$ between stagnation zones and so it remains trapped close to its emission zone. Note that even though it is released in a local non-stagnant zone, it remains confined near the emission zone because it is surrounded by stagnant air. The latter suggests that relationship between zones of high concentration of tracers and areas marked as prone to stagnation should be considered with caution, the variability in the concentration of air pollutants is not only a function of atmospheric dynamics; location and emission rates also play an important role in the problem.

4.5.2 Ventilation Efficiency

To quantify the effect of $\mathscr{D}$ section on the ventilation of the tracers emitted in $\mathscr{U}$ section (presented briefly in the previous section), the mass of each tracer within the volumes of $\mathscr{U}$, $\mathscr{D}$, $\mathscr{J}$ and $\mathscr{P}$, relative to its mass emitted from the initial time to time t, denoted by R_M, was analysed. R_M is defined by:

$$R_M = \frac{\int_{V_i} C \cdot dV}{Q \cdot t}, \tag{4.2}$$

where C is the tracer concentration in $kg\ m^{-3}$, $V_i = \mathscr{U}, \mathscr{D}, \mathscr{J}, \mathscr{P}$ and Q is the constant tracer emission rate. The top surface of each volume V_i is set by the height of the plateaux (that is 1800 m a.s.l.).

$TrP1_1$ is confined within $V_{\mathscr{U}}$ for the first four hours because the emission zone is located on a stagnation zone (see Fig. 4.10a). This also applies to the other tracer emitted in $V_{\mathscr{U}}$. As soon as the down-valley flow is fully developed in $\mathscr{U}$ (at about 240 minutes) R_M starts to decrease steadily. At 300 minutes the mass within $V_{\mathscr{U}}$ has already decreased at about 55% of the mass emitted. The tracer is transported along the system of valleys and reaches the plain by the very end of the simulated period (i.e. within two hours).

For $TrP2_1$ (see Fig. 4.10e) the effect of stagnation is greatly amplified, as was shown in the previous section. The tracer is transported to $\mathscr{J}$ after 300 min, and its mass within $V_{\mathscr{U}}$ decreases by just around a 10% by the end of the simulated period (i.e. within one hour). This result suggests that the narrow constriction strongly affects the ventilation of the tracers from this section. The mass of tracer transported out of $\mathscr{U}$ is reduced by about 60% between $P1$ and $P2$ by the end of the simulated period.

The behaviour of $TrP1_3$ emitted at the junction between the two valley sections (see Fig. 4.10b) is not very different to that of $TrP1_1$. The mass of tracer within $V_{\mathscr{J}}$ appears to remain constant until two hours of simulation. From this time, the tracer starts to flow downstream with some transport upstream for two more hours as a result of the divergence of the flow within the junction. After about 210 minutes from the beginning of the simulation the flow in the whole domain is completely down-valley (see Figs. 4.2a and 4.2b) driving the tracers out of the system of valleys, which is consistent with the linear decrease of R_M within $V_{\mathscr{D}}$ and a continued linear increase of R_M within $V_{\mathscr{P}}$ for the last two hours of simulation. The transport of $TrP2_3$ from $\mathscr{J}$ to $\mathscr{D}$ is delayed further (see Fig. 4.10f) because the up-valley flow in $V_{\mathscr{U}}$ persists for longer (see Sect. 4.3.1). By the end of the simulated period the mass of $TrP2_3$ within $V_{\mathscr{J}}$ is almost three times larger than what have left of $TrP1_3$ in $V_{\mathscr{J}}$.

Two tracers/emission zones are considered for the volume $V_{\mathscr{D}}$ to better characterize the zone. $TrPn_4$, emitted 14 km from the beginning of the valley, reaches first a neighbouring section after about 80 minutes. Initially a predominantly up-valley flow drives something close to the 30% of the total mass of tracer through $V_{\mathscr{J}}$. Afterwards a down-valley establishes quickly and transports the tracer out of the valley (which eventually reaches the plain after three hours of simulation). At the end of the simulated period about the 80% of the total mass of tracer emitted is out of the valley (that is in $V_{\mathscr{P}}$). Stagnation is amplified for $P2$ because the up-valley flow is stronger than for $P1$. The transport up valley is greater; an equivalent mass of about the 25% of the total mass emitted reaches $V_{\mathscr{U}}$ at the end of the first three hours of simulation. When the flow changes direction and tracers are transported in the down-valley direction, nonetheless the mass of tracer in $V_{\mathscr{U}}$ and $V_{\mathscr{J}}$ combined at the end

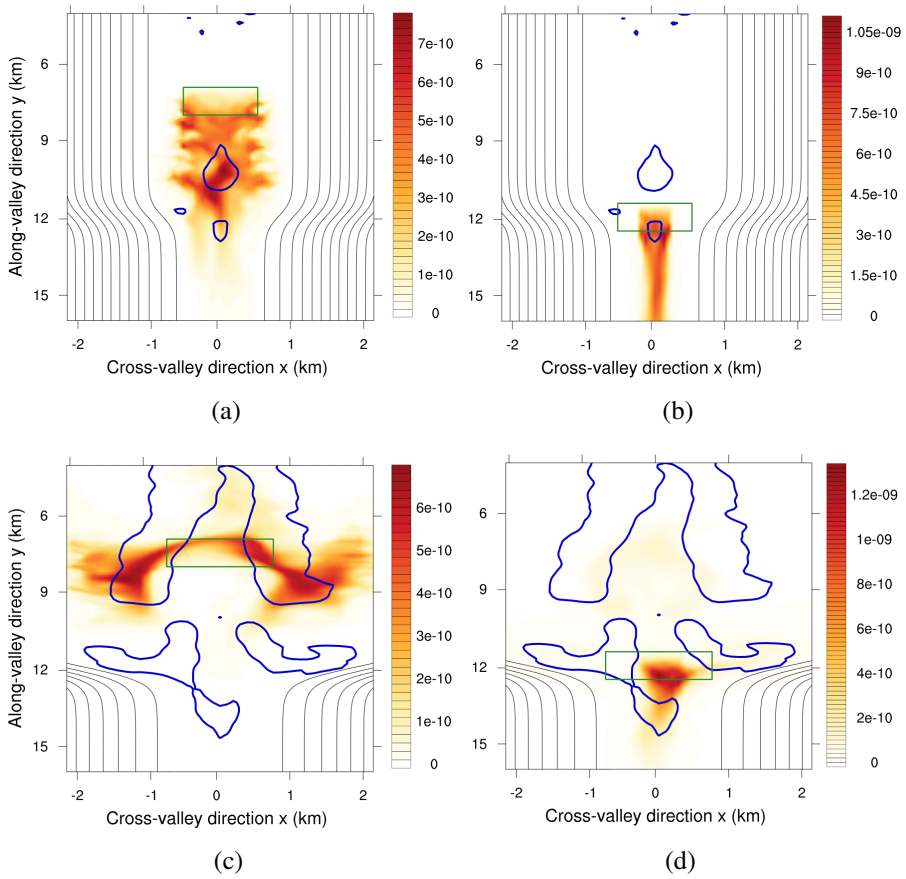

Fig. 4.9 *Contour plot of the tracer concentration at the end of the simulation (averaged over the last 15 minutes of simulation) for a) $TrP1_1$, b) $TrP1_3$, c) $TrP2_1$ and d) $TrP2_3$ averaged over the first 30 m along the vertical. Blue lines correspond to the locations where the critical stagnation zones are located (Figs. 4.7e and 4.7f). Green rectangles represent the emission zones for each of the tracers. Note that the label bar is different for each of the pictures.*

of the simulation is about the 25%. Regardless of the ventilation during the last part of the simulation, almost twice as much mass remains close to the release zone for $P2$ compared to $P1$.

Tracers $TrP1_5$ and $TrP2_5$ emitted half way along $\mathscr{D}$ display a very similar behaviour since they are advected in the down-valley direction once the along-valley flow develops (around 120 minutes). The latter indicates that the dynamics in $\mathscr{D}$ away from $\mathscr{J}$ is independent of the geometry of the neighbour valley for the range of geometrical parameters considered in this work.

R_M provides information about the lifetime of the tracers in the different sections of the valley-system, but a quantification of the valley ventilation efficiency is still required. A

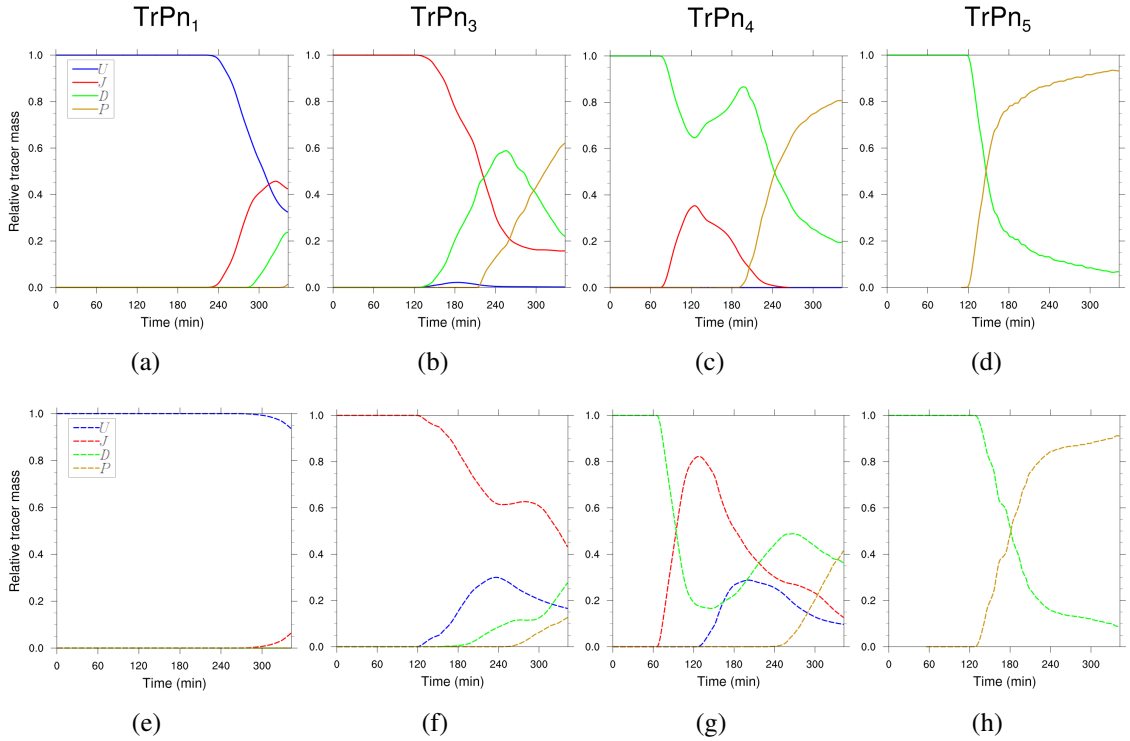

Fig. 4.10 *Time series of the relative tracer mass (R_M) at the different control volumes in the system ($V_{\mathscr{U}}$, $V_{\mathscr{J}}$, $V_{\mathscr{D}}$ and $V_{\mathscr{P}}$) for tracers $TrPn_1$ (released at $\mathscr{U}$), $TrPn_3$ (released at $\mathscr{J}$), $TrPn_4$ (released at the beginning of $\mathscr{D}$) and $TrPn_5$ (released at the centre of $\mathscr{D}$). Note that $n = 1$ for $P1$ and $n = 2$ for $P2$. Solid lines represent values of $P1$ (top row), while dashed lines stand for $P2$ (bottom row). The location of the emission source of each of the tracers is presented in Fig. 4.1a.*

synthetic account of the ventilation character of the different sections of the valley-system can be provided by computing the residence time of the tracers at each section. The residence time can be seen as a volume parameter that aims to describe the general exchange characteristics of a control volume leaving aside the identification of the underlying physical processes or their spatial distribution Monsen et al. (2002). The residence time $\mathscr{T}$ is defined simply as:

$$\mathscr{T} = \frac{m_{total}}{f} \tag{4.3}$$

where m_{total} is the total mass stored in the control volume at the time when the calculation is performed and f is the mass fluxes through the boundaries. When the fluxes out of the control volume are near zero or into the volume, $\mathscr{T}$ will tend to infinity (i.e. the tracers will remain always inside the control volume). On the other hand, if the tracer flux is large compared with the tracer mass in the volume, the tracer residence time will tend to zero.

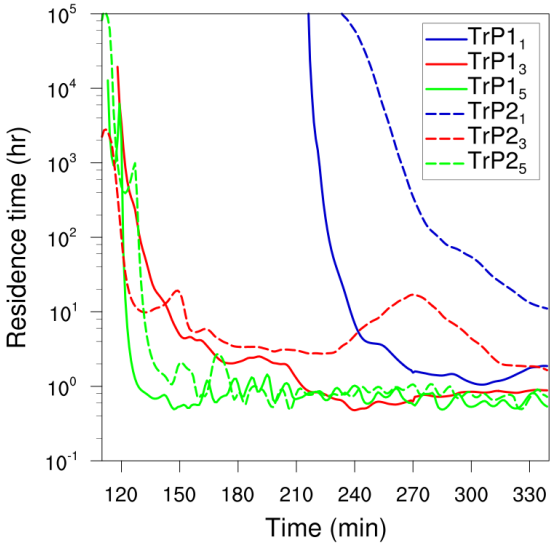

Fig. 4.11 *Time series of the residence time ($\mathscr{T}$) of tracers $TrPn_1$ (blue lines, tracer released at $\mathscr{U}$), $TrPn_3$ (red lines, tracer released at $\mathscr{J}$) and $TrPn_5$ (green lines, tracer released at $\mathscr{D}$). Note that $n = 1$ for $P1$ and $n = 2$ for $P2$. Solid lines represent values of $P1$, while dashed lines stand for $P2$. The location of the source of each of the tracers is presented in Fig. 4.1a. Please note that for the vertical axis $\mathscr{T}$ the unit used is hours.*

Figure 4.11 displays a compilation of the tracer residence time for three tracers. The tracer released at the centre of $V_{\mathscr{D}}$ ($TrP1_5$) is mainly subjected to ventilation, the residence time reaches a quasi-steady state ($\mathscr{T} \approx 45$ minutes) once the along-valley wind is established after 120 minutes. This value is used as a reference for ventilation residence time and is denoted by $\mathscr{T}_v$. Note that such $\mathscr{T}_v$ resembles an average wind speed in this valley section of about 2.6 m s^{-1}, which is consistent with what was presented in Fig. 4.2b for the last two hours of simulation. The oscillatory behaviour of $\mathscr{T}$ (of about +/-15 minutes) may be a consequence of the oscillation in the wind speed magnitude previously encountered in drainage valleys similar to $V_{\mathscr{D}}$ (Quimbayo-Duarte et al., 2019a). $TrP1_3$ displays a similar behaviour as the one of pure ventilation, reaching a very close value (60 minutes) just before the four hours of simulation. Conversely, for $TrP1_1$ the value of $\mathscr{T}$ at the end of the simulation was two times larger than the one of $\mathscr{T}_v$ (please be aware of the logarithmic scale of the vertical axis in figure 4.11), indicating that the stagnation character of $V_{\mathscr{U}}$ is noted until the end of the simulated period for $P1$. Even with the zones of stagnation detected for $P1$, the system as a whole could be seeing as a drainer valley due to the ventilation character evidenced in Fig. 4.11.

As it was mentioned before, the wind dynamics in the last portion of $V_{\mathscr{D}}$ is very similar for both $P1$ and $P2$ (see Figs. 4.2b and 4.2d). Tracer $TrP2_5$ has a very similar behaviour

than $TrP1_5$, $\mathscr{T}$ quickly reaching a quasi-steady state near the value of $\mathscr{T}_v$ and remain like this until the end of the simulation. Tracer $TrP2_3$ starts to be ventilated at about 120 minutes, but due to the complexity of the system after four hours $\mathscr{T}$ increase, reflecting the change of direction of the along-valley flow transporting back to $V_{\mathscr{J}}$ the tracers advecting them in the up-valley direction. Afterwards, it seems to reach a stable regime that is a almost three times larger than $\mathscr{T}_v$, implying that at least by the end of the simulated period such section does not show ventilation of tracers. Finally, the residence time of $TrP2_1$ at $V_{\mathscr{U}}$ clearly expresses the low ventilation shown above. At the end of the simulation it display a $\mathscr{T}$ of about 10 hours, indicating that this portion of valley is characterized as a stagnation zone.

Arduini et al. (2017) following the work of Whiteman et al. (1996) indicates that $P1$ is considered as a drainer valley, and $P2$ can be considered as a trapper. From the tracer experiment presented here it is possible to infer that for $P2$ the system as a whole could not be considered as a trapper due to the strong ventilation evidenced at the end of $V_{\mathscr{D}}$.

4.6 Summary and Conclusions

Numerical simulations were performed to examine the response of the transport of air pollutants, modelled as passive tracers, to orographic variations along the axis of an idealized version of an Alpine valley during wintertime after the evening transition. A system of two valleys sharing the same axis, with one of the valleys opening on a narrower valley, which opens on a plain, is considered. Two sets of simulations were considered, named $P1$ and $P2$ for which the valley-floor width of the downstream valley section is the same ($\mathscr{L}_d = 360$ m), but that of the upstream valley section ($\mathscr{L}_u$) was set to 1440 m ($\mathscr{L}_u/\mathscr{L}_d = 4$) and 4230 m ($\mathscr{L}_u/\mathscr{L}_d = 11.5$), respectively. The transport of passive tracers across the domain has been analysed for six different tracers released along the valley-axis. The main conclusions of this work can be summarized as follows:

- The change in the thermal structure of the atmosphere within the different sections of the valley and the plain generates a horizontal pressure gradient that leads to the development of an along-valley flow. For $P1$ it is up-valley in the upstream valley section during the first three hours of simulation and then reverses in the downstream direction for the rest of the simulated time period (six hours). For $P2$ a faster up-valley flow persists in the upstream valley section until the end of the simulated period. These differences in the dynamics between P1 and P2 translate to differences in the horizontal

mass flux out of the upstream valley section: it is 1.5 times larger for $P1$ than for $P2$ (see Fig. 4.3).

- The methodology proposed by (Allwine and Whiteman, 1994) to predict locations prone to ventilation, stagnation and recirculation was evaluated and found to work well for predicting areas with high tracer concentration. Indeed, the zones where critical stagnation is detected agree well with zones of high tracer concentration (see Fig. 4.9). However, the relationship between areas identified as prone to stagnation and the zones of high tracer concentration should be considered with caution since the variability in the concentration of air pollutants is not only a function of atmospheric dynamics but also of the emission location and rate, as evidenced in Fig. 4.9d.

- The sizable change in the cross-sectional area between the upstream ($\mathscr{U}$) and downstream ($\mathscr{D}$) valleys affects atmospheric dynamics, and hence tracer transport across the domain. The export of tracers out of $\mathscr{U}$ is reduced by about 50% for $P2$ compared to that for $P1$. Intra-valley transport of tracers is also reduced in $\mathscr{D}$. By the end of the simulated period $\tilde{8}0\%$ of the total mass emitted for tracer $TrP1_4$ (at the beginning of $\mathscr{D}$) has been transported out of the valley system while for tracer $TrP2_4$ (which is emitted at the same position but for $P2$) only $\tilde{4}0\%$ of the total mass emitted have left the valley system (see Figs. 4.10c and 4.10g).

- The ventilation efficiency within the different sections of the valley-system was quantified by a residence time. For $P1$ the residence time within $\mathscr{U}$ (about two hours) is more than twice that within $\mathscr{D}$ (about 45 minutes) at the end of the simulated time period (Fig. 4.11). This difference in the ventilation efficiency between $\mathscr{U}$ and $\mathscr{D}$ is more pronounced for $P2$, for which the ventilation efficiency for $\mathscr{U}$ (about 10 hours) is reduced by more than a factor ten compared to that for $\mathscr{D}$ (about 45 minutes).

Acknowledgements

This work has been supported by a PhD grant provided by the Colombian Administrative Department of Science, Technology and Innovation, COLCIENCIAS. Numerical simulations were run on the French national HPC facilities at CINES.

Chapter 5

Drivers of Severe Air Pollution Events in a Deep Valley During Wintertime

Abstract

During wintertime, urbanised mountainous areas are frequently affected by severe particulate air pollution episodes due to the direct emission of particulate matter (PM) and precursor gases leading to secondary aerosols. In such confined terrain, the atmospheric stability (which may suppress turbulent mixing and block ventilation), plays a fundamental role in air quality issues. Stable boundary layers in valleys are often related to persistent cold-air pools, which can last for days and lead to high pollutant concentrations exceeding air-quality standards. In the present work we focus our attention in a section of the Arve River Valley, located in the northern French Alps. In recent years the relatively small city of Passy, located in this valley, has regularly experienced air-quality issues during wintertime when the atmosphere is strongly stratified. Passy has become one of the most polluted cities in the region, recording pollution levels as high as Lyon, which is the third large city in France and has ten times more inhabitants than Passy. The contribution to local air pollution from different valley sections have been studied. Results suggest that the influence of the pollution from the tributaries is small compared to that from local sources, suggesting that in-situ emissions are primarily responsible for the high concentration of PM in the valley. A predominant down-valley flow is observed during the simulated time period, which results in a rather small transport of pollution in the up-valley direction. The ventilation characteristics of the valley and their influence on the PM concentration have been investigated. The analysis indicates that due to

the limited ventilation in some particular sites inside the valley, as the area covering the town of Passy, the hourly variability of PM concentration at these sites is mainly driven by that of local emissions.

5.1 Introduction

During the winter season, mountainous areas are affected by episodes of severe air pollution when atmospheric stability increases due to the formation of a temperature inversion that suppresses vertical mixing in the lower atmosphere (Chazette et al., 2005). Particulate pollution is of particular concern since it has been shown to have a strong effect on human health, from asthma to increased risk of heart attacks (Anderson et al., 2012b).

The relationship between meteorology and high concentration of particulate matter (PM) in the atmosphere has been explored extensively in the literature. Smith et al. (2001) used computer-calculated trajectories of air masses together with relevant meteorological data to interpret a three-year-long data set (1995-1997) of PM_{10} collected in London, UK. The model proved to be able to describe well 60 to 65 % of the observed variation of PM_{10} in this time period. The study concluded that the local climate is not the main driver of concentration peaks; in fact, an advection of PM_{10} from external sources was shown to play an important role by adding in some cases up to 20 μg m^{-3} to the concentration recorded in the city. Vardoulakis and Kassomenos (2008) analysed a three-year-long data set (2001-2003) to explore the relationship between concentrations of PM_{10}, other pollutants (such as CO and NO_x) and meteorological parameters in two European cities (Athens, Greece and Birmingham, UK). The authors found a positive correlation during the cold season between PM_{10} concentration, low wind speed and solar radiation, which are normally associated with stable boundary layers.

The impacts of stable layers on air quality in complex terrain are well known to be more significant than over flat regions. Topographic effects lead to stronger and deeper temperature inversions that block ventilation and prevent mixing of pollutants. In the urbanized Salt Lake Valley (Utah, USA) for example, Whiteman et al. (2014) studied the relationship between local weather conditions and particulate air pollution in the winter season using a 40-year long data set (1973-2003). PM_{10} (particles with an aerodynamic diameter less than 10 μm) concentrations in the area were found to be highly correlated with the valley heat deficit, a vertically integrated measure of atmospheric stability, especially on days with snow-

covered surface, low clouds and fog, which are often associated with long-lasting pollution episodes. Neemann et al. (2015) investigate the relationship between the development of a cold air pool and high concentrations of pollutants in the Uintah Basin, Utah, USA, for a one-week-long pollution episode in February 2013. Numerical model results showed a high sensitivity of boundary-layer development and ozone concentrations to snow cover. By increasing surface albedo and reducing short-wave radiation absorbed by the surface, snow cover leads to a colder temperature near the surface and a more stable boundary layer, leading to higher concentrations of pollutants. Largeron and Staquet (2016) investigated the relationship between the dynamics of persistent cold-air pools and episodes of high particulate pollution during the winter in the Grenoble valley in the northern French Alps using data from ground-based weather and air quality stations in the area during the winter 2006-2007. A criterion based solely on the temperature difference between the valley floor and an elevated mountain-top site was developed to detect persistent temperature inversions in this deep valley. During this winter, nine temperature inversion episodes leading to high particle pollution episodes were identified. Only one pollution episode during this winter was not related to a temperature inversion; out to long-range transport of pollution.

All previous studies indicate that the strength and duration of temperature inversion are responsible for the high concentration of pollutants recorded during wintertime pollution episodes in complex terrain. However, the rate and location of local emission sources, and atmospheric chemistry, need to be considered to determine the spatial and temporal distribution of pollutants. In the present study we focus our attention on the Arve River Valley, located in the northern French Alps (see Fig. 5.1). This valley has experienced particularly high levels of particulate air pollution in the winter season during recent years (Piot, 2011), with PM_{10} concentrations exceeding the European standards (that is more than 35 days a year with a daily average greater than 50 μgr m^{-3}) set by the Directive 2008/50/EU. The small town of Passy (11,214 inhabitants, according to the 2012 census), is one of the main concerns of local authorities due to the high particulate air pollution registered in winter (Atmo-Auvergne-Rhone-Alpes, 2018).

The surrounding summits, culminating at more than 2000 m above the valley bottom, together with the change in the cross-sectional area of the valley near the town of Passy, lead to a fairly confined atmosphere that does not allow pollutants emitted at the bottom of the valley to be ventilated outside. This effect becomes very intense when the valley atmosphere is dynamically decoupled from the upper atmosphere (as is the case during an anticyclonic regime), hereby trapping cold air within the valley for multiple days, often referred to as a

persistent cold air pool (PCAP). In this region, PCAPs can last for several days (and even weeks) and may extend up to about 800 m above the valley floor (Arduini, 2017).

During winter 2014-2015, a large number of instruments were deployed in the vicinity of the city of Passy a field campaign called Passy-15 (Staquet et al., 2015, Paci et al., 2017). The main objective of this field campaign was to collect data to characterize the atmospheric dynamics in this section of the valley and link it to pollution episodes. Using these data Chemel et al. (2016) explored the relationship between the temporal variability of PM_{10} concentration and the temporal variability of the valley heat deficit. The authors found that when calculating the squared Pearson product-moment correlation coefficient (r^2) using daily-averaged data, the correlation between the valley heat deficit and the PM_{10} concentration was as high as r^2 equal to 0.69. However, the hourly evolution of the PM_{10} concentration was found relatively complex and could not be explained simply by the hourly variability of the heat deficit of the valley. The concentration of PM_{10} in the lower atmosphere is strongly affected by variables such as local emissions of PM_{10}, local dynamics and the position where the measurement is made. An analysis of local atmospheric circulation was performed by Sabatier et al. (2018) for a section of the Arve River Valley using data from a Doppler Lidar during the PCAP event which was associated with the first intensive period (IOP1) of the Passy-15 field campaign (between 6 and 13 February 2015). The authors attempted to explain the high levels of PM_{10} recorded and the rather special spatial distribution of pollutants along the valley during this episode. As expected, the atmospheric dynamics during the episode were characterized by a strong temperature inversion together with calm winds that prevented the ventilation of pollution out of the valley. In fact, light winds favoured the formation of hot spots of high PM_{10} concentration, highlighting the important role of local wind dynamics in the valley. Both studies provided important insights in the understanding of the severe pollution episodes recorded in this section of the valley, and more generally in similar valleys, but also noted the need for numerical simulations to better understand this complex situation.

Arduini (2017) used results from high-resolution numerical simulations to explore the local and non-local drivers of the PCAP event associated with the IOP1 of the Passy-15 field campaign. The author analysed the different stages of the event and pointed out the importance of the tributary valleys in the persistent stage of the PCAP, which together with the advection of air from above determine the height of the inversion layer. Throughout the episode, complex interactions took place between the local dynamics in the valley and the flows in and out of its main tributaries. This work provided a detailed account of the atmospheric dynamics during the PCAP event, which as shown in other studies (e.g., Silcox et al. 2012, Green et al. 2015, Baasandorj et al. 2017), have a determinant role in the

accumulation of pollutants in such complex terrain. However, the origin of the pollution episodes and the horizontal heterogeneity in the distribution of pollution in the valley remain outstanding issues.

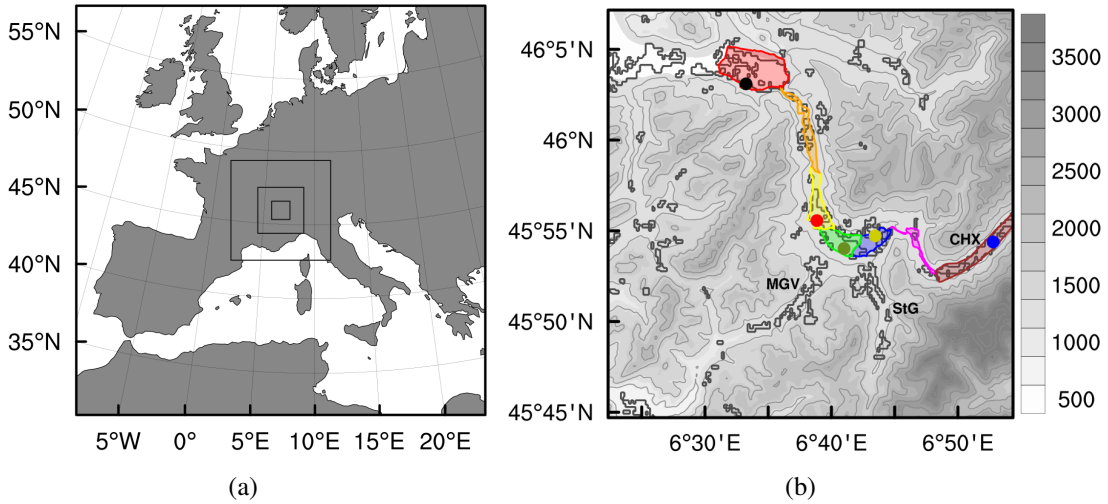

Fig. 5.1 *a) WRF model domain d01; domains d02, d03 and d04 noted with the boxes. b) Topographical representation of the innermost domain d05. Black contours indicate urban areas in the domain. The locations of the air quality stations in the zone are marked with coloured dots; Chamonix (blue), Passy (yellow), Sallanches (red) and Marnaz (black). The exact locations of the stations are documented in table 5.3. In addition, the location of the main measurement site in Passy-15 is denoted with the green dot. The black letters indicate the main tributaries leading to the towns of Megève (MGV), Saint-Gervais-les-Bains (StG) and Chamonix Mont-Blanc (CHX). The color areas represent a sub-array of the emissions along the valley. The color sections are named as Se_1 (red area), Se_2 (orange area), Se_3 (yellow area), Se_4 (green area), Se_5 (blue area), Se_6 (magenta area) and Se_7 (brown area).*

In the present work, we used numerical simulations coupled with a chemistry module to examine the possible drivers of particulate air pollution in the section of the Arve River Valley near Passy using a configuration similar to that presented in Arduini (2017). The numerical simulations were designed to simulate the IOP1 of the Passy-15 field campaign. The numerical model and the emissions inventory used are presented in Sect. 5.2. Section 5.3.1 presents a summary of the meteorological model performance, a sensitivity test and the main characteristics of the atmospheric dynamics during IOP 1. The coupling between the meteorological and chemical model is evaluated and discussed in Sect. 5.3.1. The horizontal distribution of pollution is presented in Sect. 5.3.2. Finally, conclusions along with a discussion are presented in Sect. 5.4.

5.2 The Numerical Model

5.2.1 Meteorological Model Configuration and Physics

The Weather Research and Forecasting (WRF) (Skamarock et al., 2005), version 3.5.1, was used to perform the numerical simulations. The model was coupled to a chemical module (WRF-Chem) to model the diffusion and transport processes of passive tracers emulating the behaviour of PM_{10} in the atmosphere. In this work, we assume that under winter conditions, PM_{10} found in the atmosphere has a low chemical reactivity. In fact, elemental carbon (EC), which in winter represents a significant fraction of the total mass of PM_{10} (up to 15%, Aymoz et al. 2007), is well known for its low chemical reactivity in the atmosphere.

The simulation was performed using five nested domains centred in the airport of Sallanches (45.935 °N, 6.636 °E) and was carried out in three steps. The first three domains (d01, d02 and d03) were run in a one-way online nested configuration, covering the continental scales (see Fig. 5.1a). Data from the European Centre for Medium-Range Meteorological Forecasts (ECMWF) were used to initialize and provide the lateral boundary conditions for the outermost domain, and were updated every 6 hours. The simulation started on February 7, 2015, at 12:00 (UTC time) and was run for 7 days until February 14, 2015, at 12:00 (UTC time). The size, horizontal and vertical resolutions along with the time step for each domain are listed in table 5.1.

Domain	nx, ny, nz	$\Delta x = \Delta y$	Δz_{min}	Δt
d01	202, 202, 46	15 km	42 m	30 s
d02	246, 246, 46	3 km	42 m	6 s
d03	340, 340, 46	1 km	42 m	2 s
d04	406, 406, 92	333 m	21 m	0.6 s
d05	382. 382, 92	111 m	9.2 m	0.06 s

Table 5.1 *Main parameters used in the simulations. The number of grid points nx, ny, nz correspond to the east-west, north-south and vertical directions, respectively. The vertical coordinate is stretched with height, Δz_{min} represents the height above the ground of the first grid point, the first mass point being located at $\Delta z_{min}/2$ m.*

In a second step, the results obtained in the first run for domain d03 were used as initial and lateral boundary conditions for domain d04 through a down-scaling process. The lateral boundaries were updated every 10 minutes. This simulation for domain d04 was run for six days, from the 8th at 12h00, to the 14th at 12h00 February 2015.

Finally, the same downscaling methodology was used to produce the initial and lateral boundary conditions for domain d05, which used a grid resolution of 111 m in the horizontal and 92 grid points in the vertical direction. WRF uses a vertical stretched coordinate that provides a finer resolution near the ground. Two vertical discretizations were tested (see Fig. 5.4): one with the first grid point at 21 m above ground level (V_{prof1}), and a second one with the first grid point at 9.2 m above ground level (V_{prof2}) for which the first mass point is located at 10.5 m and 4.6 m for V_{prof1} and V_{prof2}, respectively. The simulation for domain d05 was run from the 9th at 12h00, to the 13th at 12h00 February 2015.

The planetary boundary layer (PBL) was parametrized in the first online run (for d01, d02 and d03) using the Yonsei University (YSU) scheme (Hong, 2010). For the two innermost domains (d04 and d05), the PBL has been explicitly resolved using a turbulent kinetic energy (TKE) 1.5 order closure employing a Smagorinsky coefficient C_s equal to 0.1. The rest of the physical and dynamic options were shared by all domains. The temporal discretization of the model equations used a Runge-Kutta scheme of third order, for the acoustic modes a time-splitting technique was implemented. The scheme developed by Morrison et al. (2005) was used to parametrize the microphysics in the model with the inclusion of the modifications on the treatment of ice fog proposed by Neemann et al. (2015). The Rapid Radiative Transfer Model (Mlawer et al., 1997) was used to parametrize both shortwave and longwave radiation. The Noah land surface model (Chen and Dudhia, 2001) was implemented to model the surface-atmosphere exchanges, with four soil layers. The revised MM5 Monin-Obukhov scheme (Jiménez et al., 2012) was used to model the surface layer physics.

5.2.2 Geographical Location and Terrain Representation

The Arve valley is located in the north of the French Alps, near the French-Swiss border (see Fig. 5.1). In the winter season, the local time is UTC+1. The three main localities in this section of the valley, from the upstream to the downstream section, are Passy, Sallanches and Marnaz, with a population of 11,485, 16,722 and 5,476 inhabitants, respectively (Institut national de la statistique et des études économiques, 2015). In Passy, the valley floor is about 588 m above sea level (a.s.l.) and decreases along the 23 km length of the valley to 475 m a.s.l. in Marnaz (see Fig. 5.1b). The valley is surrounded by high mountains that reach up to 2,700 m.a.s.l. in the western and northern parts of the valley. The highest peak in the area is Mont Blanc (4808 m a.s.l.), located about 18 km southeast of Passy. The city of Chamonix is located about 20 km upstream in the valley. The valley has two main tributaries leading to the cities of Megève and Saint-Gervais-les-Bains (see Fig. 5.1b).

Data from the Shuttle Radar Topography Mission (Farr et al., 2007) at a resolution of about 90 m was used to create the orography. At this horizontal resolution, the maximum slopes of the terrain can reach values close to 75°. These steep slopes in the area generate numerical instabilities in the model. To overcome this problem, a filter was implemented to reduce the maximum slope angle to 42°. The general shape of the topography is retained while maintaining the main small-scale characteristics of the topography of the domain.

Due to the importance of the snow cover in the surface-atmosphere interactions (Tomasi et al. 2014; Neemann et al. 2015; Arduini 2017), a methodology was developed for the initialization of snow cover in the model. The high horizontal resolution of the model required an adequate representation of the snow layer during the simulated days, which is not available in the numerical model reanalysis product that is produced at a resolution of about 15 km. MODIS/Terra (MOD10_L2) satellite data for snow cover at a resolution of 500 m (Hall et al., 2006) averaged between 5 and 10 February 2015 was thus interpolated at the horizontal resolution in the inner most domain to better represent the initial snow fields in the simulations (see Arduini, 2017, for details).

5.2.3 Emission Input

The emission input used in the simulations is based on an emissions inventory developed by the local air quality agency of the Auvergne Rhône-Alpes region (Atmo-Aura) for the year 2015 (Atmo-Auvergne-Rhone-Alpes, 2017). The emission inventory is available at a resolution of 100 m throughout the whole region. The inventory incorporates several pollutants, such as nitrogen oxides, non-metallic volatile organic compounds, polycyclic aromatic hydrocarbons, heavy metals and suspended particles (such as PM10), which is the focus of the present work.

The methodology used to compile the emission inventory is a hybrid of bottom-up and top-down approaches. In general, when data are available at the finest scale (road counts, lists of major industrial sources, i.a.), the bottom-up approach was favoured. Once the most accurate data are obtained, it is aggregated at the city level for the calculation of emissions on a regional scale. In cases where fine-scale data are not available, regional data are disaggregated at the city level, applying the top-down method. This disaggregation process is carried out following key information for all towns in the region, such as population and employment. A final adjustment of the data is made by crossing the final product with the

SNAP	Classification	% in mass
1	Combustion in energy and transformation industries	1,28
2	Non-industrial combustion plants (Residential heating)	61,24
3	Combustion in manufacturing industry	2,56
4	Production processes	9,55
5	Extraction and distribution of fossil fuels and geothermal energy	0,00
6	Solvent and other product use	0,75
7	Road transport	19,42
8	Other mobile sources	3,03
9	Waste treatment and disposal	0,97
10	Agriculture	1,20
11	Other sources and sinks	0,00

Table 5.2 *The contribution of each SNAP sector in mass (percentage) to the total PM_{10} emission in the numerical domain; according to the emission inventory provided by Atmo-Aura for the year 2015.*

information provided by the Observatoire de l'énergie et des gaz à effet de serre (OREGES, Energy and greenhouse gas observatory in English) and its partners.

The inventory was used with a database that allows the assignment of appropriate emission factors for the calculation of emissions. The emission factors were extracted from a compilation of different reference works, mainly from the Centre interprofessionnel technique d'études de la pollution atmosphérique (CITEPA, Interprofessional technical centre for air pollution studies in English) reference guide.

The different emission sectors were categorised using the classification proposed by the European Topic Centre on Atmospheric Emissions (ETC/AE), which classifies the activities generating an emission of pollutants into the atmosphere using the Selected Nomenclature of Air Pollution Sources (SNAP). The eleven SNAP categories, or sectors as it is commonly named, are considered and their contribution to the total emission of PM_{10} (in mass) in the area is presented in Table 5.2. The table shows that in this area three main contributors account for about 90% of the total emissions: residential heating, production processes and road transport, contributing 61.24%, 9.55% and 19.42%, respectively. These estimates are inline with the findings of Aymoz et al. (2007) that biomass combustion emissions appear to have a significant impact on organic carbon concentrations during the winter season, hence on PM_{10} mass concentration in the same area (Chamonix).

Because the emission inventory is provided as the total mass emitted for the whole year, a disaggregation of the total value must be made for each simulated day. Such temporal profiles vary between seasons, months and even according to the ambient temperature at the place

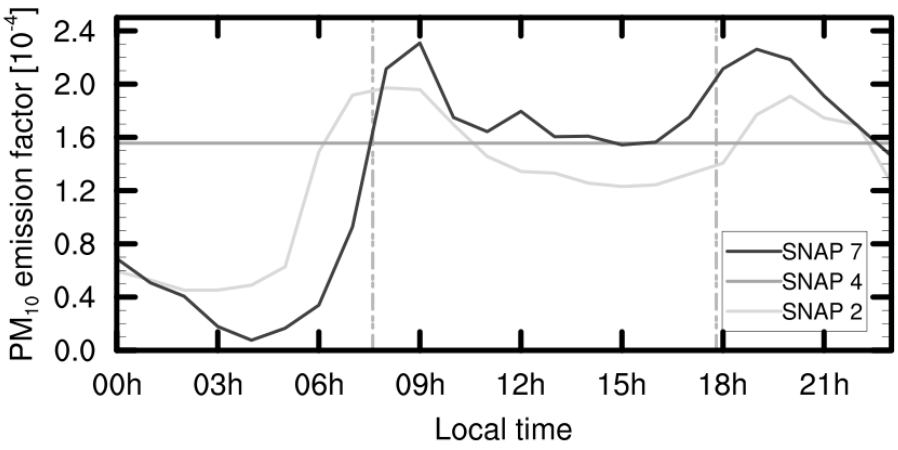

Fig. 5.2 *First level disaggregation in time of total year emission for a complete daily cycle during the first week of February 2015 for the three main SNAP sectors emitting in the area, SNAP 2 (residential heating), SNAP 4 (industrial combustion) and SNAP 7 (route transport). Vertical dashed lines stands for the average sunrise and sunset times during the simulation period.*

of emission (Atmo-Auvergne-Rhone-Alpes, 2017). In the present work, we implemented a first level (without considering the ambient temperature) hourly disaggregation using a different profile for each SNAP sector based on the emission factors recommended by Atmo-Aura (Atmo-Auvergne-Rhone-Alpes, 2017) and the Netherlands Organization for Applied Scientific Research, TNO (Schaap et al., 2005). Figure 5.2 presents the daily evolution of the emissions factors for the two main SNAP sectors emitting in this area (SNAP 2 and SNAP 7); the third largest contributor (SNAP 4) is represented by a constant emission factor.

Location	***Latitude***	***Longitude***	***Height [m .a.s.l.]***
Chamonix	45°55'33.24" N	6°52'11.71" E	1038
Passy	45°55'24.71" N	6°42'49.10" E	588
Sallanches	45°56'06.47" N	6°38'08.02" E	542
Marnaz	46°03'27.86" N	6°32'00.38" E	504

Table 5.3 *Localisation of the four air-quality stations in the domain. Colour dots in figure 5.3 represent the locations of the four air-quality stations and the position of the IOP measurement site in the map.*

The emission input file was compiled with all PM_{10} emissions in the area considered. WRF-Chem model read the emissions input every hour and all emissions were released at ground level. A first numerical experiment using all the PM_{10} emissions in the area was performed as a reference base line simulation. In a second step, an experiment dividing the Arve River Valley and the emissions therein into seven sections was carried out (see Fig. 5.1). Each color area has been carefully delimited to represent the emissions at the valley floor, where the principal contributors are located. The experiment provided the opportunity to

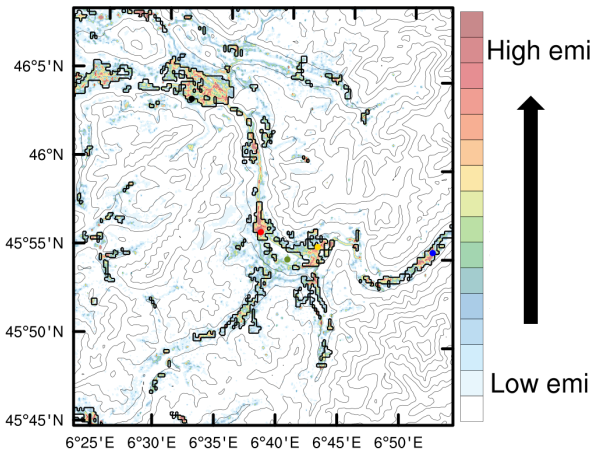

Fig. 5.3 *Horizontal distribution of the emission input in the domain for a complete day (9th February 2015) overlaid over contours of the terrain height (grey contours). Black contours indicate urban areas in the domain. The locations of the air quality stations in the zone are marked with coloured dots; Chamonix (blue), Passy (yellow), Sallanches (red) and Marnaz (black). In addition, the location of the main measurement site in Passy-15 is denoted with the green dot. No scale is provided for confidentiality reasons.*

distinguish the contribution (on a very local level) of each of the sections along the valley on the total PM_{10} concentration by devoting a different variable to the emissions in each of the sections. Finally, worth to mention that the area covered by the innermost domain (d05) encompasses four air quality stations (see table 5.3).

5.3 Results

5.3.1 Model Performance

5.3.1.1 Atmospheric dynamics

The PCAP event associated with the IOP1 of the Passy-15 campaign formed in the Arve River Valley due to the presence of an anticyclone in the upper atmosphere that exported warm air above the valley (see Fig. 5.5). This event lasted for four days and triggered a severe particulate air pollution episode in the valley (see Fig. 5.5a). The correct representation of the atmosphere during those days is very important for the correct representation of the distribution of PM_{10} in the valley.

The numerical simulations presented herein rely on previous work by Arduini (2017). The present work includes an improvement of the vertical resolution by increasing it almost by a factor of two in the first 200 m (see Fig. 5.4). This allows the model to better represent the lower atmosphere, which in this case is fundamental because the main processes of transport and mixing of pollutants in the area occur close to the ground. A second difference between the simulations presented here and the previous simulation by Arduini (2017) is that we ran the model continuously for the four-day period, as opposed to a reinitialisation every 24 hours. The impact of these two modifications is evaluated below.

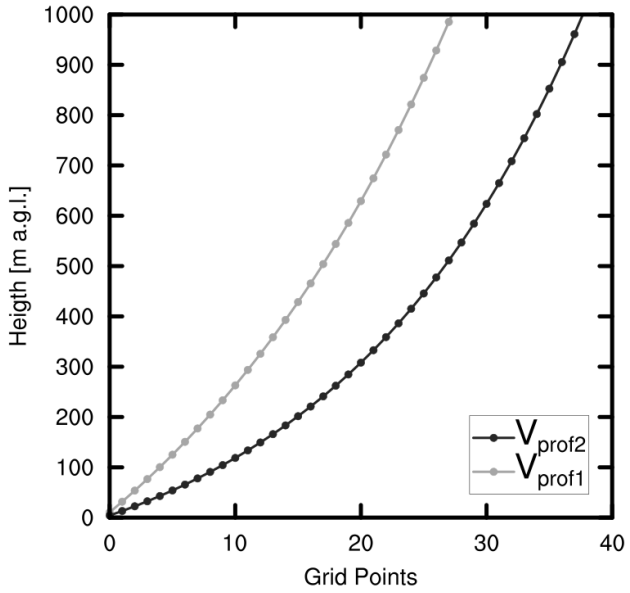

Fig. 5.4 *Vertical discretization of the model innermost domain (d05) in the first 1000 m above ground level. The first vertical discretization (grey line) is the one used by Arduini (2017), the second vertical discretization (black line) has been developed for this set of simulations. Each marker of the lines represents a grid point in the model. Both profiles were taken at the bottom of the valley from 556.6 m above sea level.*

We focused this sensitivity study on 60 hours of simulation between February 11, 2015, at 00h00, and February 13, 2015, at 12h00 UTC time, that is on the persistent stage of the PCAP event (Arduini, 2017). Results of three simulations were compared: I. That presented in Arduini (2017) using the first vertical discretization (see Fig. 5.4) and restarting the simulation every 24 hours (S_{ard}). II. A simulation using the first vertical discretization (see Fig. 5.4) and run continuously throughout the period (S_{vert1}). III. A simulation using the second vertical discretization (see Fig. 5.4) and run continuously throughout the period (S_{vert2}).

Before comparing the results of these three simulations, the validity of the predictions of simulation S_{vert2} is assessed in Fig. 5.5 by comparison with field measurements using vertical profiles of potential temperature obtained from radiosounding ascents over the IOP1 (The same comparison was performed by Arduini (2017) for simulation S_{ard}). The model captured the formation of a CAP in the lower atmosphere between 9th and 10th February, then, it was followed by a persistent stage until the evening of 12th February. At the end of the simulation period (13th February), the destruction of the CAP is observed both in the simulated data and in the field data bearing evidence of agreement between the simulated data and the field measurements. The relation between the development of such persistent CAP (PCAP) episode and the increasing in the PM_{10} concentration is evidenced in Fig. 5.5a, note that during the destruction stage of the PCAP episode the PM_{10} concentration dramatically decrease.

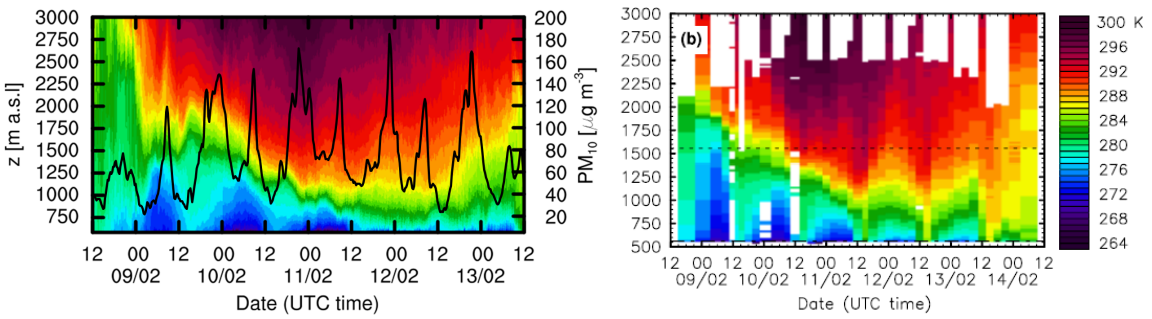

(a) (b)

Fig. 5.5 *a) Simulation S_{vert2}. Temporal evolution of the vertical structure of the cold-air pool by computing the potential temperature vertical profile. Data were taken at the location of the main measurement site of the Passy-15 field campaign and are overlaid with the PM_{10} concentration registered over the same time period by the air quality station at Passy (black line). b) Temporal evolution of the vertical structure of the cold-air pool obtained by compiling potential temperature profiles from the radiosounding ascents and wind profiles retrieved from LiDAR (below 1050 m a.s.l.) and wind profiler (above 1050 m a.s.l.). Figure b) was extracted from Arduini (2017) with the author's authorization.*

The effects of the model restart on the thermal structure of the atmosphere seems to play an important role. Results from the model runs continuously shows cooler air close to the ground and a deeper cold-air pool (see Fig. 5.6a and 5.6b).

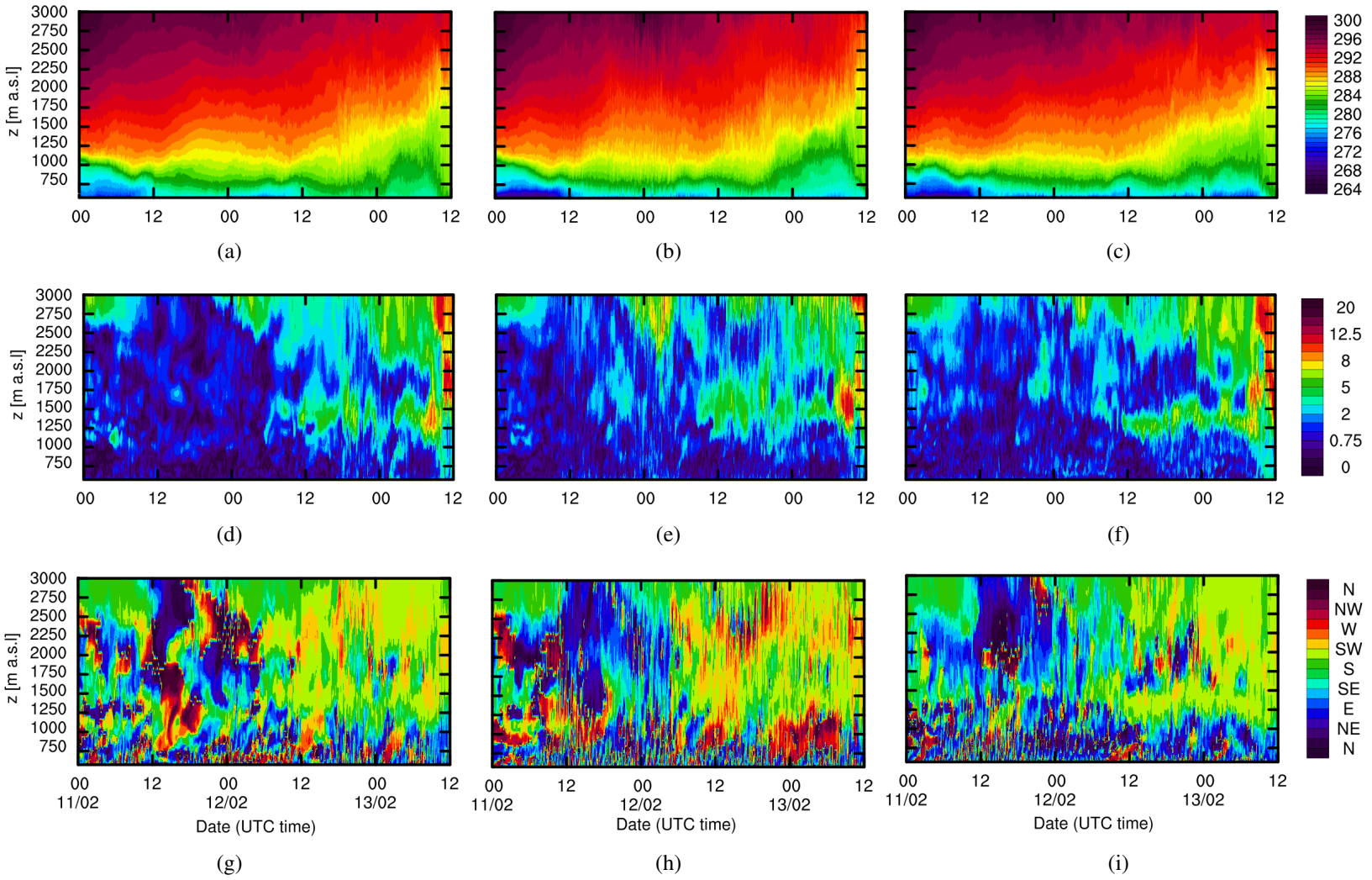

Fig. 5.6 *Temporal evolution of the vertical structure of the cold-air pool for simulations S_{ard} (left column), S_{vert1} (mid column) and S_{vert2} (left column) by computing the potential temperature vertical profiles (top row), wind speed (mid row) and wind direction (bottom row). All data were taken at the location of the main measurement site in Passy-15.*

Running the model continuously improves the predictions because the small-scale features induced by the topography close to the ground are not lost after restart. This is one of the main reasons why the simulation presented in Arduini (2017) (S_{ard}) did not capture the reversal of the wind direction at noon. In domain d04, shared by all three simulations, the flow from the Megève tributary is up-valley, while in S_{vert2} the flow is down-valley towards Passy changing direction at the measurement site. The misrepresentation of the flow in the tributaries may also explain why the depth of the CAP was underestimated. A smaller import of cold air from the tributaries to the core of the valley generates a decrease in the growth rate of the CAP.

With the introduction of the improvement in vertical resolution (see Fig. 5.6c), the model was able to better represent the thermal structure of the atmosphere during the PCAP event. Note that the depth of the CAP is greater throughout the simulation, which better agrees with the observations.

Wind speed does not show striking differences from one simulation to another, although in S_{vert2} (see Fig. 5.6f) the reproduction of the upper-level jet at the end of the simulation (February 13 around noon) is better captured than in the other two simulations, see Figs. 5.6d and 5.6e, where it was triggered too soon. This simulation also better reproduced the flow acceleration during the morning of February 12 and 13, although it is not as strong as it was reported in the field data (see Fig. V.3 in Arduini, 2017).

The influence of the model restart and vertical resolution on wind direction seems to be very important near the surface. The differences between Figs. 5.6g and 5.6h show that the uninterrupted model run better reproduces wind direction with the appearance of some air blowing from the east, especially on February 12. However, the improvement in vertical resolution seems to be definitive for the improvement of wind direction. Figure 5.6i shows a clear pattern of air blowing from the east, with midday wind reversals.

The most important consequence of the improvement in the vertical resolution of the model is an increase in the wind speed coming from the tributaries, especially the wind from Megève and Chamonix is stronger than in the previous simulations (cases S_{ard} and S_{vert1}). This increase in wind speed generates a change in wind direction at the bottom of the valley (near Passy), which results in a better representation of the atmospheric dynamics during the PCAP episode.

Although the changes in thermal structure and wind speed were not dramatically appreciable from one simulation to another (not the case of wind direction), in this situation, the

good representation of the CAP is fundamental for an adequate modelling of the dispersion of pollutants in the atmosphere, especially in a stratified environment. Due to the better representation of the PCAP event in S_{vert2}, we will use the results of this last simulation in the following, unless otherwise indicated.

5.3.1.2 Numerical predictions versus measurements at air-quality stations

The purpose of this section is to assess the validity of PM_{10} predictions of the model with respect to concentration measurements at the four air-quality stations encompassed in the innermost domain. The PCAP event observed during the IOP1 led to a pollution episode with a daily averaged PM_{10} concentration at the monitoring site of Passy (located in the valley core) in excess of 50 μgr m^{-3}, which is the threshold for the European regulation (see Fig. 5.5a).

Figure 5.7 presents a comparison between the PM_{10} concentration recorded by the air quality stations located in the innermost domain and results from the numerical model. Measured PM_{10} concentrations were highest at the monitoring site in Passy, where its average during the episode (February 9-12 2015) was 74 μgr m^{-3} (see Fig. 5.7a). The PM_{10} concentration in Passy were generally higher than at the monitoring sites in Sallanches and Chamonix, located further dowstream and upstream, respectively. PM_{10} concentrations measured at the monitoring site in Marnaz, located outside the valley in a less confined area, were much lower with an average during the episode of about 30 μgr m^{-3}.

In the upstream section of the valley in Chamonix, the model captured the temporal variation of the PM_{10} concentration, but it underestimated the magnitude of the concentration throughout the simulated time period (see Fig. 5.7a). However in Chamonix the emission inventory did not adequately represent the emissions of SNAP sector 7, which may contribute, in part, to the underestimation of PM_{10} by the numerical model in this upstream valley section.

In Passy, the magnitude and temporal variation of the PM_{10} concentration during the mornings were well represented (see Fig. 5.7b). However, the model did not capture adequately the nocturnal peak. The concentration reached a maximum too early (about 4 hours early). Because the time at which the evening peak is recorded (around midnight), the increased concentration does not appear to be a response to the emission rate. We do believe that the reason why the model could not reproduce the correct time of the nocturnal peak is due to difficulties in capturing the correct wind structure during the evening in Passy, even

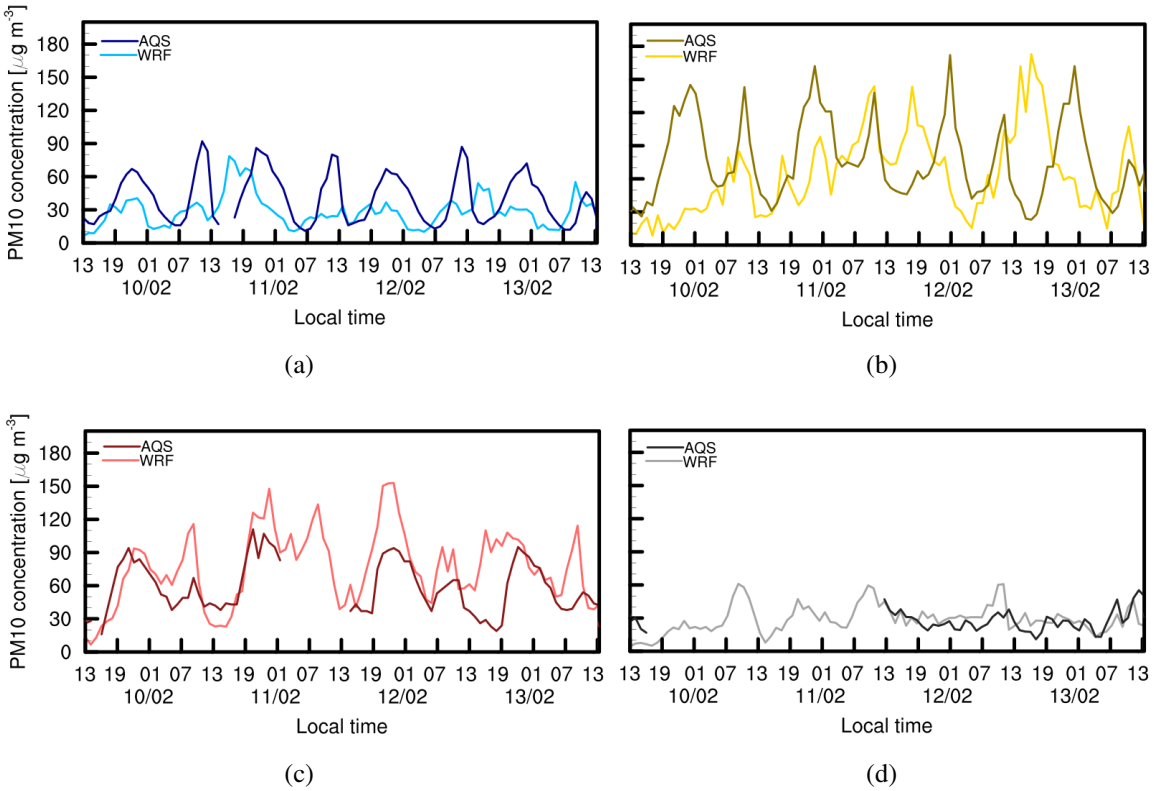

Fig. 5.7 *Time series of the concentration of PM_{10} in $\mu gr\ m^{-3}$ in Chamonix (a), Passy (b), Sallanches (c) and Marnaz (d) using data collected by the AQS (dark lines), and results of WRF innermost domain d05 (light lines). The results of the model have been averaged in time over one hour, over a horizontal domain of 1/3 km centred about each AQS and vertically over 10 m from ground level. Local time is used in all time series.*

though this is hard to confirm because of the lack of meteorological measurements in the area.

In Sallanches, the model simulates well the PM_{10} concentration observed at the monitoring site, although during the night it showed a small overestimation of the concentration (see Fig. 5.7c). In the valley core, Sallanches is the location at which the model displays the best performance.

In Marnaz, the AQS was unfortunately not functioning during the first half of the IOP. However, the model showed a good agreement with the data available for the second part of the IOP (see Fig. 5.7d). In light of these results, the performance of the model in the downstream section of the valley appears better than in the upstream section. Since the same emission inventory was used for the entire domain, this suggests that the atmospheric boundary layer is better represented in the downstream section of the valley.

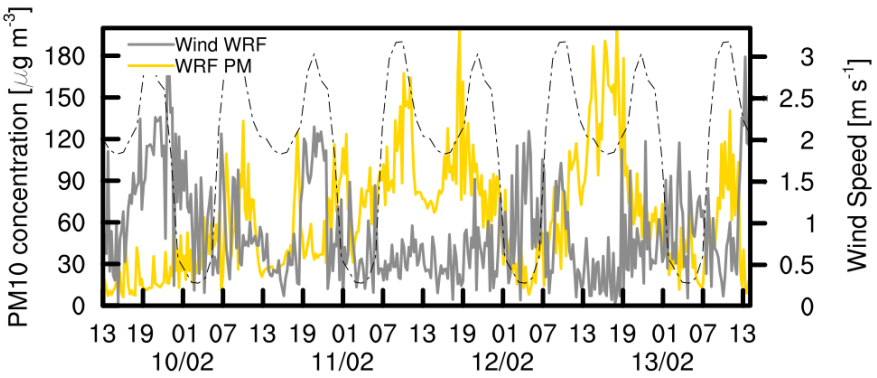

(a)

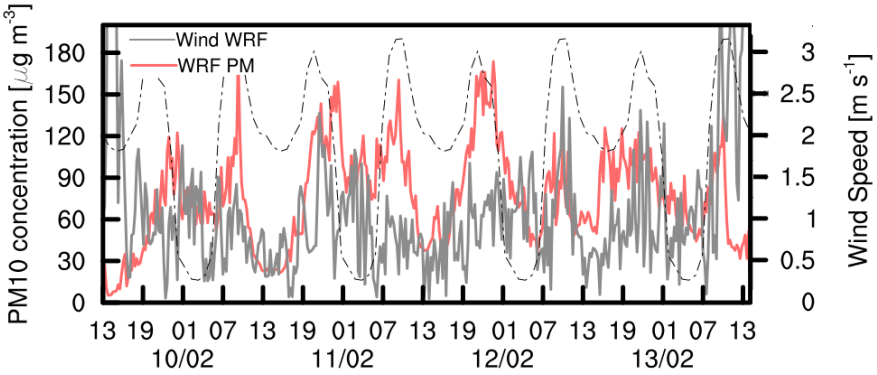

(b)

Fig. 5.8 *Time series of the concentration of PM_{10} in $\mu gr\ m^{-3}$ (color lines) and the horizontal wind speed (grey lines) using results of the simulations. The results of the model have been averaged in time over 15 minutes, over a horizontal domain of 1/3 km centred about each AQS and vertically over 10 m from ground level. Local time is used in all time series. The emission releasing profile has been added (dashed line) with no units as a reference. The calculations have been done for the positions of the AQS at Passy (a) and Sallanches (b).*

In order to understand the origin of the discrepancies between modelled and observed concentrations in Passy, we first analyse the results obtained in Sallanches, which were shown to agree well with the AQS data. In Sallanches, there is a time delay between the peaks in emission and concentration suggesting some degree of ventilation in this location and the concentration follows the emission cycle as it was observed by Chemel et al. (2016) (see Fig. 5.8b). Note that the wind speed also displays a daily cycle, with stronger winds overnight (the wind speed increases, reaches a maximum and then a quasi-steady state is reached, Quimbayo-Duarte et al., 2019a). During daylight hours the atmosphere is rather quiet with a ligther wind of less than 1 m s^{-1}. For the afternoon concentration peak, there is an increase in the emission rate in the area, but the wind speed also increases gradually and the pollution is ventilated out of the valley. Once the wind stabilizes, the emissions exceed

the ventilation capacity of the wind and PM_{10} concentration peaks. During the morning, when the emission rate increases in the area, the wind speed remains stable and actually decreases. The wind is not strong enough to disperse pollution in the atmosphere, resulting in an immediate accumulation of pollution. This is consistent with the work of Chemel et al. (2016), which showed that the signature of the daily emission cycle of the main SNAP sectors is visible in the timeseries of PM_{10} concentration (especially in the most polluted sites).

In Passy, the timeseries of PM_{10} concentration follows that of the emission rate, nonetheless the effect of the wind on the PM_{10} concentration can be observed in both Passy and Sallanches (see Fig. 5.8b). The down-valley flow is observed in the end of the afternoon at the valley bottom, and suddenly vanishes around 18h. The flow from the tributaries detached and flows over the CAP (not shown). As indicated by Sabatier et al. (2018), the flow from the east tributaries plays a very important role in the accumulation of pollution in Passy by feeding the valley core with less polluted air and generating turbulent mixing. As it is observed in Fig. 5.9, the CAP at Passy is shallower than in Sallanches suggesting that the air from Megève is able to penetrate the CAP at Sallanches resulting in a down-valley flow overnight. On the other hand, the flows from Chamonix and St-Gervais detrain above the CAP and do not contribute to the down-valley flow near the ground in Passy during the night. At Passy the flow from the eastern tributaries seems to detach too soon, leaving this section of the valley without any air supply (and without turbulent mixing) in the early hours of the night, thereby explaining that the nocturnal peak appears too early.

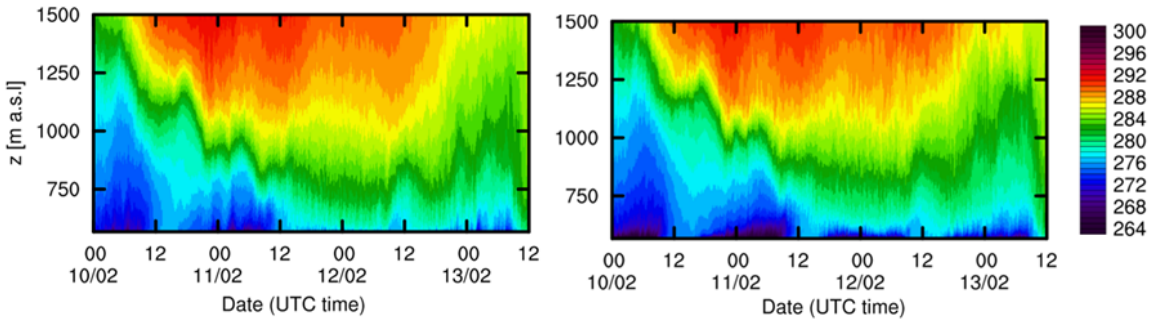

(a) (b)

Fig. 5.9 *Temporal evolution of the vertical structure of the cold-air pool in the innermost domain (d05) using data of potential temperature at Passy (a) and Sallanches (b).*

The point-to-point comparison so far showed a good reproduction of what was recorded by the radio-soundings and the LiDAR, in terms of atmospheric dynamics, and by the AQS in the area, in terms of concentration of PM_{10}. It is important to note that the differential between the AQS through the domain is conserved, being the the AQS at Passy and Sallanches

the locations reporting the highest PM_{10} concentration. The last suggest that the model is properly simulating the horizontal distribution of the pollution in the domain.

5.3.2 Horizontal Distribution of the PM_{10} Concentration

The present section describes and discusses the horizontal distribution of PM_{10} concentration across the Arve river valley, as simulated by the model. Figure 5.10 presents six-hour average of PM_{10} concentration (so as to smooth any discrepancies due to shifts in time in the model results) for different time periods during the core of the PCAP episode.

Because the emission sources are located at valley floor, PM_{10} concentrations are highest there. Note that areas marked as urban areas (black contours in Fig. 5.10) appear as hotspots of pollution. As indicated above, the daily emission cycle together with wind dynamics controls the PM_{10} concentration at the different locations.

In general, the southern tributaries of Megève and St-Gervais do not experience high levels of PM_{10}: the concentration is always below 30 μgr m^{-3}. In the east at Chamonix the situation is slightly different with localized regions where the concentration are higher than 55 μgr m^{-3} in the morning and early afternoon. Conversely, the valley core (where the towns of Passy and Sallanches are located) present important accumulations of PM_{10} throughout the whole episode with average values above 50 μgr m^{-3} and localized peak concentrations up to about 150 μgr m^{-3} around the larger urban areas in the morning and evening rush hours.

Throughout the episode, four pollution hotspots can be identified: in Passy, downstream of the monitoring station in Sallanches, upstream of the valley exit (near Magland) and on the west side of Marnaz. These locations are characterized by the presence of large emission sources (see Fig. 5.3), although not all sites reporting large sources have particularly high PM_{10} concentrations.

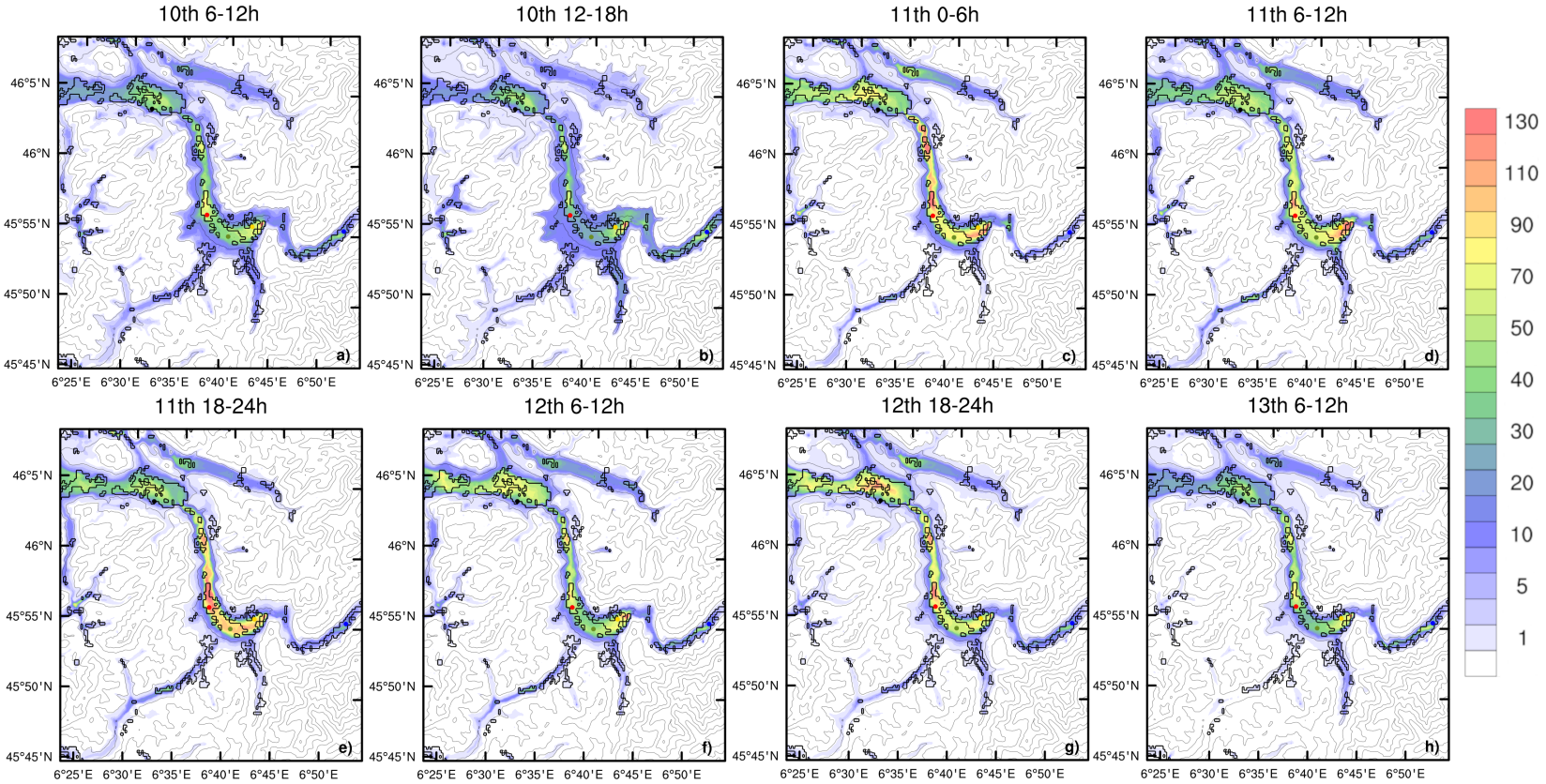

Fig. 5.10 *Contour plots of six-hour average of PM_{10} concentration [$\mu gr\ m^{-3}$] averaged along the vertical in the first 10 m above the ground overlayed with contour lines of the terrain height. Black contours indicate urban areas in the domain. The locations of the air quality stations in the zone are marked with coloured dots; Chamonix (blue), Passy (yellow), Sallanches (red) and Marnaz (black). The exact locations of the stations are documented in table 5.3. In addition, the location of the main measurement site in Passy-15 is denoted with the green dot.*

In order to better understand the horizontal distribution of PM_{10} concentrations in the domain, the valley and the emissions on it were divided into seven subsections (see Fig 5.1a). Note that we were able to devote a single variable for emissions in each of the seven valley sections, meaning that we can track the evolution in time and space of tracers emitted in each valley section. Figure 5.11a shows timeseries of the area-averaged emissions normalized to the area averaged of the total emissions (whole domain) during the simulated time period. Emissions are larger by a factor of about two in the section around Passy because the largest point source in the domain together with some other industrial sources are located in this valley section. This is likely to explain the concentration hotspot found in Passy, but not elsewhere. A more detailed analysis is performed by comparing the ratio R_{cc} (see Fig. 5.11b) between the volume averaged concentration and the area-averaged emissions for each of the valley sections. Each volume extends vertically from the ground surface to a height h = 100 m above the ground level. Given that the atmosphere is stably stratified and that emissions are released at the ground, most pollutants remain below h, as was reported for other alpine valleys during wintertime such as the Inn Valley (Gohm et al., 2009).

The values of R_{cc} shown in Fig. 5.11b must be interpreted along side the values provided for the area-averaged emissions presented in 5.11a. When R_{cc} tends to zero and the area-averaged emission is well above the mean, it may suggest that the area presents potential ventilation. On the other hand, when it tends to a value near $1/h$, the emitted mass is staying in the volume resulting in local stagnation. All lines in Fig. 5.11b, with the exception of the magenta line representing the transition section Chamonix-Passy and the blue line representing the section of Passy, follow a similar trend for most of the simulated time period. The last suggests that none of those sections experiences an atypical stagnation or ventilation regime with respect to the rest of the valley. At Passy R_{cc} remains high throughout 11th February, pointing the stagnant character of this section during the core of the PCAP episode. Even with the information provided by R_{cc}, it is hard to completely explain the origin of the horizontal distribution of PM_{10} concentration across the domain calling for an analysis of the atmospheric variables that may affect the transport of pollution.

5.3.3 Stagnation and ventilation zones in the Arve river valley

The methodology proposed by Allwine and Whiteman (1994) is used to track the potential for stagnation, recirculation or ventilation zones in the domain. The method was originally designed for a single station measurement, but in the present work, it is applied for each grid point allowing a complete picture of the potential transport to be drawn across the domain

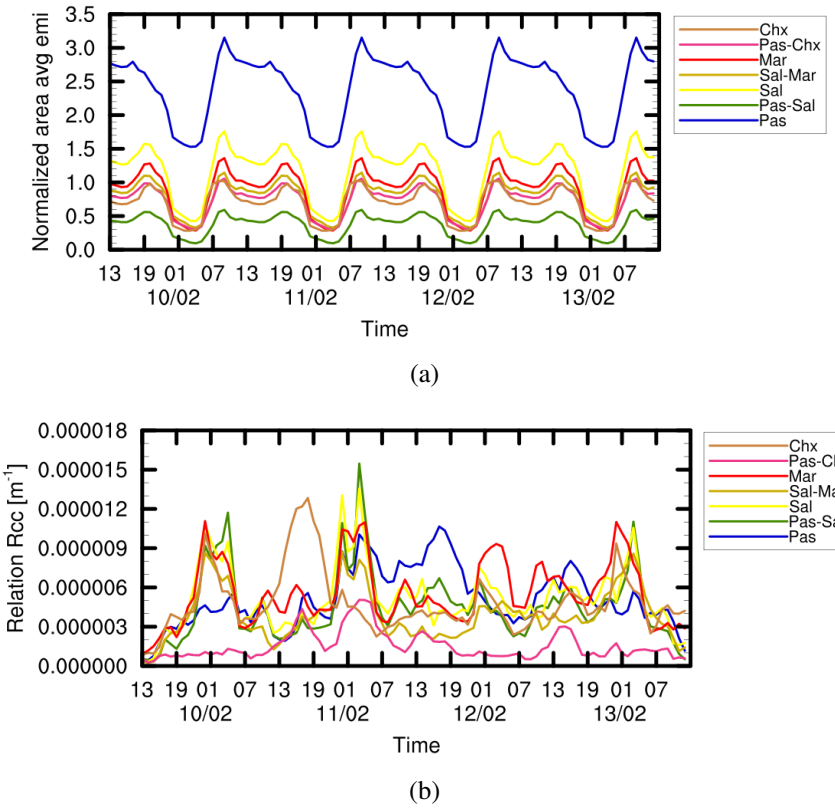

Fig. 5.11 *a) Hourly area average of the emissions released in each of the valley sections previously defined in Fig. 5.1a normalized with the area averaged emission for the whole domain. b) Time series of the ratio R_{cc} between the volume averaged concentration and the area-averaged emissions of PM_{10} for each of the valley sections (valley sections defined in Fig. 5.1a).*

(see Sect. 4.4.1 for a summary of the methodology). A characterisation of the R index and the wind run S for the winter 2014-2015 was carried out between the months of December and February using data from the Passy-15 field campaign (see Fig. 5.12). The data were obtained from the first LiDAR level (40 m a.g.l.) and averaged over different time periods τ (not shown) in order to choose the most appropriate values for the critical values of stagnation and ventilation for the recirculation index (R_c and R_{cv}) and wind run (S_c and S_{cv}). A value of τ equal to 6 hr was selected to provide a daily variability of the transport across the domain.

The critical values used in Allwine and Whiteman (1994) were defined by characterizing the transport of two sites in the Colorado Plateau basin, USA. Based on the average values for S and R in the two sites, the authors selected the critical values for stagnation and ventilation. Unfortunately, there is no standard methodology to choose such critical values; indeed, the authors note the need for the development of a methodology based on a statistical or physical approach to properly define them. For our study, due to the fact that data were only available

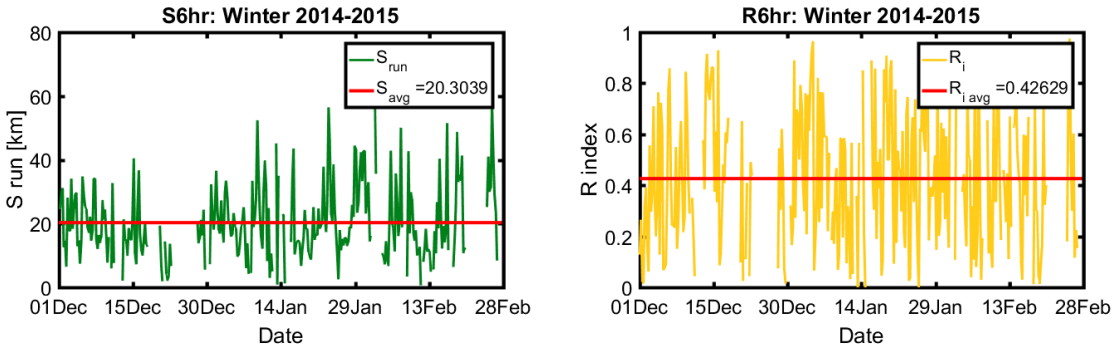

(a) (b)

Fig. 5.12 *Timeseries of the wind run S (a) and the recirculation index R (b) for the winter 2014-2015 (1st December 2015 to the 28th February 2015). Data retrieved from LiDAR measurements at the position of the IOP at 40 m a.g.l. The calculation has been done using a* τ*= 6 hr.*

at one site inside the valley, we have to base the critical values on the measurement site at Passy. In a 6-hour interval the average S_{avg} is equal to 20 km, corresponding to an average wind speed of about 0.9 m s^{-1}. As this is a light wind speed, the critical value for stagnation S_c is set equal to 20 km. The critical value for ventilation (S_{cv}) is set to 32 km using τ equal to 6 hr. This value corresponds to an average wind speed of about 1.5 m s^{-1}, which from a previous analysis of the PM_{10} time series through the winter seems to be large enough to ventilate pollution from the valley core (not shown). A priori we know that the location of Passy is poorly ventilated, which is somehow confirmed in the time series of S: just about 15% of the time, values are found above S_{cv}. On the other hand, about 60% of the time, S presents values below S_c (see Fig. 5.12a).

Since R measures the recirculation potential of an air parcel on time scales comparable with τ by relating the travelled distance S to the resultant distance L, the values of R are strongly influenced by the characteristics of the terrain. Nevertheless, the critical values R_c and R_{cv} can be seen as values independent of the characteristics of each site. Allwine and Whiteman (1994) set R=R_c when the resultant distance corresponds to 40% of the total wind run for a given time period. In the same way R=R_{cv} when the resultant distance corresponds to 80% of the total wind run for the same time period. In this work we use the values originally proposed by Allwine and Whiteman (1994), namely R_c = 0.6 and R_{cv} = 0.2.

Allwine and Whiteman (1994) defined three regimes to characterize the atmospheric transport potential for a single location: stagnation, recirculation and ventilation. These three categories do not appear to be sufficient to adequately describe our simulations and the need to include a more descriptive classification was necessary. Largeron (2010) improved the

Categorie	Criterium	Thresholds
Critical stagnation (SC)	$S \leq S_c$ and $R \geq R_c$	$S_c = 20$ km and $Rc = 0.6$
Stagnation (S)	$S \leq S_c$ and $R \leq R_c$	$S_c = 20$ km and $Rc = 0.6$
Recirculation (R)	$S \geq S_c$ and $R \geq R_c$	$S_c = 20$ km and $Rc = 0.6$
Low ventilation (LV)	$(S_c \leq S \leq S_{cv}$ and $R \leq R_c)$ or $(S \geq S_{cv}$ and $R_{cv} \leq R \leq R_c)$	$S_c = 20$ km and $Rc = 0.6$ $S_{cv} = 32$ km and $R_{cv} = 0.2$
Ventilation (V)	$S \geq S_{cv}$ and $R \leq R_{cv})$	$S_{cv} = 32$ km and $R_{cv} = 0.2$

Table 5.4 *Definition of the five categories to characterize the transport properties of the flow proposed by Largeron (2010). The critical values for the wind run have been modified to better describe the wind structure in the Arve River Valley (IOP location). The values registered herein for the critical values have been selected using a τ = 6 hr.*

classification by including two additional categories (critical stagnation and low ventilation) based on Allwine and Whiteman (1994) methodology for the Grenoble Valley. These categories, defined in Table 5.4 range from the worst case scenario for pollutant ventilation (critical stagnation) that is low wind speed combined with a strong recirculation character, to the best case scenario for which low accumulation (ventilation) is associated to high wind speeds that transports pollutants away from the measurement site.

When the domain is mapped using these categories, regions ranging from critically-stagnant zones to well-ventilated zones are identified. Starting at the south part of the domain, the Megève tributary has a strong ventilation potential. The wind from the south of the domain is channelled into the valley core through the episode (see Fig. 5.13). Part of this flow is able to penetrate the CAP at the core of the valley generating ventilation at different moments during the episode. This is evident in Sallanches where, despite its stagnant character, critical stagnation was rarely evidenced (see Figs. 5.13c, 5.13d and 5.13e). The penetration of the flow coming from the other tributary of St-Gervais and Chamonix into the CAP at the valley core is not always the case, at the section of Passy critical stagnation is found at different periods through the episode (see Fig. 5.13b for example).

A jet-like structure (not shown) is observed at the valley exit creating a local ventilation zone (Cluses, 46°4'N - 6°35'E) that remains throughout the simulation. This flow also generates a local stagnation zone in Marnaz (see Fig. 5.13e) due to a recirculation pattern created when the flow cannot follow the abrupt change in cross-sectional area between Cluses and Marnaz. Despite the stagnation zone, PM_{10} did not accumulate in Marnaz; the ventilation zone at the valley exit seems to be sufficient to prevent such accumulation.

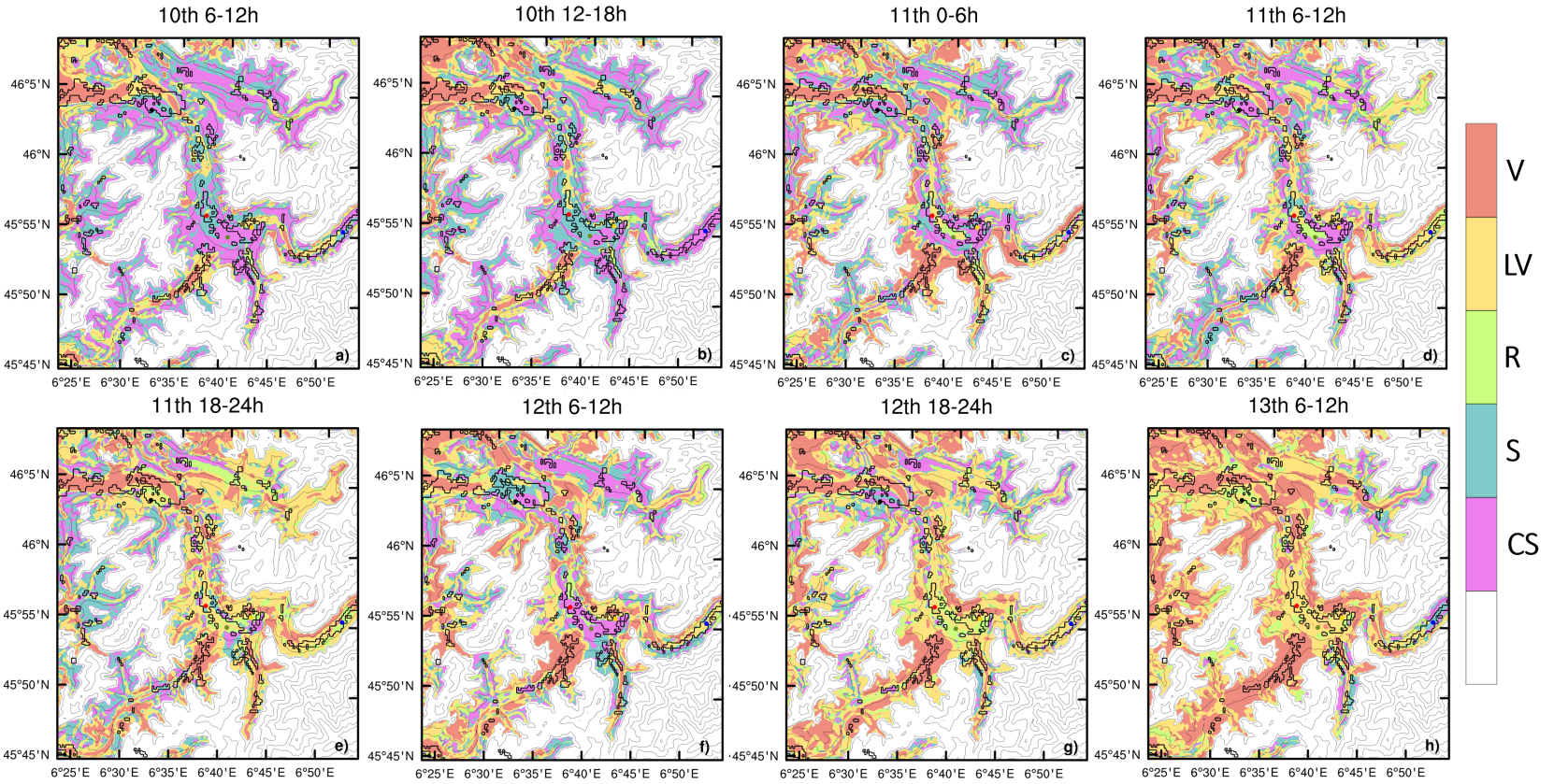

Fig. 5.13 *Maps tracking the zones prone to critical stagnation (CS), stagnation (S), recirculation (R), low ventilation (LV) and ventilation (V) using a six-hour average in time and averaged along the vertical in the first 10 m above the ground. The results have been overlayed with contour lines of the terrain height. The data is masked to show the information only for terrain height lower than 1500 m a.s.l. Black contours indicate urban areas in the domain. The locations of the air quality stations in the zone are marked with coloured dots; Chamonix (blue), Passy (yellow), Sallanches (red) and Marnaz (black). The exact locations of the stations are documented in table 5.3. In addition, the location of the main measurement site in Passy-15 is denoted with the green dot.*

The core of the valley is predominantly stagnant during the episode, although different degrees of stagnation are recorded across the valley sections. In Passy, for example, a critical stagnation is often found explaining, together with high emissions (see Fig. 5.11) the high pollution levels recorded there. This section appears to be decoupled from the rest of the valley core. In the downstream direction (near Sallanches) the conditions are slightly different showing a lower degree of stagnation and even during the first hours of the 11th February a low ventilation. This results in a significant accumulation of pollutants in the area, as observed in Sallanches, but due to some ventilation PM_{10} concentrations are not as high as in Passy.

5.3.4 Local and Non-local Contributions

The relative contributions of the PM_{10} emissions of each of the seven sections of the valley to the total PM_{10} concentration at the location of the air quality monitoring sites (Chamonix, Passy, Sallanches and Marnaz) are presented in Fig. 5.14. More precisely, Fig. 5.14 displays the ratios $< C_i >_{AQS_j} / < \Sigma C_i + Rest >_{AQS_j}$, for i comprised between 1 and 7 and j, between 1 and 4. Each index i is associated with a colour, and the same colour convention as in Fig. 5.11 is used. "Rest" represents the tracers being emitted in the innermost domain but outside the seven zones.

In the upstream section of the valley at Chamonix (see Fig. 5.14a) PM_{10} pollution is originating almost entirely from local sources throughout the episode. This result can be accounted by the fact that no source exists upstream of the Chamonix valley section and an up-valley flow, if exists, does not reach Chamonix. It agrees with a previous study by Chazette et al. (2005), which highlighted the importance of local emission sources on the concentration of wintertime pollution at this site.

Over most part of the episode the contribution of local sources emitted in Passy to the total concentration of PM_{10} recorded in Passy reaches values close to 80% with an average of 74% during the episode (see Fig. 5.14b), which highlights the decoupled character of this section of the valley during the persistant stage of the episode (11 - 13th February) pointed out in Sect. 5.3.2. Also, note that the contribution of the downstream sections is almost zero, suggesting that no up-valley flow is presented there during the episode. The only contribution of pollution to the section, although small, appears to come from Chamonix (brown line) and the tributary of St-Gervais (black line), especially at night, suggesting that part of the flow from these tributaries is able to penetrate the CAP. This suggests that, as deduced by Sabatier

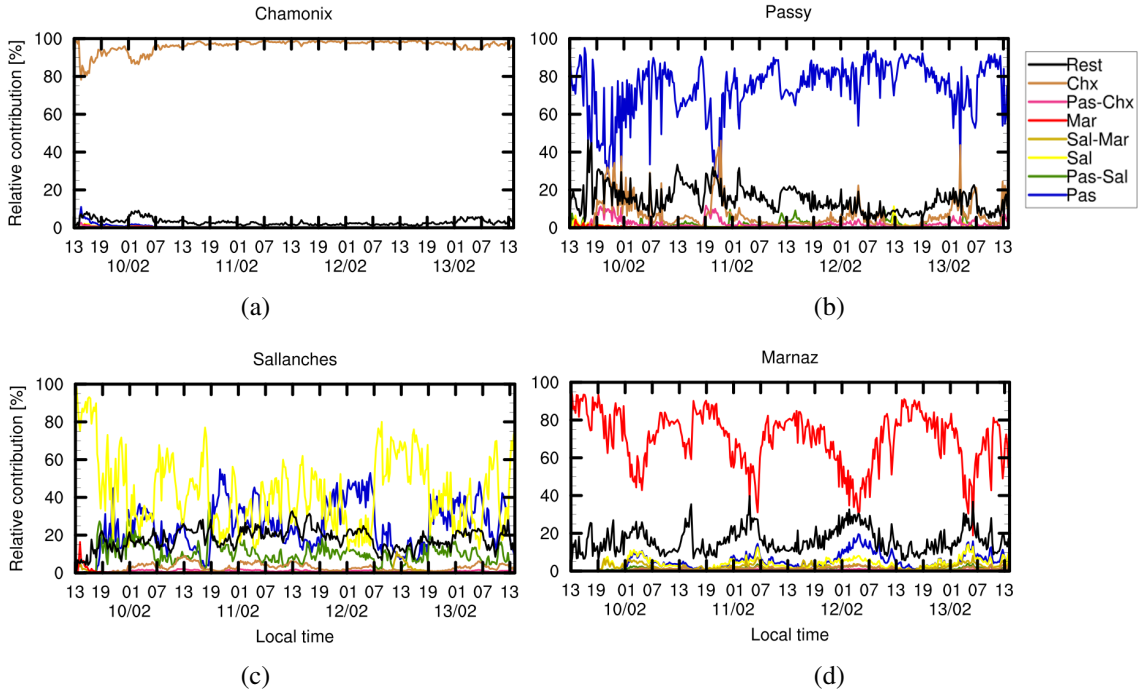

Fig. 5.14 *Timeseries of the relative contribution in percentage of each of the valley sections (see Fig. 5.1b) to the value recorded in the AQS position in Chamonix (a), Passy (b), Sallanches (c) and Marnaz (d) using the data produced in the innermost domain d05. The results of the model have been averaged in time every 15 minutesand in space over a horizontal square of side 1/3 km around the location of AQS station; an average is also performed over the first 10 m above ground level.*

et al. (2018), the tributaries can make a contribution (about an average of 15% through the episode) to the pollution recorded at Passy.

In Sallanches (see Fig. 5.14c) the situation is more complex and, in fact, this section shows strong interactions with the surroundings sections. Although the average emissions released from this section is the second largest in the domain (see Fig. 5.11a), the contribution from local sources is not as high (43%) as reported for the upstream section (74%). Again, the lack of evidence of up-valley flow during the episode is reinforced by the small contribution of the section linking Sallanches and Marnaz (always less than 10%, gold line in Fig. 5.14c). The contribution of PM_{10} emissions sources from the section in Passy is very important, with an average of 25% throughout the episode. Note that a daily cycle can be identified in the timeseries, with a large contribution from Passy during the night, while the export of pollution ceases during the day. Finally, the contribution from the tributary leading to Megève (black line) reaches values as high as 27% for short periods of time.

In Marnaz (see Fig. 5.14d) the contribution of local sources to the local PM10 pollution is as high as 70% on average during the episode. A daily cycle is also visible in the timeseries. During the night, non-local pollution increases systematically, especially from sources outside the seven sections (black line). Note that the peaks in the contribution of the latter sources match very well with the peaks of the upstream sources, suggesting that these sources are located in the upstream part of the valley.

5.4 Conclusions and Discussion

A real-case simulation of the particulate-matter transport processes in a section of the Arve River valley (northern French Alps) is performed using the Weather Research and Forecasting (WRF) model. The influence of the valley-wind system on the ventilation of pollutants and the effect of very local pollution sources on the resultant pollutant concentration in such a deep alpine valley when subject to wintertime anticyclonic conditions was quantified. The results about the flow dynamics presented here are based on a previous work developed by Arduini (2017). The simulations reproduce the pollution episode associated with the first intensive observation period (IOP) of the Passy-15 field-campaign (Staquet et al., 2015, Paci et al., 2017) which was conducted in the surroundings of the town of Passy during the second week of February 2015. The set of numerical simulations used was able to adequately describe the main features of the atmospheric boundary layer (thermal structure, wind speed, wind direction, i.a.) observed in the area during those days. The model's ability to accurately simulate the concentration of PM_{10} in the valley has been tested against data recorded by four air quality stations (AQS) in the area (Chamonix, Passy, Sallanches and Marnaz, see Fig. 5.1). An analysis was then developed to account for the horizontal distribution of pollution in the valley from the point of view of the emission sources and the atmospheric dynamics. The main results of this study are summarized as follows:

- A sensitivity test was conducted by running the simulation continuously for four days of the IOP and by improving the vertical resolution close to the ground, with the first mass point at 4.6 m above the ground level (m a.g.l.) and the double of grid points in the first 200 m a.g.l. (17 grid points in the first 200 m a.g.l.). Such modifications had an important effect on the results, namely they led to a better characterization of the atmospheric boundary layer in the domain and therefore a better representation of the CAP in the core of the valley. A comparison has been made between the results of the model and the data collected in the Passy field campaign (data retrieved from the

radiosoundings and the wind profilers). A better characterization of the wind led to a better representation of the CAP in the core of the valley, having a continuous flow of cold air from the tributaries that feed the CAP, increasing its growth rate compared to the base simulation of Arduini (2017).

- The model performance was evaluated by comparing the simulated concentration of PM_{10} in the domain with data recorded by the air quality stations (AQS) in the area. The simulated concentration of PM_{10} at the Sallanches and Marnaz AQS locations showed better agreement with the data collected by the AQS than the simulated concentration of PM_{10} at the Chamonix and Passy AQS locations. However, through the domain, the correct magnitude of the concentration was well captured (see Fig. 5.7). The main discrepancy occurred in Passy, where the simulated PM_{10} appeared to peak too early in the evening compared to the AQS data (about four hours earlier). Because of the time at which the AQS reports those peaks (around midnight), it seems that this discrepancy is not a consequence of the release of emissions but, on the contrary, it seems to be a consequence of the dynamic characteristics of the atmosphere at Passy. The tributaries in the area partly drive the growth of the CAP; in fact, the air coming from Megève appears to control the dynamics of the CAP in Sallanches (this is extensively discussed in Arduini, 2017). Problems with the timing of the concentration of PM_{10} at Passy can be explained by an intrusion of cold air from the tributary of Chamonix that accelerates the flow at this site too early (see Fig. 5.8a) generating the early ventilation observed in the simulations. The origin of this problem can be attributed to the unsuccessful simulation of a stronger CAP. In the real situation, the air from Chamonix cannot flow into the strong CAP and is forced to flow over it. Before sunrise, the air coming from the Megève's tributary responds with a similar behaviour, which causes poor ventilation of the valley's core. A better characterization of the terrain characteristics, as the urban canopy in urbanized areas (Rasheed et al., 2011, Rendón et al., 2014), the ice and fog formation processes (Engerer et al., 2008), or the cloud microphysics effects (Neemann et al., 2015) may help to obtain a better description of the CAP in Passy that strongly affect the representation of the temporal evolution of the PM_{10} concentration.

- From the measurements of the AQS available across the valley, an unusual horizontal distribution of pollution was observed, with hotspots of PM_{10} concentration in localized sites throughout the valley core. These sites prone to high PM_{10} pollution are normally associated with urban areas (See Fig. 5.10). To understand the distribution of pollutants in the domain we divided the valley into seven sections (see Fig. 5.1b), which allow

us to track the evolution in time and space of pollutants released in each of the valley section. The section with the highest amount of released pollution is that of Passy, even so, this cannot completely explain the high concentration of pollutants there. The sections of Sallanches and Marnaz emit a similar amount of pollution during the episode, although in Sallanches there is a much higher concentration of PM_{10} than in Marnaz. This difference cannot be explained only from the point of view of emissions, rising the need to estimate the ventilation potential in the domain.

- Following the methodology developed by Allwine and Whiteman (1994), zones prone to ventilation and stagnation in the domain were characterized (see Fig. 5.13). A relationship was identified between these zones, their respective emission sources and the zones liable to high pollution. In Passy, for example, critical stagnation is often found due to the fact that it remains decoupled from the rest of the valley core. The air from the Chamonix and St-Gervais tributaries detach and flow over the CAP without injecting less polluted air into the valley core (thereby not inducing any mixing process in this CAP). On the other hand, the air from Megève can flow into the CAP but goes down-valley towards Sallanches, leaving the section in Passy uncoupled from the rest of the valley, which creates a stagnation zone. Such stagnation zone along with the fact that this area presents the highest emission of all the valley sections, results in the high concentration of PM_{10} recorded in the area. Conclusions from chapter 4 confirmed the fact that a stagnant zone is not necessary associated with high pollution, which in this real case was observed in the north of the domain (Morillon, 46°05'N, 6°40'E) because no significant emission occurs there.

- The local and non-local contribution to the concentration of PM_{10} in the different sections of the valley has been identified. In Passy, which through the analysis stands out as the location with the highest emissions, showing the greatest problems of atmospheric stagnation and particulate air pollution, the most important factor contributing to the pollution reported at the AQS site was the local sources. The decoupled character of the area and the large emissions become a dangerous combination. In Sallanches, on the other hand, the impact of external sources (such as tributaries and Passy's pollution) play an important role in the problem by reporting a very similar contribution to local sources. From this study, it is clear that there is almost no transport in the upstream direction through the episode. Indeed no section of the valley seems to be affected by pollution released in a neighbouring downstream section suggesting no up-valley transport during the episode.

As a final consideration, it is important to note that the analysis presented in this paper is based entirely on a single winter and especially on a one-week pollution episode. Although the results of the Passy-15 field campaign and the works exploring those results (including the one presented here) provide valuable information on the drivers of particulate air pollution in the valley, the need for long-term meteorological and pollutant measurements in the area to better understand what is leading to such pollution problems is clear.

Acknowledgements

The PhD work of J. Quimbayo is supported by the Colombian Administrative Department of Science, Technology and Innovation (COLCIENCIAS). Numerical simulations were run on the ARCHER UK National Supercomputing Service (http://www.archer.ac.uk).

Chapter 6

Summary and General Conclusions

The purpose of this thesis is to study the drivers of particulate air pollution in deep Alpine valleys during winter in decoupled atmospheric conditions. The work has been conducted using numerical simulations of both idealized and real cases using the Weather Research and Forecasting (WRF) model. Passive tracers have been used to emulate pollution sources, assuming a low reactivity of PM_{10} in the Alps in winter conditions. The work is designed to meet the objectives outlined at the end of Chap. 1, namely to improve the understanding of pollution transport in the stable valley boundary layer. The most important conclusions from this work are now presented and discussed.

Starting with a simple idealized case, a three-dimensional U-shaped valley that opens directly onto a plain is considered (see Chap. 3). The objective is to characterize the response of the pollution released over the valley bottom to the nocturnal valley wind system (focusing on the down-valley wind dynamics) with no synoptic forcing. The change in the thermal structure of the atmosphere within the valley (because of the convergence of the down-slope flow at the valley centre) generates a horizontal pressure gradient between that valley and the plain, which leads to the development of a down-valley flow. After about 180 minutes into the simulation, the down-valley flow is fully developed and reaches a quasi-steady state regime. The down-valley flow next displays oscillations induced by internal gravity waves emitted by the down-slope wind when hitting the valley floor (and later its level of neutral buoyancy) via a hydraulic jump (as observed in Chemel et al., 2009b). The down valley flow velocity evolves linearly along the valley axis, starting from zero at the beginning of the valley to a maximum velocity of about 3 m s^{-1} at the valley exit. The down-valley flow displays weak turbulence due to the stable stratification that prevents mixing. Indeed,

turbulence is detected in two regions only: close to the valley floor, within a shallow layer ($\simeq$ 20 m) extending from the ground to the first maximum of this wind, which behaves like a jet; and at the top of the cold-air pool close to the valley exit, where the wind accelerates because of the decreasing height of the cold-air pool (see Fig. 3.7).

Passive tracers are emitted at the beginning of the steady regime. Several striking features should be noted. The tracers emitted at the ground remain trapped at all times inside the shallow layer extending up to the jet speed maximum as can be inferred from the conservation of the tracer flux and the linear behaviour of the along-valley flow versus y. As a consequence, and because the flow is laminar elsewhere (except in the second region detected close to the valley exit), tracers emitted above that bottom layer at different altitudes are advected towards the valley exit but do not meet. For the tracers emitted at the ground level, the averaged concentration over the trapping region close to the ground (outside its emission zone) displays a decaying law along the valley axis. The concentration thus decreases as $1/y$ at a given time, where y is the along-valley coordinate. As a consequence, the total concentration at the valley exit, where several valley-floor emissions superimpose, may not be larger than inside the valley close to an emission source. Finally, the tracer's average concentration displays strong temporal oscillations, induced by those detected in the down-valley wind, which may reach 50% of the mean (over time) value of the concentration. If occurring in a real valley, this would imply that averaged values in an urbanized valley may disguise high instantaneous, and therefore potentially harmful, pollution concentration values.

In Chap 4, a more complex situation is considered as a step towards a more realistic configuration. A valley composed of a first valley section that opens on a narrow valley section that finally opens on a plain is used to examine the response of orographic variations along the valley axis on the ventilation of pollutants inside the valley during wintertime. Two setups were considered, named $P1$ and $P2$, having the same downstream valley section, but a different upstream valley section, its width being three times larger in $P1$ than $P2$ (see Fig. 4.1).

The pressure gradient created by differences in the thermal structure of the atmosphere between the valley core and the plain is also observed in this case, although due to variations in the width of the valley floor an intra-valley pressure gradient is also observed. As a result, the along-valley wind experiences a different behaviour compared with the one previously observed in the simple valley-plain configuration. For $P1$, an up-valley wind is observed near the end of the upstream section of the valley during the first three hours of simulation, then

reversing in the downstream direction for the remainder of the simulated time period (see Fig. 4.2a). For $P2$ a this up-valley wind persists until the end of the simulated period (see Fig. 4.2c). Such differences in the wind dynamics between $P1$ and $P2$ translate into differences in horizontal mass flux outside the upstream section of the valley: this mass flux is 1.5 times greater for $P1$ than for $P2$ (see Fig. 4.3). From this result, the effect of the change in the width of the valley floor on the transport processes in the system is already observed, and a deeper analysis was conducted to better characterize this effect.

The ventilation potential across the domain was evaluated using the methodology proposed by Allwine and Whiteman (1994) to predict locations prone to ventilation, stagnation and recirculation. The methodology was found to work well for predicting areas with high tracer concentration; indeed, the zones where a critical stagnation was detected agree well with zones of high tracer concentration (see Fig. 4.9). However, the relationship between areas identified as prone to stagnation and the zones of high tracer concentration should be considered with caution since the variability in the concentration of air pollutants is not only a function of atmospheric dynamics but also of the emission location and rate, as evidenced in Fig. 4.9d.

Although the methodology of Allwine and Whiteman (1994) provided a good overview of the ventilation potential in the domain, a more quantitative approach was used to characterize the transport properties of each of the sections composing the valley. As noted above, the change in the valley-floor width between the upstream ($\mathscr{U}$) and downstream ($\mathscr{D}$) valley sections affects the atmospheric dynamics, and hence tracer transport across the domain. The export of tracers out of $\mathscr{U}$ is reduced by about 50% for $P2$ compared to that for $P1$. Intra-valley transport of tracers is also reduced in $\mathscr{D}$. By the end of the simulated period about 80% of the total mass emitted for tracer $TrP1_4$ (released at the beginning of $\mathscr{D}$) has been transported out of the valley system while for tracer $TrP2_4$ (which is released at the same position but for $P2$) only about 40% of the total mass emitted have left the valley (see Figs. 4.10c and 4.10g).

A final analysis is performed with the introduction of the residence time, a quantification of the ventilation efficiency within the different sections of the valley. For $P1$ the residence time within $\mathscr{U}$ (about two hours) is more than twice that within $\mathscr{D}$ (about 45 minutes) at the end of the simulated time period (Fig. 4.11). This difference in the ventilation efficiency between $\mathscr{U}$ and $\mathscr{D}$ is more pronounced for $P2$, for which the ventilation efficiency for $\mathscr{U}$ (about 10 hours) is reduced by more than a factor ten compared to that for $\mathscr{D}$ (about 45 minutes). From this analysis it is important to note that although the upstream valley section

of $P2$ may be considered as a trapper valley (Arduini et al., 2017), the valley as a whole could not be considered as a trapper due to the strong ventilation evidenced in $\mathscr{D}$.

A real-case is eventually considered in Chap. 5 by simulating the particulate-matter transport processes in a section of the Arve River valley (northern French Alps). The influence of the valley-wind system on the ventilation of pollutants and the effect of very local pollution sources on the resultant pollutant concentration in such a deep alpine valley when subject to wintertime anticyclonic conditions was quantified. The results about the flow dynamics presented here are based on a previous work developed by Arduini (2017). The simulations reproduce the pollution episode associated with the first intensive observation period (IOP) of the Passy-15 field-campaign (Staquet et al., 2015, Paci et al., 2017) which was conducted in the Arve River valley during the second week of February 2015. The set of numerical simulations used was able to adequately describe the main features of the atmospheric boundary layer (thermal structure, wind speed, wind direction, i.a.) observed in the area during those days.

A sensitivity test was conducted by running the simulation continuously for four days of the IOP and by improving the vertical resolution close to the ground, with the first mass point at 4.6 m above the ground level (m a.g.l.) and the double of grid points in the first 200 m a.b.l. (17 grid points in the first 200 m a.g.l.). Such modifications had an important effect on the results, namely to a better characterization of the atmospheric boundary layer in the domain and therefore a better representation of the CAP in the core of the valley. A comparison has been made between the results of the model and the data collected in the Passy field campaign (data retrieved from the radiosoundings and the wind profilers). The model showed good performance in reproducing the temporal evolution of the vertical potential temperature profiles during the first IOP, implying that the continuous flow of cold air from the tributaries contributing to the increase of the CAP's growth is better simulated than in Arduini (2017).

In a second step, the performance of the model was evaluated by comparing the simulated concentration of PM_{10} in the domain with data recorded by the air quality stations (AQS) in the area. The simulated concentration of PM_{10} at the Sallanches and Marnaz AQS locations showed better agreement with the data collected by the AQS than the simulated concentration of PM_{10} at the Chamonix and Passy AQS locations. However, through the domain, the correct magnitude of the concentration was always captured (see Fig. 5.7). The main discrepancy occurred in Passy, where the simulated PM_{10} appeared to peak too early in the evening compared to the AQS data (about four hours earlier). Because of the time at which the AQS reports those peaks (around midnight), it seems that this discrepancy is not a consequence of

the release of emissions but, on the contrary, it seems to be a consequence of the dynamic characteristics of the atmosphere at Passy. The tributaries in the area partly drive the growth of the CAP; in fact, the air coming from Megève appears to control the dynamics of the CAP in Sallanches (this is extensively discussed in Arduini, 2017). Problems with the timing of the concentration of PM_{10} at Passy can be explained by an intrusion of cold air from the tributary of Chamonix that accelerates the flow at this site too early (see Fig. 5.8a) generating the early ventilation observed in the simulations. The origin of this problem can be attributed to the unsuccessful simulation of a stronger CAP. In the real situation, the air from Chamonix cannot flow into the strong CAP and is forced to flow over it. Before sunrise, the air coming from the Megève's tributary responds with a similar behaviour, which causes poor ventilation of the valley's core.

The unusual horizontal distribution of pollution observed in this section of the Arve River valley, with several concentration hotspots of PM_{10} around the domain, has been investigated. The sites prone to high pollution are normally associated with urban areas, although an urban area may not be always associated with high pollution concentration (See Fig. 5.10). To understand the particular distribution of pollutants in the domain, the valley core was divided into seven sections (see Fig. 5.1b); this allow us to track the evolution in time and space of pollutants released in each of the valley sections. The section with the highest emissions is Passy, but the role of transport processes in the atmosphere should be also considered to understand the high pollution concentration recorded there. The sections of Sallanches and Marnaz display a similar amount of emissions during the episode, yet the AQS in Sallanches recorded a much higher concentration of PM_{10} than in Marnaz. This difference cannot be explained only from the point of view of emissions, rising the need to estimate the ventilation potential in the domain.

In this real configuration the methodology proposed by Allwine and Whiteman (1994) was also used to track the areas prone to ventilation and stagnation in the domain (see Fig. 5.13). A relationship was identified between these areas, their respective emission sources and the areas liable to high pollution. In Passy, for example, critical stagnation is often found due to the fact that this section remains decoupled from the rest of the valley. The air from the Chamonix and St-Gervais tributaries detach and flow over the CAP without injecting less polluted air into the valley core (thereby not inducing any mixing process in this CAP). On the other hand, the air from Megève can flow into the CAP but goes down-valley towards Sallanches, leaving the section in Passy uncoupled from the rest of the valley, which creates a stagnation zone. Such stagnation zone along with the fact that this area presents the highest emission of all the valley sections, results in the high concentration of PM_{10} recorded in the

area. Conclusions from chapter 4 highlighted the fact that a stagnant zone is not necessary associated with high pollution, which in this real case was observed in the north of the domain (Morillon, 46°05'N, 6°40'E) because no significant emission occurs there.

Lastly, the local and non-local contribution to the concentration of PM_{10} in the different sections of the valley has been identified. In Passy, which through the analysis stands out as the location with the highest emissions, showing the greatest problems of atmospheric stagnation and particulate air pollution, the most important factor contributing to the pollution reported at the AQS site was the local sources. The decoupled character of the area and the large emissions become a dangerous combination. In Sallanches, on the other hand, the impact of external sources (such as tributaries and Passy) play an important role in the problem, as they show a similar contribution to that of local sources (see Fig. 5.14c). Let us note finally that, from this study, it is clear that there is almost no transport in the upstream direction through the episode. Indeed no section of the valley seems to be affected by pollution released in a neighbouring downstream section suggesting no up-valley transport during the episode.

6.1 Prospectives

Although the transport and accumulation of pollutants in mountainous terrain is a very complex problem in which much remains to be learned, this thesis has helped to characterize the effects of the valley-wind system (from a fairly simple idealized system to a highly complex one) on the ventilation of pollution from deep alpine valleys. In the following some ideas for future research are presented, based on the conclusions and limitations of this document.

From the set of idealized simulations reported in Chapters 3 and 4, a clear influence of topographic characteristics on the transport and accumulation of pollutants in complex terrains can be observed. Indeed, the influence of the surrounding terrain has put forward an important change in the transport of tracers released at the ground level (by comparing the configurations used in Chap. 3 and Chap. 4). However, mountain valleys do not consist in systems of isolated valleys and plains, which highlights the need for a more complex configuration to be simulated, such as a valley system with tributaries. It may allow a better understanding of the effect of the (isolated) valley-wind system on the transport of pollutants across mountainous terrain. By slowly increasing the complexity of the system,

advantages appear such as recognizing the individual effects of each variable in a more complex real system. The latter can help to the design of sub-grid scale parametrizations with the aim to improve meso-scale modelling, to better forecast the transport processes in the atmosphere for operational applications. From the point of view of emissions, a more realistic (but still idealized) emission input can help to easily extrapolate the results of these simple configurations to real case applications. A temporal disaggregation of emissions mimicking a realistic profile may help to identify the joint effect of emissions and evening and/or morning transition on the resulting concentration.

Results obtained from the sensitivity test performed in Chap. 5 stressed the importance of continuously running the model along with the increase the vertical resolution close to the ground to accurately simulate the atmospheric dynamics and pollutant transport in such complex terrain; nonetheless, the simulations still need to be refined again. A better characterization of the particularities of the terrain, such as the urban canopy in urbanized areas (Rasheed et al., 2011, Rendón et al., 2014), the ice and fog formation processes (Engerer et al., 2008), or the cloud microphysics effects (Neemann et al., 2015) may help to obtain a better description of the CAP in Passy that strongly affect the representation of the temporal evolution of the PM_{10} concentration.

Finally, although the model was able to reproduce the main features of the atmospheric boundary layer when tested against the data collected during the field campaign, more detailed observations (meteorological and air pollution) are still required to better understand the transport processes in the atmosphere and adequately validate the numerical simulations in such a complex terrain.

References

A. S. Ackerman, O. Toon, D. Stevens, A. Heymsfield, V. Ramanathan, and E. Welton. Reduction of tropical cloudiness by soot. *Science*, 288(5468):1042–1047, 2000.

L. Y. Alleman, L. Lamaison, E. Perdrix, A. Robache, and J.-C. Galloo. Pm10 metal concentrations and source identification using positive matrix factorization and wind sectoring in a french industrial zone. *Atmospheric Research*, 96(4):612–625, 2010.

K. Allwine and C. Whiteman. Ventilation of pollutants trapped in valleys: a simple parameterization for regional-scale dispersion models. *Atmospheric Environment (1967)*, 22(9): 1839–1845, 1988.

K. J. Allwine and C. D. Whiteman. Single-station integral measures of atmospheric stagnation, recirculation and ventilation. *Atmospheric Environment*, 28(4):713–721, 1994.

J. O. Anderson, J. G. Thundiyil, and A. Stolbach. Clearing the air: A review of the effects of particulate matter air pollution on human health. *Journal of Medical Toxicology*, 8(2): 166–175, Jun 2012a.

J. O. Anderson, J. G. Thundiyil, and A. Stolbach. Clearing the air: a review of the effects of particulate matter air pollution on human health. *Journal of Medical Toxicology*, 8(2): 166–175, 2012b.

S. Anquetin, C. Guilbaud, and J.-P. Chollet. The formation and destruction of inversion layers within a deep valley. *Journal of Applied Meteorology*, 37(12):1547–1560, 1998.

S. Anquetin, C. Guilbaud, and J.-P. Chollet. Thermal valley inversion impact on the dispersion of a passive pollutant in a complex mountainous area. *Atmos. Environ.*, 33(24):3953–3959, 1999.

G. Arduini. *Wintertime stable boundary-layer processes in Alpine valleys*. PhD thesis, University of Hertfordshire, 2017.

G. Arduini, C. Staquet, and C. Chemel. Interactions between the nighttime valley-wind system and a developing cold-air pool. *Boundary-Layer Meteorol.*, 161(1):49–72, 2016.

G. Arduini, C. Chemel, and C. Staquet. Energetics of deep alpine valleys in pooling and draining configurations. *J. Atmos. Sci.*, 74 (7):2105–2124, 2017.

B. Atkinson and A. Shahub. Orographic and stability effects on day-time, valley-side slope flows. *Boundary-Layer Meteorology*, 68(3):275–300, 1994.

Atmo-Auvergne-Rhone-Alpes. Méthode d'élaboration de l'inventaire des émissions atmospheriques en auvergne-rhône-alpes. Technical report, Atmo-Auvergne-Rhone-Alpes, 2017.

Atmo-Auvergne-Rhone-Alpes. Bilan des connaissances sur la qualité de l'air dans la vallée de l'arve. Technical report, Atmo-Auvergne-Rhone-Alpes, 2018.

E. L. Avol, W. J. Gauderman, S. M. Tan, S. J. London, and J. M. Peters. Respiratory effects of relocating to areas of differing air pollution levels. *American journal of respiratory and critical care medicine*, 164(11):2067–2072, 2001.

G. Aymoz, J. L. Jaffrezo, D. Chapuis, J. Cozic, and W. Maenhaut. Seasonal variation of pm_{10} main constituents in two valleys of the french alps. i: Ec/oc fractions. *Atmospheric Chemistry and Physics*, 7(3):661–675, 2007. doi: 10.5194/acp-7-661-2007. URL https://www.atmos-chem-phys.net/7/661/2007/.

M. Baasandorj, S. W. Hoch, R. Bares, J. C. Lin, S. S. Brown, D. B. Millet, R. Martin, K. Kelly, K. J. Zarzana, C. D. Whiteman, et al. Coupling between chemical and meteorological processes under persistent cold-air pool conditions: Evolution of wintertime pm2. 5 pollution events and n2o5 observations in utah's salt lake valley. *Environmental Science & Technology*, 51(11):5941–5950, 2017.

D. C. Bader and T. B. McKee. Effects of shear, stability and valley characteristics on the destruction of temperature inversions. *Journal of climate and applied meteorology*, 24(8): 822–832, 1985.

R. M. Banta, Y. L. Pichugina, and R. K. Newsom. Relationship between low-level jet properties and turbulence kinetic energy in the nocturnal stable boundary layer. *J. Atmos. Sci.*, 60(20):2549–2555, 2003.

M. L. Bell, D. L. Davis, and T. Fletcher. A retrospective assessment of mortality from the london smog episode of 1952: the role of influenza and pollution. *Environmental health perspectives*, 112(1):6, 2004.

M. Beychok. *Fundamentals of stack gas dipersion*. M.R. Beychok ed., 2005.

T. C. Bond, S. J. Doherty, D. Fahey, P. Forster, T. Berntsen, B. DeAngelo, M. Flanner, S. Ghan, B. Kärcher, D. Koch, et al. Bounding the role of black carbon in the climate system: A scientific assessment. *Journal of Geophysical Research: Atmospheres*, 118(11): 5380–5552, 2013.

G. Brulfert, C. Chemel, E. Chaxel, and J. Chollet. Modelling photochemistry in alpine valleys. *Atmos. Chem. Phys.*, 5(9):2341–2355, 2005.

P. Burns and C. Chemel. Evolution of cold-air-pooling processes in complex terrain. *Boundary-Layer Meteorol.*, 150(3):423–447, 2014.

P. Burns and C. Chemel. Interactions between downslope flows and a developing cold-air pool. *Boundary-Layer Meteorology*, 154(1):57–80, 2015.

F. Catalano and A. Cenedese. High-resolution numerical modeling of thermally driven slope winds in a valley with strong capping. *Journal of Applied Meteorology and Climatology*, 49(9):1859–1880, 2010.

P. Chazette, P. Couvert, H. Randriamiarisoa, J. Sanak, B. Bonsang, P. Moral, S. Berthier, S. Salanave, and F. Toussaint. Three-dimensional survey of pollution during winter in french alps valleys. *AE*, 39(6):1035–1047, 2005.

C. Chemel and P. Burns. Pollutant dispersion in a developing valley cold-air pool. *Boundary-Layer Meteorol.*, 154(3):391–408, 2015.

C. Chemel, C. Staquet, and Y. Largeron. Generation of internal gravity waves by a katabatic wind in an idealized alpine valley. *Meteorology and atmospheric physics*, 103(1-4): 187–194, 2009a.

C. Chemel, C. Staquet, and Y. Largeron. Generation of internal gravity waves by a katabatic wind in an idealized alpine valley. *Meteorol. Atmos. Phys.*, 103(1-4):187–194, 2009b.

C. Chemel, G. Arduini, C. Staquet, Y. Largeron, D. Legain, D. Tzanos, and A. Paci. Valley heat deficit as a bulk measure of wintertime particulate air pollution in the arve river valley. *Atmos. Environ.*, 128:208–215, 2016.

F. Chen and J. Dudhia. Coupling an advanced land surface–hydrology model with the penn state–ncar mm5 modeling system. part i: Model implementation and sensitivity. *Mon. Weather. Rev.*, 129(4):569–585, 2001.

F. Chevrier, G. Močnik, I. Ježek, G. Brulfert, J.-L. Jaffrezo, and J.-L. Besombes. Decombio-contribution de la combustion de la biomasse aux pm. *POLLUTION ATMOSPHÉRIQUE*, (231-232):259, 2016.

H. M. Chew and W. Kellaway. *London Assize of Nuisance, 1301-1431: a calendar*, volume 10. London Record Society, 1973.

W. G. Christy. History of the air pollution control association. *Journal of the Air Pollution Control Association*, 10(2):126–174, 1960.

A. Colette, F. K. Chow, and R. L. Street. A numerical study of inversion-layer breakup and the effects of topographic shading in idealized valleys. *Journal of Applied Meteorology*, 42(9):1255–1272, 2003.

J. Cuxart and M. Jiménez. Mixing processes in a nocturnal low-level jet: An les study. *J. Atmos. Sci.*, 64(5):1666–1679, 2007.

J. Cuxart, M. Jiménez, and D. Martínez. Nocturnal meso-beta basin and katabatic flows on a midlatitude island. *Monthly weather review*, 135(3):918–932, 2007.

S. F. De Wekker. Observational and numerical evidence of depressed convective boundary layer heights near a mountain base. *Journal of Applied Meteorology and Climatology*, 47 (4):1017–1026, 2008.

J. W. Deardorff. Stratocumulus-capped mixed layers derived from a three-dimensional model. *Boundary-Layer Meteorol.*, 18(4):495–527, 1980.

F. Defant. Zur theorie der hangwinde, nebst bemerkungen zur theorie der berg- und talwinde (A Theory of Slope Winds, Along with Remarks on the Theory of Mountain Winds and Valley Winds). *Springer-Verlag Publishing Company, Vienna, Austria.*, 1949.

H. A. T. DIRECTIVE. Council directive 1999/30/ec. *Official Journal L*, 163(29/06):0041–0060, 1999.

H. A. T. DIRECTIVE. Council directive 1999/30/ec. *Official Journal L*, 163(20/08):0041–0060, 2015.

F. Dominici, R. D. Peng, M. L. Bell, L. Pham, A. McDermott, S. L. Zeger, and J. M. Samet. Fine particulate air pollution and hospital admission for cardiovascular and respiratory diseases. *Jama*, 295(10):1127–1134, 2006.

J. Doran and T. Horst. Velocity and temperature oscillations in drainage winds. *Journal of Applied Meteorology*, 20(4):361–364, 1981.

P. Drazin and W. Reid. *Hydrodynamic stability*. Cambridge University Press, 1982.

J. Dudhia. Numerical study of convection observed during the winter monsoon experiment using a mesoscale two-dimensional model. *J. Atmos. Sci.*, 46:3077–3107, 1989.

E.E.A(2015). Air quality in europe – 2015 report. eea report. Technical Report 5/2015, European Environment Agency, 2015.

E. Ekhart. De la structure thermique de l'atmosphere dans la montagne. *La météorologie*, 4: 3–26, 1948.

N. A. Engerer, D. J. Stensrud, and M. C. Coniglio. Surface characteristics of observed cold pools. *Monthly Weather Review*, 136(12):4839–4849, 2008. doi: 10.1175/2008MWR2528.1.

J. F. Evelyn. or, the inconveniencie of the aer and smoak of london dissipated together with some remedies humbly proposed by je esq. to his sacred majestie, and to the parliament now assembled. *Printed by W. Godbid for G. Bedel and T. Collins London*, 1661, 1661.

T. G. Farr, P. A. Rosen, E. Caro, R. Crippen, R. Duren, S. Hensley, M. Kobrick, M. Paller, E. Rodriguez, L. Roth, et al. The shuttle radar topography mission. *Rev. Geophys.*, 45(2), 2007.

R. G. Fleagle. A theory of air drainage. *Journal of Meteorology*, 7(3):227–232, 1950.

J. Garratt et al. *The atmospheric boundary layer. Cambridge atmospheric and space science series*, volume 416. 1992.

A. Gohm, F. Harnisch, J. Vergeiner, F. Obleitner, R. Schnitzhofer, A. Hansel, A. Fix, B. Neininger, S. Emeis, and K. Schäfer. Air pollution transport in an alpine valley: Results from airborne and ground-based observations. *Boundary-layer meteorology*, 131 (3):441–463, 2009.

M. C. Green, J. C. Chow, J. G. Watson, K. Dick, and D. Inouye. Effects of snow cover and atmospheric stability on winter pm2. 5 concentrations in western us valleys. *J. Appl. Meteorol. Climatol.*, 54(6):1191–1201, 2015.

G. A. Grell, S. Emeis, W. R. Stockwell, T. Schoenemeyer, R. Forkel, J. Michalakes, R. Knoche, and W. Seidl. Application of a multiscale, coupled mm5/chemistry model to the complex terrain of the votalp valley campaign. *Atmospheric Environment*, 34(9): 1435–1453, 2000.

D. K. Hall, G. A. Riggs, and V. V. Salomonson. Modis snow and sea ice products. In *Earth science satellite remote sensing*, pages 154–181. Springer, 2006.

G. Heywood. Katabatic winds in a valley. *Quarterly Journal of the Royal Meteorological Society*, 59(248):47–58, 1933.

B. Hicks, D. Baldocchi, T. Meyers, R. Hosker, and D. Matt. A preliminary multiple resistance routine for deriving dry deposition velocities from measured quantities. *Water, Air, and Soil Pollution*, 36(3-4):311–330, 1987.

W. C. Hinds. *Aerosol technology: properties, behavior, and measurement of airborne particles*. John Wiley & Sons, 2012.

S.-Y. Hong. A new stable boundary-layer mixing scheme and its impact on the simulated east asian summer monsoon. *Q. J. R. Meteorol. Soc.*, 136(651):1481–1496, 2010.

M. Z. Jacobson. Control of fossil-fuel particulate black carbon and organic matter, possibly the most effective method of slowing global warming. *Journal of Geophysical Research: Atmospheres*, 107(D19):ACH–16, 2002.

M. Z. Jacobson. *Fundamentals of atmospheric modeling*. Cambridge university press, 2005.

J.-L. Jaffrezo, G. Aymoz, C. Delaval, and J. Cozic. Seasonal variations of the water soluble organic carbon mass fraction of aerosol in two valleys of the french alps. *Atmos. Chem. Phys.*, 5(10):2809–2821, 2005.

M. A. Jiménez and J. Cuxart. A study of the nocturnal flows generated in the north side of the pyrenees. *Atmospheric research*, 145:244–254, 2014.

P. A. Jiménez, J. Dudhia, J. F. González-Rouco, J. Navarro, J. P. Montávez, and E. García-Bustamante. A revised scheme for the wrf surface layer formulation. *Mon. Weather. Rev.*, 140(3):898–918, 2012.

M. Kanakidou, K. Tsigaridis, F. J. Dentener, and P. J. Crutzen. Human-activity-enhanced formation of organic aerosols by biogenic hydrocarbon oxidation. *Journal of Geophysical Research: Atmospheres*, 105(D7):9243–9354, 2000.

P. L. Kinney and H. Özkaynak. Associations of daily mortality and air pollution in los angeles county. *Environmental Research*, 54(2):99–120, 1991.

J. Klemp, J. Dudhia, and A. Hassiotis. An upper gravity-wave absorbing layer for nwp applications. *Mon. Weather. Rev.*, 136(10):3987–4004, 2008.

T. Kuwagata and J. Kondo. Observation and modeling of thermally induced upslope flow. *Boundary-Layer Meteorology*, 49(3):265–293, 1989.

M. Lang, A. Gohm, and J. Wagner. The impact of embedded valleys on daytime pollution transport over a mountain range. *Atmos. Chem. Phys.*, 15(20):11981–11998, 2015.

N. P. Lareau, E. Crosman, C. D. Whiteman, J. D. Horel, S. W. Hoch, W. O. Brown, and T. W. Horst. The persistent cold-air pool study. *Bull. Am. Meteorol. Soc.*, 94(1):51–63, 2013.

Y. Largeron. *Dynamique de la Couche Limite Atmosphérique Stable en relief complexe. Application aux épisodes de pollution particulaire des vallées alpines.* PhD thesis, Université de Grenoble, 2010.

Y. Largeron and C. Staquet. Persistent inversion dynamics and wintertime pm_{10} air pollution in alpine valleys. *Atmos. Environ.*, 135:92–108, 2016.

Y. Largeron, C. Staquet, and C. Chemel. Characterization of oscillatory motions in the stable atmosphere of a deep valley. *Boundary-layer meteorology*, 148(3):439–454, 2013a.

Y. Largeron, C. Staquet, and C. Chemel. Characterization of oscillatory motions in the stable atmosphere of a deep valley. *Boundary-layer meteorology*, 148(3):439–454, 2013b.

M. Lehner and A. Gohm. Idealised simulations of daytime pollution transport in a steep valley and its sensitivity to thermal stratification and surface albedo. *Boundary-layer meteorology*, 134(2):327–351, 2010a.

M. Lehner and A. Gohm. Idealised simulations of daytime pollution transport in a steep valley and its sensitivity to thermal stratification and surface albedo. *Boundary-Layer Meteorol.*, 134(2):327–351, 2010b.

J. Li and B. Atkinson. Transition regimes in valley airflows. *Boundary-Layer Meteorology*, 91(3):385–411, 1999.

L. Łobocki. Surface-layer flux–gradient relationships over inclined terrain derived from a local equilibrium, turbulence closure model. *Boundary-Layer Meteorology*, 150(3): 469–483, Mar 2014.

A. Maurizi, F. Russo, and F. Tampieri. Local vs. external contribution to the budget of pollutants in the po valley (italy) hot spot. *Science of the total environment*, 458:459–465, 2013.

T. B. McKee and R. D. O'Neal. The role of valley geometry and energy budget in the formation of nocturnal valley winds. *Journal of Applied Meteorology*, 28(6):445–456, 1989.

R. T. McNider. A note on velocity fluctuations in drainage flows. *J. Atmos. Sci.*, 39(7): 1658–1660, 1982.

A. G. Megaritis, C. Fountoukis, P. E. Charalampidis, H. A. C. Denier van der Gon, C. Pilinis, and S. N. Pandis. Linking climate and air quality over europe: effects of meteorology on $pm_{2.5}$ concentrations. *Atmospheric Chemistry and Physics*, 14(18):10283–10298, 2014. doi: 10.5194/acp-14-10283-2014. URL https://www.atmos-chem-phys.net/14/10283/2014/.

S. Menon, J. Hansen, L. Nazarenko, and Y. Luo. Climate effects of black carbon aerosols in china and india. *Science*, 297(5590):2250–2253, 2002.

E. J. Mlawer, S. J. Taubman, P. D. Brown, M. J. Iacono, and S. A. Clough. Radiative transfer for inhomogeneous atmospheres: RRTM, a validated correlated-k model for the longwave. *J. Geophys. Res.*, 102:663–682, 1997.

N. E. Monsen, J. E. Cloern, L. V. Lucas, and S. G. Monismith. A comment on the use of flushing time, residence time, and age as transport time scales. *Limnology and oceanography*, 47(5):1545–1553, 2002.

H. Morrison, J. Curry, and V. Khvorostyanov. A new double-moment microphysics parameterization for application in cloud and climate models. part i: Description. *J. Atmos. Sci.*, 62(6):1665–1677, 2005.

E. Neemann, E. Crosman, J. Horel, and L. Avey. Simulations of a cold-air pool associated with elevated wintertime ozone in the uintah basin, utah. *Atmos. Chem. Phys.*, 15(1), 2015.

A. Paci, C. Staquet, J. Allard, H. Barral, G. Canut, J.-M. Cohard, J.-L. Jaffrezo, P. Martinet, T. Sabattier, F. Troude, et al. La campagne passy-2015: dynamique atmosphérique et qualité de l'air dans la vallée de l'arve. *2268-3798*, 2017.

S. E. Peckham, G. A. Grell, S. A. McKeen, M. Barth, G. Pfister, C. Wiedinmyer, J. D. Fast, W. I. Gustafson, S. J. Ghan, R. Zaveri, et al. *WRF/Chem Version 3.3 User's Guide*. US Department of Commerce, National Oceanic and Atmospheric Administration, Oceanic and Atmospheric Research Laboratories, Global Systems Division, 2012.

C. Piot. *Polluants atmosphériques organiques particulaires en Rhône-Alpes: caractérisation chimique et sources d'émissions*. PhD thesis, Université de Grenoble, 2011.

C. A. Pope and D. W. Dockery. Health effects of fine particulate air pollution: lines that connect. *Journal of the air & waste management association*, 56(6):709–742, 2006.

W. M. Porch, W. E. Clements, and R. L. Coulter. Nighttime valley waves. *Journal of Applied Meteorology*, 30(2):145–156, 1991.

U. Pöschl. Atmospheric aerosols: composition, transformation, climate and health effects. *Angewandte Chemie International Edition*, 44(46):7520–7540, 2005.

L. Prandtl. Mountain and valley winds in stratified air. *Hafner Publishing company*, pages 422–425, 1952.

X. Querol, A. Alastuey, J. de la Rosa, A. Sánchez-de-la Campa, F. Plana, and C. R. Ruiz. Source apportionment analysis of atmospheric particulates in an industrialised urban site in southwestern spain. *Atmospheric Environment*, 36(19):3113–3125, 2002.

J. Quimbayo-Duarte, C. Staquet, C. Chemel, and G. Arduini. Dispersion of tracers in the stable atmosphere of a valley opening onto a plain. *Boundary-Layer Meteorology*, -(-):—-, 2019a. ISSN 1573-1472.

J. Quimbayo-Duarte, C. Staquet, C. Chemel, and G. Arduini. Impact of along-valley orographic variations on the dispersion of passive tracers in a stable atmosphere. *Atmosphere*, 10(4), 2019b.

G. Rampanelli, D. Zardi, and R. Rotunno. Mechanisms of up-valley winds. *J. Atmos. Sci.*, 61(24):3097–3111, 2004.

A. Rasheed, D. Robinson, A. Clappier, C. Narayanan, and D. Lakehal. Representing complex urban geometries in mesoscale modeling. *International Journal of Climatology*, 31(2): 289–301, 2011.

R. P. Regmi, T. Kitada, and G. Kurata. Numerical simulation of late wintertime local flows in kathmandu valley, nepal: Implication for air pollution transport. *Journal of Applied Meteorology*, 42(3):389–403, 2003.

A. M. Rendón, J. F. Salazar, C. A. Palacio, V. Wirth, and B. Brötz. Effects of urbanization on the temperature inversion breakup in a mountain valley with implications for air quality. *J. Appl. Meteorol. Climatol.*, 53(4):840–858, 2014.

I. A. Renfrew. The dynamics of idealized katabatic flow over a moderate slope and ice shelf. *Q. J. R. Meteorol. Soc.*, 130:1023–1045, 2004.

M. W. Rotach, G. Wohlfahrt, A. Hansel, M. Reif, J. Wagner, and A. Gohm. The world is not flat: implications for the global carbon balance. *Bulletin of the American Meteorological Society*, 95(7):1021–1028, 2014.

T. Sabatier, A. Paci, G. Canut, Y. Largeron, A. Dabas, J.-M. Donier, and T. Douffet. Wintertime local wind dynamics from scanning doppler lidar and air quality in the arve river valley. *Atmosphere*, 9(4):118, 2018.

J. M. Samet, F. Dominici, F. C. Curriero, I. Coursac, and S. L. Zeger. Fine particulate air pollution and mortality in 20 us cities, 1987–1994. *New England journal of medicine*, 343 (24):1742–1749, 2000.

M. Schaap, M. Roemer, F. Sauter, G. Boersen, R. Timmermans, P. Builtjes, and A. Vermeulen. Lotos-euros: Documentation. *TNO report*, 297, 2005.

J. J. Schauer and G. R. Cass. Source apportionment of wintertime gas-phase and particle-phase air pollutants using organic compounds as tracers. *Environmental science & technology*, 34(9):1821–1832, 2000.

J. J. Schauer, M. J. Kleeman, G. R. Cass, and B. R. Simoneit. Measurement of emissions from air pollution sources. 2. c1 through c30 organic compounds from medium duty diesel trucks. *Environmental Science & Technology*, 33(10):1578–1587, 1999.

J. Schmidli and R. Rotunno. Mechanisms of along-valley winds and heat exchange over mountainous terrain. *Journal of the atmospheric sciences*, 67(9):3033–3047, 2010.

J. Schmidli and R. Rotunno. The quasi-steady state of the valley wind system. *Frontiers in Earth Science*, 3:79, 2015.

U. Schuman. Large-eddy simulation of the up-slope boundary layer. *Quarterly Journal of the Royal Meteorological Society*, 116(493):637–670, 1990.

A. Scotti, C. Meneveau, and D. K. Lilly. Generalized smagorinsky model for anisotropic grids. *Physics of Fluids A: Fluid Dynamics (1989-1993)*, 5(9):2306–2308, 1993.

G. A. Sehmel. Particle and gas dry deposition: a review. *Atmospheric Environment (1967)*, 14(9):983–1011, 1980.

J. H. Seinfeld and S. N. Pandis. *Atmospheric chemistry and physics: from air pollution to climate change*. John Wiley & Sons, 2012.

S. Serafin and D. Zardi. Daytime heat transfer processes related to slope flows and turbulent convection in an idealized mountain valley. *Journal of the Atmospheric Sciences*, 67(11): 3739–3756, 2010.

S. Serafin, B. Adler, J. Cuxart, S. De Wekker, A. Gohm, B. Grisogono, N. Kalthoff, D. Kirshbaum, M. Rotach, J. Schmidli, et al. Exchange processes in the atmospheric boundary layer over mountainous terrain. *Atmosphere*, 9(3):102, 2018.

G. D. Silcox, K. E. Kelly, E. T. Crosman, C. D. Whiteman, and B. L. Allen. Wintertime pm 2.5 concentrations during persistent, multi-day cold-air pools in a mountain valley. *Atmos. Environ.*, 46:17–24, 2012.

W. C. Skamarock, J. B. Klemp, J. Dudhia, D. O. Gill, D. M. Barker, M. G. Duda, X.-Y. Huang, W. Wang, and J. G. Powers. A description of the advanced research wrf version 3. Technical report, National Center For Atmospheric Research Boulder Co Mesoscale and Microscale Meteorology Div, 2005.

S. Smith, F. T. Stribley, P. Milligan, and B. Barratt. Factors influencing measurements of pm10 during 1995–1997 in london. *Atmos. Environ.*, 35(27):4651–4662, 2001.

C. Staquet, A. Paci, and J. Allard. The passy project: objectives, underlying scientific questions and preliminary numerical modeling of the passy alpine valley. *Proc. of the 33rd International on Alpine Meteorology, Innsbruck, Austria*, 2015.

R. Steinacker. Area-height distribution of a valley and its relation to the valley wind. *Contrib. Atmos. Phys.*, 57:64–71, 1984.

R. B. Stull. *An introduction to boundary layer meteorology*, volume 13. Springer Science & Business Media, 2012.

S. Szidat, A. S. Prévôt, J. Sandradewi, M. R. Alfarra, H.-A. Synal, L. Wacker, and U. Baltensperger. Dominant impact of residential wood burning on particulate matter in alpine valleys during winter. *Geophysical Research Letters*, 34(5), 2007.

E. Tomasi, L. Giovannini, D. Zardi, and M. de Franceschi. High-resolution numerical simulations of wintertime atmospheric boundary layer processes in the adige valley during an alpnap project field campaign. In *EGU General Assembly Conference Abstracts*, volume 16, 2014.

S. Vardoulakis and P. Kassomenos. Sources and factors affecting pm10 levels in two european cities: Implications for local air quality management. *Atmos. Environ.*, 42(17):3949–3963, 2008.

I. Vergeiner and E. Dreiseitl. Valley winds and slope winds—observations and elementary thoughtsberg-und tal-bzw. hangwinde—beobachtungen und grundsätzliche überlegungen. *Meteorology and Atmospheric Physics*, 36(1-4):264–286, 1987.

A. Wagner. Theorie und beobachtung der periodischen gebirgswinde (Theory and Observation of Periodic Mountain Winds). *Akademische Verlagsgesellschaft Geest und Portig K.-G., Leipzig, East Germany.*, 1938.

J. Wagner, A. Gohm, and M. Rotach. The impact of valley geometry on daytime thermally driven flows and vertical transport processes. *Q. J. R. Meteorol. Soc.*, 141(690):1780–1794, 2014.

J. Wagner, A. Gohm, and M. Rotach. The impact of valley geometry on daytime thermally driven flows and vertical transport processes. *Quarterly Journal of the Royal Meteorological Society*, 141(690):1780–1794, 2015.

C. D. Whiteman. Breakup of temperature inversions in deep mountain valleys: Part i. observations. *Journal of Applied Meteorology*, 21(3):270–289, 1982.

C. D. Whiteman. Observations of thermally developed wind systems in mountainous terrain. In *Atmospheric processes over complex terrain*, pages 5–42. Springer, 1990.

C. D. Whiteman. *Mountain meteorology: fundamentals and applications*. Oxford University Press, 2000.

C. D. Whiteman, T. B. McKee, and J. Doran. Boundary layer evolution within a canyonland basin. part i: Mass, heat, and moisture budgets from observations. *Journal of Applied Meteorology*, 35(12):2145–2161, 1996.

C. D. Whiteman, B. Pospichal, S. Eisenbach, P. Weihs, C. B. Clements, R. Steinacker, E. Mursch-Radlgruber, and M. Dorninger. Inversion breakup in small rocky mountain and alpine basins. *J. Appl. Meteorol.*, 43(8):1069–1082, 2004.

C. D. Whiteman, A. Muschinski, S. Zhong, D. Fritts, S. W. Hoch, M. Hahnenberger, W. Yao, V. Hohreiter, M. Behn, Y. Cheon, et al. Metcrax 2006: Meteorological experiments in arizona's meteor crater. *Bulletin of the American Meteorological Society*, 89(11): 1665–1680, 2008.

C. D. Whiteman, S. W. Hoch, J. D. Horel, and A. Charland. Relationship between particulate air pollution and meteorological variables in utah's salt lake valley. *Atmos. Environ.*, 94: 742–753, 2014.

D. Zardi and C. D. Whiteman. Diurnal mountain wind systems. In *Mountain Weather Research and Forecasting*, pages 35–119. Springer, 2013.

S. Zoras, A. Triantafyllou, and D. Deligiorgi. Atmospheric stability and pm10 concentrations at far distance from elevated point sources in complex terrain: Worst-case episode study. *Journal of environmental management*, 80(4):295–302, 2006.